EFFECTS OF ROCK TEXTURE ON SURFACTANT-ASSISTED SPONTANEOUS IMBIBITION: AN EXPERIMENTAL AND STOCHASTIC STUDY IN TIGHT LIQUID-RICH RESERVOIRS

A Thesis

by

HASSAN WASEL A. AL HASHIM

Submitted to the Office of Graduate and Professional Studies of
Texas A&M University
in partial fulfillment of the requirements for the degree of

MASTER OF SCIENCE

Chair of Committee, David S. Schechter
Committee Members, Maria A. Barrufet
Ibrahim Y. Akkutlu
Head of Department, Jeff B. Spath

August 2019

Major Subject: Petroleum Engineering

ABSTRACT

The addition of surfactants to completion fluids in ULRs is widely believed to boost productivity and prolong well life. Previous laboratory studies have revealed that this approach is capillary-driven via spontaneous imbibition. This is a result of the interaction of surfactant solutions with the oil/water/rock interface. Nevertheless, published works regarding the effect of pore-size distribution (PSD) and the textural characteristics of the rock on the mechanism of surfactant-assisted spontaneous imbibition (SASI) are scarce at most.

The purpose of this research is to provide a complete workflow for assessing the effectiveness of SASI and unveil a target pore size range for SASI EOR through a combination of experimental results, computed tomography (CT), scanning electron microscope (SEM), and nuclear magnetic resonance (NMR). In addition, interfacial tension (IFT), contact angle (CA), zeta potential, surfactant adsorption isotherm, and spontaneous imbibition experiments were all performed as part of the initial data gathering process. Ten SASI experiments were conducted at reservoir temperature using different surfactants on quartz- and carbonate-rich side-wall core samples obtained from the Wolfcamp formation in the Midland Basin. CT-scan technology was used to visualize the process of oil expulsion from the core plugs and assess fluid movement throughout the imbibition process. SEM was used to match the NMR PSD and obtain the surface relaxivity conversion factor for each core sample. This conversion factor was used to find the equivalent spherical radius (ESR) at each relaxation time. The target pore size range

and fluid distribution for SASI EOR in the Wolfcamp formation was determined from the NMR results.

The primary SASI EOR production mechanism is highly influenced by wettability alteration and IFT reduction. The SASI experiments showed optimistic oil recovery results in both quartz- and carbonate-rich core samples, with up to 36% and 40% of the original oil in place (OOIP), respectively. Measurements of the adsorption isotherm showed a positive correlation between the wettability alteration performance and amount of surfactant adsorbed onto the rock surface. The NMR results revealed that PSD plays a significant role in SASI EOR; the majority of the imbibed fluid was observed in smaller pores larger than those of clay-bound water (CBW) but smaller than those of high permeability streaks or bedding planes. Consideration of PSD has a significant impact on successful surfactant selection and proper EOR process design. CT scanning was also used to validate the NMR results, which revealed a direct relationship between CT imaging and NMR outcomes.

The novelty of this research comes from the insight it offers into the essential role of PSD in SASI EOR through the use of CT, SEM, and NMR technologies. In addition, a new workflow for surfactant selection is proposed that unveils the real potential of SASI in low and ultra-low permeability clastic and carbonate reservoirs.

ACKNOWLEDGEMENTS

I would like to thank my committee chair, Dr. Schechter, and my committee members, Dr. Akkutlu and Dr. Barrufet for their guidance, support, and patience in answering all of my questions throughout this research.

I'm very grateful to my colleague Fan Zhang, perhaps Dr. Zhang by the time of the publication of this work, for his help and advice with the numerical portion of this research. I would not have managed to complete it without his assistance.

Special gratitude goes out to Dr. Jinhong Chen and Dr. Stacey Althaus at Aramco Services Houston Research Center for their valuable input and technical support on the petrophysics and physics of the fluid transport in tight pore spaces. Without their help, a huge percentage of this work would not have been possible.

A special mention to Dr. Ashraf Tahini for his blessing to use the nuclear magnetic resonance instrument available at Aramco Services Houston Research Center. It was a pleasure to work at your facility with your competent staff. What an astonishing and highly sophisticated place to work at!

I would also like to express my sincere gratitude to Saudi Aramco Southern Area Reservoir Management Department for giving me this opportunity to pursue an advanced degree in petroleum engineering at a highly reputable university such as Texas A&M.

Thanks also go to my colleagues Imad Adel and Wayan Rakananda Saputra for their guidance throughout the experimental part of this research.

Last but not least and by no means least, in this case, thanks to my father, Wasel and brother, Ahmed for their encouragement and inspiration and to my mother for her continuous moral support and endless love.

CONTRIBUTORS AND FUNDING SOURCES

Contributors

This work was supervised by a thesis committee consisting of professor David S. Schechter and professor Ibrahim Y. Akkutlu of the Department of Petroleum Engineering and professor Maria A. Barrufet of the Department of Chemical Engineering.

All other work conducted for the thesis was completed independently by the student.

Funding Sources

This research was funded by the Southern Area Reservior Management Department at Saudi Aramco. The work contents are solely the responsibility of the author and do not necessarily represent the official views of Saudi Aramco

TABLE OF CONTENTS

Page

LIST OF FIGURES

LIST OF TABLES

CHAPTER 1

INTRODUCTION

Oil production from tight reservoirs has seen a steady increase since the early 2000s, as the majority of the remaining oil in the world is contained in low or moderate rock quality reservoirs. This process forms the bulk of American crude oil production, accounting for 65% of the total onshore oil production in the US. Producing an enormous volume from such reservoirs has placed many countries, especially the United States, at a point of advantage, enabling them to export large volumes of oil to the global market to offset the demands of non-producing countries. This venture has also added to the supply of gas, which further offsets the domestic demand of this commodity. The result has occasionally been a decrease in oil prices, as was the case in 2015. This global oil price decline was mainly elicited by OPEC countries as a means of maintaining their market share. Nonetheless, booming oil production from tight rocks was the genesis of the oversupply in the global oil market.

Recognition of source rocks dates back to the initial conventional reservoir petroleum industry. Source rocks are the source of hydrocarbon in conventional reservoirs. Production from such tight rocks is often deemed unreasonable because the rock is of a unique ultra-tight nature. Higher cost frequently accompanies tighter target zones of low-quality rock. The mean pore size for a low-quality rock matrix, be it clastic or carbonate, ranges from 10 to 100 nm (Nelson 2009). A nanoscale pore size directly affects the porosity and permeability of rocks, resulting in a different production mechanism than might be used in rocks with larger pores. Ordinarily, porosity drops to approximately 12%,

while permeability is in the hundreds in terms of nano-darcy, or in the lower end of milli-darcy, at best. However, hydrocarbon production from low permeability reservoirs became economically appealing following the work of George P. Mitchell, who began implementing a combination of massive multi-stage hydraulic fracturing and horizontal wells to enhance production, thereby making productivity satisfactory (Steward 2013).

Well productivity can ultimately be enhanced by drilling horizontally with multi-stage hydraulic fractures across the lateral, since this offers more contact area between the wellbore and reservoir matrix. This makes economic sense when it comes to producing from low porosity and permeability reservoirs. Horizontal wells improve production by increasing the contact area between the reservoir and wellbore as more matrix area becomes accessible; this occurs when the reservoir is penetrated horizontally, as opposed to vertically. Thus, the productivity of a well is often associated with the term "kh," where k is the permeability and h is the length of the lateral or thickness, depending on the model used. Normally, the higher the kh, the more productive the well. Hydraulic fracturing also enhances productivity by improving the contact area, as well as providing a better flow path from the matrix to the wellbore. An artificial fracture network is usually created around the wellbore when a large volume of fluid is pumped under high pressure. These fractures yield more access to the matrix, along with the increase induced by drilling the well horizontally. The flow geometry is significantly improved around the wellbore because the resulting fractures possess a permeability that is three orders of magnitude higher than that of the matrix (Advani, Khattab and Lee 1985).

Both horizontal drilling and multi-stage hydraulic fracture have been shown to minimize cost while maximizing productivity. The recovery factor, however, is still relatively low, despite efforts to improve it by employing horizontal drilling and hydraulic fracturing technologies. Many proposals have been made regarding recovering more of the oil that remains in a porous medium. Longer lateral and larger hydraulic fracture operations have been proposed to enhance production and increase recovery. Infill drilling is another option that allows access to more reservoir area. However, Lindsay et al. (2018) conducted a study of ten different unconventional basins and concluded that the productivity of the infill wells was substantially lower than that of the parent wells. Infill drilling may lead to increased production, but may not be economically feasible in tight reservoirs.

Adding a surfactant to hydraulic fracturing completion fluids has gained in popularity, with the belief that it improves on both initial production and ultimate oil recovery (EUR). The addition of a surfactant to completion fluids is not a novel technique in itself. It has been applied as a step in hydraulic fracturing jobs to minimize the effect of water block that may arise from water moving into the matrix during the high-pressure injection of fracturing fluid (Liang et al. 2017). However, it has recently been discovered that surfactant molecules are capable of more than just minimizing the effect of water block. They are soluble in water and oil, and possess both hydrophobic and hydrophilic groups. The two groups grant the surfactant molecules the ability to change the way water and oil interact, as these molecules are able to bridge between the two immiscible fluids. The most notable change that occurs when surfactants are added to a system of water, oil,

and rock is a decrease in the interfacial tension that exists between water and oil, as well as a clear shift in wettability (J. O. Alvarez and Schechter 2016). When it comes to oil reservoirs, these two effects translate into higher productivity via a mechanism known as surfactant-assisted spontaneous imbibition (SASI).

Imbibition takes place when oil moves out of the pores as water moves in to replace produced oil. In this regard, fluid movement takes place in the absence of any pressure deferential effect in the system. This means that the process of fluid exchange is not instigated by viscous force, but rather by the capillary forces responsible for driving the oil out from the pores. Surfactants act as catalysts in this process because they reduce the IFT and alter wettability. Young and Laplace described capillary pressure as a function of wettability, IFT, and pore radius. By shifting the wettability towards the more water-wet region ($\theta < 90$), surfactants cause the capillary force direction to shift in response, making SASI more favorable. This increases the volume of oil expelled, as well as the rate of oil withdrawal. The surfactants, however, decrease IFT, leading to a lower capillary force; this is because the power behind this force is controlled by the IFT of the oil and aqueous solution. IFT is also undesirable when it is unaltered, as this may lead to reduced dispersion of the surfactant solutions into the matrix, thereby reducing the performance of the surfactant's effectiveness during SASI.

Over the course of the last five years, surfactants and their role in imbibition have continued to be studied in labs. Tests have been carried out on the three most prolific oil-bearing tight reservoirs: Eagle Ford, Wolfcamp, and Bakken. These studies found that the addition of surfactants yielded more oil production from spontaneous imbibition, as

compared to a basic case of water without any additives (Johannes O Alvarez, Saputra, and Schechter 2017; J. O. Alvarez and Schechter 2016). The majority of the experimental studies employed IFT, contact angle, and zeta potential measurements to investigate the effects of adding different surfactants to a variety of rock-oil combinations. Spontaneous imbibition experiments were carried out by submerging core plugs into different surfactant solutions in modified Amott cells in order to measure how the performance of a surfactant might influence oil production. The findings of these experiments showed that surfactants have the ability to reduce IFT, which is mainly influenced by the interaction of the oil and surfactant. Wettability alteration was also observed, where increasing water-wetness was achieved by the addition of surfactants to water. Imbibition also displayed different ranges of production improvement at a variety of degrees and in various oil compositions, rock types, and surfactant combinations. All studies found that surfactant-assisted imbibition led to improved oil recovery, at least at the lab level.

Application of surfactant-assisted spontaneous imbibition in the field involves adding the ideal surfactant solution to the frac fluid during the course of the frac job. The rationale behind doing so is to allow for more reservoir contact with the surfactant solution. Most studies regarding SASI, however, are limited to laboratory-scale observations. Field-scale performance studies, on the other hand, are of great importance, as they offer another point of view with regards to the relevance of this concept in field applications. Most lab studies are carried out with imbibition being observed in the absence of the application of a pressure difference, which is not the case in the field where pressure drawdown exists. (Saputra and Schechter 2018) conducted a numerical study in

an attempt to understand the benefits of adding surfactants to completion fluids in the presence of pressure differences in field applications. They found that SASI did indeed improve the initial oil production rate by 22%, and the three-year cumulative oil recovery by 18.4% (as compared to the base case). However, the benefit of SASI on a field scale differs strongly based on the reservoir's petrophysical properties. Thus, the present study bridges a gap regarding the effects of a reservoir's petrophysical properties such as pore size distribution and heterogeneity on the performance of SASI.

The main objective of this research is to provide a complete workflow for evaluating the performance of surfactants in improving well productivity. This entails analyzing the effects of a reservoir's petrophysical properties and imbibition mechanism, thereby bridging the gap in the current widely-used workflow. This study is divided into three main sections: experimental and fundamental, SASI and oil displacement, and textural characterization and pore size distribution. In the experimental and fundamental analysis section, all necessary data with regards to how oil, water, surfactants, and rock interact together is gathered and investigated. These data also include rock and fluid characterizations, interfacial tension, contact angle, zeta potential, and adsorption isotherm. The SASI and oil displacement analysis section includes CT-scan images and, ultimately, a spontaneous imbibition experiment. Lastly, the textural characterization and pore size distribution analysis section includes the effects of a reservoir's petrophysical properties such as pore size distribution and heterogeneity on the performance of SASI, along with the mechanism of oil production employed during the SASI experiments.

1.1 Pore Size

Porosity is one of many different attributes used for pore quantification. However, porosity is a single averaged value that does not reflect the heterogeneity of the pores in a porous medium. Another attribute that is often used for a more precise structure and pore quantification is pore–size distribution (PSD). PSD enumerates the frequency of occurrence associated with different pore sizes. The term "pore size" does not have a precise definition because pores do not exist uniformly in a matrix. There are many irregular and interconnected networks of pores localized in different locations within a matrix. Therefore, there is no unique definition of "pore size," which has resulted in multiple proposed techniques for measuring PSD.

Every PSD measurement technique defines pore size qualitatively. Then, the qualitative results are converted into quantitative outcomes based on a fit-for-purpose pore model, stochastic analysis, or both. Multiple models have been used to convert qualitative data into quantitative results, such as open-ended cylinders or spheres. In this work, the assumption of a spherical model for PSD determination is used, and the obtained diameters termed "equivalent spherical diameters." This approximation is treated as a one-dimensional representation of the irregular and interconnected complex three-dimensional pore structure of a matrix. Also, neither mercury injection capillary pressure (MICP) nor gas adsorption is used in this work because they represent pore throat distribution (PTD) and often tend to underestimate pore diameters, due to the high pressure that needs to be applied for an intrusion to occur.

In the literature, pore-size terminology varies; however, in this work, the International Union of Pure and Applied Chemistry (IUPAC) Sing (1982) classification system is used. This method divides pores into three main categories, based on their size. Pores that are > 50 nm are classified as macropores, pores between 2 and 50 nm are designated as mesopores, and pores < 2 nm are identified as micropores.

1.2 Research Objectives

The significance of surfactant-assisted spontaneous imbibition oil production in tight reservoirs and the lack of understanding of the mechanism behind it are the two main factors motivating this research. The research objectives addressed in this study are as follows:

1. Investigate the feasibility of the addition of surfactants to hydraulic fracturing or completion fluids to enhance oil recovery.
2. Evaluate the dominant aspect affecting the mechanism of the surfactant-assisted spontaneous imbibition process.
3. Understand the various pore-structure characteristics and their relationship to the oil produced from the surfactant-assisted spontaneous imbibition process.
4. Develop a workflow for estimating grain size, along with the distribution of pores within a matrix.
5. Provide a comprehensive workflow for evaluating the effects of surfactant addition to completion fluid through laboratory experiments and special core analysis.

1.3 Scientific Approach

The scientific approach includes the application of a scientific method or methods to demonstrate adequacy. According to Wolfs (1996), the scientific method is "the process by which scientists collectively endeavor to construct an accurate representation of the world. Schafersman (1997) defined the term as "reliable knowledge that has a high probability of being true because its veracity has been justified by a reliable method." Although the steps of the scientific methods vary greatly, they follow the same approach. Sidle and Lee (2010) proposed five steps for verifying and implementing the scientific method. These can be summarized as follows:

1. Define the question.
2. Research the question and formulate a hypothesis.
3. Perform experiments, and collect and analyze the data.
4. Interpret the data and draw conclusions.
5. Revise the hypothesis if necessary, and repeat Steps 3 and 4.

These steps require researchers to clearly define the question to guide the user to formulate a proper hypothesis. To demonstrate and validate the significance of rock properties and petrophysical data in the imbibition process, the adopted scientific approach is as follows.

- **Define the proposed reliable technology that will contribute to unveiling the significance of the rock's textural characteristics to the imbibition process.**

  In this case, NMR and FE-SEM, coupled with CT imaging, a pore quantification approach, and deconvolution technologies, were all used to acquire information sufficient to reach conclusive results.

- **Research the question and determine how well the science behind the proposed technology works in theoretical (i.e., perfect) situations, and identify the effect of non-ideal situations on the applied success of the proposed technologies.**

  All technologies used in this research have been proven reliable by many qualified petroleum engineering critics and researchers. For example, NMR has been used in open hole logging for the past 40 years, with the primary use being the determination of moveable and bound fluids contained in a porous medium. The main limitation of this approach is related to the "tightness" of the subject formation. This issue was mitigated through the use of a higher radio frequency source to detect fluids contained in smaller pores. FE-SEM is an imaging technique that has long been in use. The limitation of this method stems from the frequently bad image resolution, questionable adequacy of the rock surface used, and the fact that the images represent a very small portion of the core sample. Each limitation can be mitigated separately. The resolution issue was solved by equipping a high brightness conical field emission gun, resulting in significant improvement. The questionable adequacy of the sample surface was eliminated by embedding the samples in epoxy, polishing the epoxy to expose the surface of the rock chips, and smoothing the chips using multiple geologic smoothing grits. The last issue, in which the images taken represent a very small portion of the core sample, was solved by taking as many images as possible and projecting them onto the NMR distributions obtained by scanning the entire set of core samples. Pore quantification and deconvolution techniques are no different from any other mathematical approach, in that certain limitations are often encountered due to

improper boundary limits and inconsistencies when analyzing the data. These limitations were mitigated through the introduction of the term “equivalent spherical radius” to preserve consistency in the data analysis and boundary limits.

- **Test the technology to validate or invalidate the hypothesis.**

  All technologies used in this research were applied conjointly and systematically to prove the hypothesis that “*the dominant aspect affecting the mechanism of the surfactant-assisted spontaneous imbibition process is indeed capillary influenced, resulting in the majority of the imbibed fluid ending up in either smaller or larger pores, depending on the wettability of the rock/water/oil interface*.” The experimental approach taken to validate the hypothesis involved testing multiple surfactant solutions with different wettability alteration capabilities on a variety of rock samples of various compositions. PSD was then evaluated for each core sample and the imbibition contribution estimated with regards to different relaxation times. The relaxation times were then converted into the equivalent spherical radius through the use of FE-SEM and quantitative pore body distribution data acquisition techniques. 2-D images were also used to analyze the composition of the produced fluid and residual oil, subsequent to the imbibition experiments. It is worth noting that multiple trials were performed for each test to ensure the number of tests performed was adequate to support the statistical significance of the conclusion. Also, all test data and results were included in evaluating the hypothesis, in order to eliminate any statistical selection and survivor bias that might transpire from discarding undesirable results.

- **Provide documentation, including a description of the conditions needed to achieve reliability, and explain the input data and how to identify misapplications of the technology.**

  All necessary documents defining the conditions, assumptions, boundary limits, and input data can be found in their designated chapters. The References section includes previous work performed by other researchers, scientists, and engineers regarding the research topic.

1.4 Thesis Organization

This thesis is organized into three broad categories and divided into five chapters. The first chapter, **Chapter 1**, introduces the main research problem and the samples used for this research. The next chapter, **Chapter 2**, is a literature review providing a brief summary of the previous studies conducted on the subject, along with some information about surfactant-assisted spontaneous imbibition methods commonly used to measure different surfactant-related properties. **Chapter 3** is centered on the methodologies used to measure all of the fundamental parameters and results pertaining to surfactant-related properties such as interfacial tension, contact angle, zeta potential, and adsorption isotherm. **Chapter 4** analyzes recoveries from surfactant-assisted spontaneous imbibition and oil displacement monitoring using CT-scan imaging. **Chapter 5** presents a detailed pore structure and textural analysis using nuclear magnetic resonance (NMR), along with scanning electron microscopy (SEM). This chapter also includes a detailed discussion of the effects of rock texture characterization on oil recovery from the imbibition process.

Chapter 6 offers an interpretation of the results and recommendations developed from this study, and summarizes the observations found during the course of this work.

1.5 List of Publications

- **Submitted Conference papers:**

  Alhashim, H.W., Zhang, F., Schechter, D.S., and Jinhong Chen. 2019. Investigation of the Effect of Pore Size Distribution on the Produced Oil from Surfactant-Assisted Spontaneous Imbibition in ULR Using NMR. Presented at the SPE Annual Technical Conference and Exhibition, Calgary, Albert, Canada.

- **Submitted in peer reviewed journals:**

  Alhashim, H.W., Zhang, F., Schechter, D.S., and Jinhong Chen. 2019. Investigation of the Effect of Pore Size Distribution on the Produced Oil from Surfactant-Assisted Spontaneous Imbibition. Submitted to SPE Journal.

- **In preparation proceedings and abstracts:**

  Alhashim, H.W., Zhang, F., Schechter, D.S., and Jinhong Chen. 2019. Produced Oil Composition Change during Surfactant-Assisted Spontaneous Imbibition.

CHAPTER 2

LITERATURE REVIEW

This literature review covers the major studies previously conducted on spontaneous imbibition and the role that surfactants play in that process. This chapter also covers concepts related to different experimental procedures for spontaneous imbibition, as well as how surfactants interact with oil-water-rock combinations.

2.1 Contact Angle

A drop of liquid on a solid surface can rest as a drop with a finite area, or it can spread infinitely on the surface plane. This phenomenon is mainly governed by the amount of interfacial energy gained to form the liquid-solid interface. In a pure liquid, the molecules are pulled equally in all directions by neighboring molecules, resulting in a net force equal to zero. However, molecules exposed at the surface do not have neighboring molecules to pull, and thus balance the forces. Those molecules are pulled inward by their counterparts, causing internal pressure that forces the liquid to contract on the surface, in order to achieve the lowest surface-free energy. In other words, the intermolecular force needed to make the surface contract (i.e., surface tension) is responsible for the liquid droplet's profile**.** Hence, the condition needed for spreading is satisfied when the interfacial tension gained to form the unit area for the liquid-solid interface exceeds that which is gained to form the unit area for the liquid-vapor interface, as follows:

$$\gamma_{SV} - \gamma_{SL} > \gamma_{LV} \tag{2-1}$$

where γ_{SV} , γ_{SL}, and γ_{LV} represent solid-vapor, solid-liquid, and liquid-vapor interfacial tensions, respectively. When this inequality is not satisfied, the liquid drop remains finite in size, forming an equilibrium contact angle.

2.1.1 Contact Angle and Surface Structure —Young's Equation

The contact angle ($\boldsymbol{\theta}$) is defined as an angle that is formed as a result of the intersection between the liquid-solid and liquid-vapor interfaces when a drop of liquid rests on a flat and horizontal solid surface. The concept of contact angle was first introduced by Thomas Young in 1805. Young, in his research, reasoned that the contact angle depends on the material and not on gravity's force. Therefore, in the absence of gravity, mechanical equilibrium requires that the contact angle of the liquid drop be under the action of three interfacial tensions. These are given by **Eq. (2-2)**:

$$cos\ \theta_Y = \frac{\gamma_{SV} - \gamma_{SL}}{\gamma_{LV}} \tag{2-2}$$

where θ_Y is the Young's contact angle, or a contact angle that can be inputted into Young's equation.

This relationship, however, illustrates that the ratio of energy attained to form the unit area of the liquid-solid interface to that which is required to form the unit area of the liquid-vapor interface is equal to the cosine of the contact angle. Still, the contact angle can be geometrically obtained via the sessile drop method, which involves applying a tangent line in the droplet profile that extends from the liquid-solid contact point along the liquid-vapor interface. The attractiveness of the contact angle measurement stems from its direct relation to wettability. The concept of wettability has recently attracted tremendous interest due to its vast applicability, especially in the oil industry (Yuan and Lee 2013).

As mentioned above, when a liquid drop contacts a solid surface, it can either spread on the surface and form a small contact angle, or it can bead on the surface to form a large angle. More specifically, the wettability of a surface can be classified into three different classes (illustrated in **Figure 2-1**) in terms of the contact angle between an oil drop and rock surface, as follows:

$class\ I\ =\ complete\ wetting\ (\theta\ =\ 0°)$: In this case, a complete wetting occurs as the liquid droplet turns into a flat bubble.

$class\ II\ =\ favorable\ wetting\ (\theta\ <\ 90°)$: This case indicates that the liquid will spread, covering a wide area on the surface (i.e., water-wet).

$class\ III\ =\ unfavorable\ wetting\ (\theta\ >\ 90°)$: This case represents a compact liquid drop, in which the fluid forms a minimum contact angle with the surface to sustain the droplet (i.e., oil-wet).

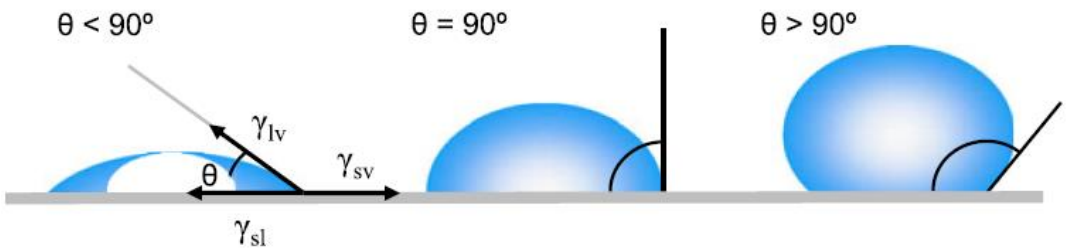

Figure 2-1 Schematic of a sessile liquid drop contact angle profile reprinted from Yuan and Lee (2013).

Note that a "lotus effect" can be observed with water contact angles greater than 150°. Typically, such angles are associated with superhydrophobic surfaces, where non-polarity on the surface repels the water molecules and prevents them from fully spreading over the surface. Instead, the water rolls off the surface in a spherical shape. It is worth noting that the contact angle obtained experimentally using Dataphysics OCA 15 Pro

corresponds to the angle between an oil droplet and rock surface, which does not equal Young's contact angle. Young's contact angle is illustrated in **Figure 2-2**. By convention, it is where a contact angle > 90^{o} is considered oil-wet and a contact angle < 90^{o} is water-wet.

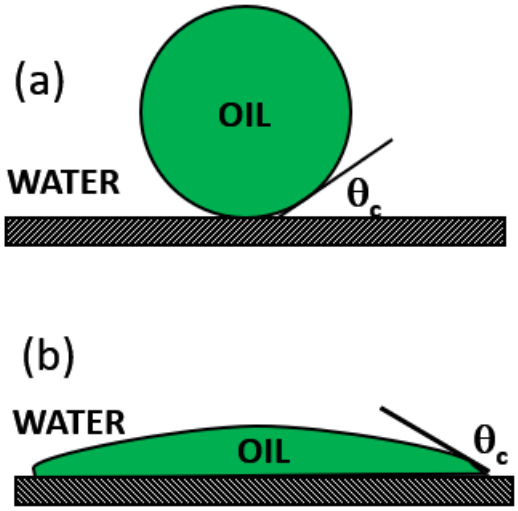

Figure 2-2 Schematic of a sessile liquid drop contact angle by convention, which is what is used in this work. Figure (a) is a more spherical oil bubble, indicating an extreme water-wet case, where (b) is a flat oil droplet indicating an oil-wet case.

2.1.2 Contact Angle Hysteresis

The physical concept of Young's theory has been questioned due to several ambiguities that occur in experiments measuring the contact angle. Although the physical validity of the contact angle holds when experimental procedures that practically yield repeatable measurements described as "equilibrium angles" are carried out, it becomes rather inadequate when fluid is in dynamic motion. In practice, fluid is in a constantly moving state, wetting a solid surface in one turn and exposing it in another. Therefore, a more sophisticated means of measuring the contact angle emerges from a three-phase contact angle line being in physical motion; such an angle is called a "dynamic" contact

angle. The phenomenon can be delineated by analyzing a liquid droplet on a horizontal surface. When the plane is slightly tilted, gravity pulls the droplet downward; another opposite force, "hysteresis," keeps the droplet in place. A lag-to-motion effect will take place in which the liquid-solid contact line does not immediately move, resulting in an asymmetrical droplet. Consequently, an increase in the contact angle can be noticed in the direction of the driving force. The maximum possible angle formed by expanding the liquid before actual motion occurs is called an "advancing angle, θ_a." Likewise, the smallest possible such angle formed by contacting the liquid before reverse motion sets in is called a "receding angle, θ_r." The difference between the advancing and receding angles is called "hysteresis, H," as shown in **Eq. (2-3)**:

$$H = \theta_a - \theta_r \tag{2-3}$$

A hysteresis range apparently occurs as a result of the liquid's resistance to motion at the interface, due to friction.

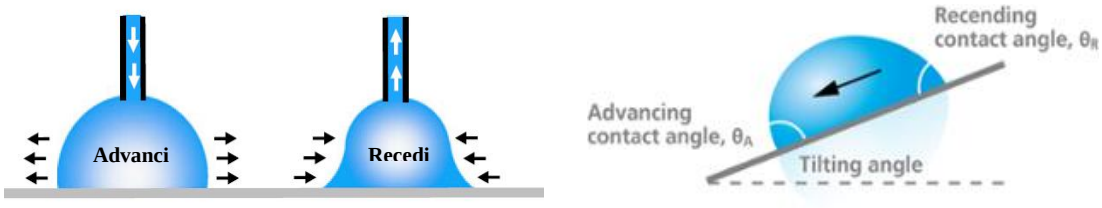

Figure 2-3 Schematic showing the advancing and receding contact angles reprinted from Yuan and Lee (2013).

Theoretically, there are multiple factors that can affect contact angle measurements, such as liquid adsorption and retention, surface deformation, and interdiffusion. However, two major factors can immensely impact contact angle measurements, and hence lead to contact angle hysteresis. The first is surface roughness, and the second is the heterogeneity of the solid surface. If hysteresis is predominantly

caused by roughness, then it is invalid to measure the contact angle by utilizing Young's equation, and doing so will potentially yield erroneous results. The generated contact angle, either from roughness or the heterogeneity of the solid surface, is called the "apparent" contact angle, which may or may not equal to the Young's contact angle. The following shows actual cases depicting how contact angle identification is affected by surface topography:

Case I: On smooth and chemically homogeneous solid surfaces, the experimentally obtained contact angle is Young's contact angle, θ_Y, an "equilibrium angle." In this case, there is no hysteresis taking place.

Case II: On smooth yet chemically heterogenous solid surfaces, θ may not be equal to the thermodynamic Young's contact angle, θ_Y. Nonetheless, the experimentally observed advancing angle, θ_a, is found to be close to that of Young's angle. Although the receding angle, θ_r, can also be implemented in this case to measure the contact angle, it is usually found to be non-reproducible, often because of sorption of the liquid into the solid and swelling of the solid by the liquid (Kwok et al. 1996).

Case III: On rough and chemically heterogeneous solid surfaces, neither the advancing nor receding angles can be utilized in Young's contact angle; thus, measuring the contact angle using Young's equation will yield meaningless results. Experimental studies have also shown that contact angles calculated on smooth surfaces appeared to be smaller than those obtained from rough yet chemically identified surfaces.

Wenzel (1936) and Baxter and Cassie (1945) extensively studied thermodynamic equilibrium angles on rough and heterogeneous surfaces. Wenzel reasoned that roughness

increased the wettability caused by roughening the surface. In other words, contact angles greater than 90° increased due to roughness. Correspondingly, those less than 90° decreased in response to roughened surfaces. This means that hydrophobic surfaces become even more hydrophobic, due to roughening of the surface. If a solid surface is roughened, then the geometric area of the actual surface becomes the projected area times the roughness factor. Hence, the energy gained to form the liquid-solid interface becomes$r(\gamma_{SV} - \gamma_{SL})$, and the contact angle (in terms of roughness), the Wenzel equation, is given by **Eq. (2-4)**:

$$cos\theta_W = \frac{r(\gamma_{SV} - \gamma_{SL})}{\gamma_{LV}} \tag{2-4}$$

where θ' is the apparent angle and r is the roughness factor, which is defined as the ratio of the actual surface to the flat projected area. Note that an r value greater than 1 indicates a rough surface, otherwise $r = 1$ and the apparent contact angle becomes the equilibrium angle, θ_Y. The Wenzel equation, however, fails when the liquid does not fully penetrate into the grooves.

Conversely, Cassie developed an equation that considers heterogenous surfaces such that if the unit of geometrical area of a surface has a fractional area f_1 of contact angle θ_1 and a fractional area f_2 of contact angle θ_2 (so that $f_1 + f_2 = 1$), then the energy E gained by spreading is given by **Eq. (2-5)**:

$$E = f_1(\gamma_{S_1V} - \gamma_{S_1L}) + f_2(\gamma_{S_2V} - \gamma_{S_2L}) \tag{2-5}$$

where γ_{S_1V} and γ_{S_1L} are the interfacial tensions for solid-vapor and solid-liquid, respectively, for fractional area f_1. Likewise, γ_{S_2V} and γ_{S_2L} are the interfacial tensions for fractional area f_2. The contact angle θ'' for the composite surface becomes **Eq. (2-6)**:

$$cos\theta_C = \frac{E}{\gamma_{LV}} = f_1 \cos\theta_1 + f_2 \cos\theta_2 \quad (2\text{-}6)$$

Cassie and Baxter assumed that in practice, porous surfaces are the most significantly heterogenous. Based on this assumption, there is no penetration of the liquid into the grooves, and the composite interface consists of vapor pockets that may be trapped underneath the liquid. In this case, the solid surface fractional area is f_1, whereas f_2 represents the fractional area of air spaces. Accordingly, γ_{S_2V} is zero, and γ_{S_2L} becomes γ_{S_2V}. Rearranging the Cassie equation, the apparent contact angle described by the Cassie-Baxter model is given by **Eqs. (2-7)** and **(2-8)**:

$$cos\theta_{CB} = f_1 \cos\theta_1 - f_2, \quad (2\text{-}7)$$

Since $f_2 = f_{LV}$ *and* $f_1 = 1 - f_2$, then:

$$cos\theta_{CB} = (1 - f_{VL}) \cos\theta_1 - f_{LV} \quad (2\text{-}8)$$

With this being said, the author of the present work recommends that for contact angle measurements, the solid surface be as smooth and inert to the liquid as possible to avoid the need to implement a surface correction factor. This is due to the fact that there are no general guidelines that define how smooth a surface must be to prevent roughness becoming a key factor in contact angle identification.

2.1.3 Methods of Contact Angle Measurements

There are several methods for experimentally measuring the contact angle, such as the tilting plate method, Wilhelmy balance method, measurement by telescope-goniometer, capillary rise at the vertical plate, capillary penetration method for powders and granules, and capillary bridge method. However, the method employed for contact angle experiments in this work is called the captive bubble method. The captive bubble

method involves immersing a solid sample in a testing liquid such that an oil bubble can be formed underneath the sample. This technique was first introduced by Arthur F. Taggart (1951). It provides direct and meaningful measurements of the contact angle. The mechanism usually works by injecting a small amount of oil into the liquid of interest, such that an oil bubble is formed beneath the sample. In order for the experiment to be successful, it is important that the needle be kept in the bubble throughout the measurement time. This is because just like with the sessile drop method, the balance of the advancing angle can be deeply affected by any disturbance. It also provides stability, so that the bubble does not drift over the solid surface when the plane is not perfectly horizontal.

The advantage of this method is that it requires the solid sample to be submerged in the liquid, which sequentially ensures that the substrate is in contact with a saturated atmosphere. The captive bubble method also minimizes the risk of contamination of the solid-air interface that may form as a result of airborne oil drops. Additionally, it provides simpler and more explicit ways of investigating the dependence of the contact angle on temperature, since it is more perspicuous to monitor the liquid's temperature via the captive bubble method than by sessile drop. The results obtained for smooth polymeric surfaces by the sessile drop and captive bubble methods have been found to be in compliance (Zhang, Wahlgren and Sivik 1989). However, the captive bubble technique bears some weaknesses, such as requiring a far greater amount of liquid than the sessile drop method. Also, swelling of the solid surface upon immersion and continuous

dissolution of the surface film by the liquid give rise to different degrees of intricacy in the captive bubble method.

2.2 Interfacial Tension

Various processes have been developed to measure the interfacial tension (IFT) of liquids. IFT measurements have been divided into two fundamental categories: static and dynamic. Static methods (e.g., pendant drop, sessile drop) involve the droplet being in an equilibrium shape in a forcefield that tends to deform the droplet, such as gravity or centripetal force. Moreover, the force of interfacial tension tends to minimize the surface area of the droplet. The difficulty with these methods lies in acquiring accurate density measurements for the liquid of interest and its surrounding phase. Also, this process requires a lengthy wait time until equilibrium is reached, depending on the liquid tested. Highly viscous liquids with additives and gelling agents like polymers may be the most affected by static measurements of IFT, since they are more prone to the thermal degradation that occurs over long wait times. Dynamic methods, however, involve continuous observation of the shape of the thread breakup and retraction of elongated droplets to an equilibrium shape. In the present research, the pendant drop method was used to measure interfacial tension.

2.2.1 Pendant Drop Method

Pendant drop is the most widely used method for interfacial tension measurements in the petroleum industry, due to its simplicity, accuracy, and reliability. The mechanism of this method functions simply by suspending a droplet of a heavier liquid in a bulk of a lighter liquid phase. Thereby, the droplet is kept suspended from a spout, narrow tube, or

tip of a syringe at the point where a balance between gravity and interfacial tension is reached. The shape and size of the droplet are governed by the predominant IFT between the given fluids. The interfacial tension values integrated by the Laplace equation for capillarity are quantified from the static droplet profile for a certain density difference across the two phases (i.e., gas-liquid or liquid-liquid). The images of the droplet are typically captured and analyzed using a video system.

However, determination of IFT values using the pendant drop method is constrained by a few assumptions. For instance, the drop is assumed to be symmetrical around a central vertical axis, which makes viewing the drop possible from all angles. Also, the drop is in a completely static and motionless condition. Thus, the dimensions of the droplet are only governed by gravity and IFT forces. Despite these assumptions, the pendant drop method yields accurate and reliable results. Such advantageous results emanate from the simplicity and usefulness of the technique. The apparatus for the pendant drop method does not require any calibration. Also, the method can be performed on Newtonian and viscoelastic fluids alike; no assumptions are needed for the rheological behavior of the fluid. One potential drawback of the method, however, is that it requires accurate knowledge of the densities of the materials utilized for the experiment, so that valid and credible results are generated.

2.2.2 Young-Laplace Equation for Surface Tension Measurements

The Young-Laplace equation relates the Laplace pressure across an interface with curvature and interfacial tension. It provides concrete and tangible results for all static measurements of interfacial tension, and is given by **Eq. (2-9)**:

$$\Delta P = (P_{in} - P_{out}) = \gamma\left(\frac{1}{R_1} + \frac{1}{R_2}\right) \quad (2\text{-}9)$$

where ΔP is the capillary difference across the curved interface, and R_1 and R_2 represent the principle radii of the curvature.

The asymmetrical drop shape analysis approach relies on the Young-Laplace equation of capillarity to compute surface tension. As surface tension minimizes the surface area of the droplet to form a spherical shape, the gravitational force elongates the droplet, which causes a pressure difference in the z-direction, following Pascal's law for hydrostatic pressure. Therefore, in the presence of gravity as the only external force acting on the droplet, the pressure difference becomes a linear function of elevation and is given by:

$$\Delta P = P_0 + \Delta\rho g z \quad (2\text{-}10)$$

where $\Delta\rho$ is the difference between the drop phase density ρ_d and continuous phase density ρ, g is the gravitational force, and z represents the vertical height from a reference point. For the pendant drop, the principle radii of the curvature at the apex becomes ($R_0 = R_1 = R_2$), and for every point above the reference, $R_2 = \frac{x}{sin\,\varphi}$. The Young-Laplace equation then becomes **Eq. (2-11)**:

$$\gamma\left(\frac{1}{R_1} + \frac{\sin\emptyset}{x}\right) = \frac{2\gamma}{R_0} + \Delta\rho g z \quad (2\text{-}11)$$

The Young–Laplace equation can be obtained as a set of three first-order dimensionless differential equations with three boundary conditions in terms of the arc length s measured at the drop apex.

$$\gamma\frac{d\emptyset}{ds} = 2 - \beta z - \frac{sin\,\emptyset}{x} \quad (2\text{-}12)$$

$$\gamma \frac{d\emptyset}{ds} = 2 - \beta z - \frac{sin\,\emptyset}{x} \quad (2\text{-}13)$$

$$\frac{d\emptyset}{ds} = 2 - \beta z - \frac{sin\,\emptyset}{x} \quad (2\text{-}14)$$

where β is the Bond number that represents the shape of the drop and is given by $\frac{\Delta\rho g {R_0}^2}{\gamma}$. Note that the Bond number is positive for oblate droplets such as bubbles below the substrate and meniscus in a capillary, and negative for prolate droplet such as pendant drops. The three boundary conditions associated with the equation are:

$$\emptyset(s = 0) = z(s = 0) = x(s = 0) = 0 \quad (2\text{-}15)$$

2.3 Zeta Potential

Zeta potential (ζ potential**)** is the potential change in electrochemical equilibrium that occurs when two different phases (such as a liquid and solid) come in contact with one another. The liquid phase is generally the polar phase, having at least a single molecule with a permanent dipole moment. Contact between the liquid and solid phases causes the liquid's dipole molecules to lean in a particular direction at the interface. Thus, if the solid phase has a positive charge, the surface's electrostatic potential becomes positive if the liquid phase is not charged, such as with distilled water. The ζ potential of an inert aqueous solution should be zero, due to the absence of charged solid particles or ions in the solution. Nevertheless, this is not always the case, since even particles as small as 1nm to 100μm can contaminate the sample.

Following this principle, if the aqueous solution is charged and thus contains dissolved ions, the electrostatic potential changes in the interface, becoming constant far

from the solid surface interface. Inert solid surfaces tend to attract electric charges when they come in contact with liquids. Thus, the presence of charged ions on the solid surface is not a necessity for charge formation. For instance, an inert surface has a negative charge because of the preferential adsorption of hydroxide ions coming from the liquid phase. This behavior is often explained by using the electrochemical double layer (EDL) model. Based on the double layer model, the potential ζ value for a pure liquid is most likely zero, unless the sample is significantly contaminated with solid particles such as dust. When a solid surface comes in contact with a liquid phase, the solid surface becomes charged; this, in turn, increases the surface potential. The surface potential decreases in magnitude and eventually become constant far from the solid surface interface. In this context, "far" means distances greater than 5nm to 200nm (Hunter 1981).

2.3.1 Measuring Zeta Potential

The most common method for measuring ζ potential is based on the principle of phase analysis light scattering (PALS). Conventional laser doppler electrophoresis (LDE) instruments measure frequency changes in the scattered light that occurs because of solid particles' movement in an electric field. The measured velocities of suspended particles are typically very small, less than 100 microns/second, which results in minor frequency changes. Thus, LDE and correlation techniques are limited to measuring high mobility particles. In other words, when the displacement of particles is less than the reciprocal of the scattering vector $\boldsymbol{[K^{-1}]}$, the signal will not result in a complete cycle; therefore, it cannot be measured accurately using LDE. To overcome this limitation, small displacements are measured by waiting for long periods of time, until they're comparable

with $\boldsymbol{[K^{-1}]}$. This approach, however, is deemed inconsistent and could be damaging, since the application of an electrical field in one direction for an extended amount of time – anything more than a couple seconds – can lead to electrode polarization. Also, applying a high voltage to offset the time needed for small displacements to be comparable with $\boldsymbol{[K^{-1}]}$ induces significant Joule heating, which is not desirable in an electrophoresis experiment.

PALS utilizes the same method as the conventional LDE, but it determines the phase shift (i.e., frequency x time) instead of frequency change. The frequency shifts $\boldsymbol{(\Delta f)}$ and $\boldsymbol{[K]}$ are defined as shown in **Eqs. (2-16)** and **(2-17)**, respectively:

$$\Delta f = \frac{2v\sin(\frac{\theta}{2})}{\lambda} \qquad \textbf{(2-16)}$$

$$[K] = \frac{4\pi n}{\lambda}\sin\left(\frac{\theta}{2}\right) \qquad \textbf{(2-17)}$$

where v is the particle velocity, λ is the laser wavelength, θ is the scattering angle, and n is the refracting index.

The phase shift changes with changes in the position of the particles. In a PALS electrophoresis experiment, a higher frequency is applied compared to that used in a conventional LDE. The phase change tends to oscillate, due to the difference between the actual and Doppler frequencies of a zero-mobility particle, typically referred to as the reference or modulation frequency. Thus, measuring the phase change between the actual and modulation frequencies more accurately determines the difference in position of the particles when mobility is low. A clear example is presented by analyzing four synthetic waves at two different frequencies. Plotting the phase difference between the two waves

results in a flat line when the frequencies are the same. However, a plot of the phase difference between two different waves, in our case 50 Hz and 60Hz, results in an increasing gradient, as shown in **Figure 2-4**.

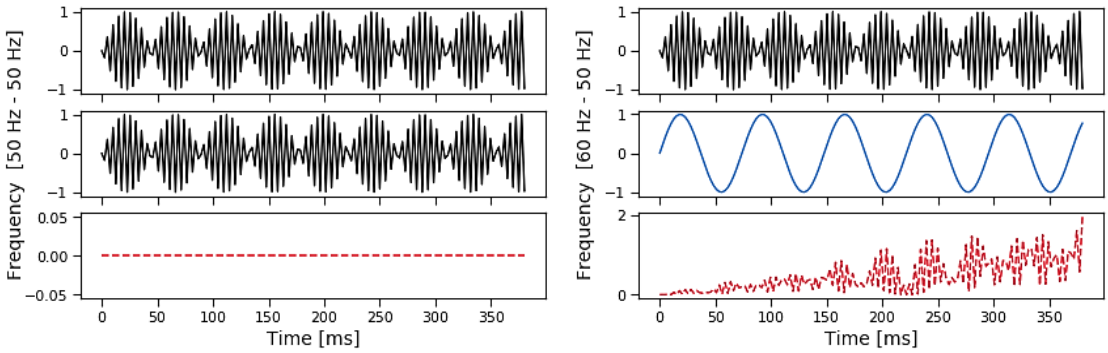

Figure 2-4 Schematic diagram showing the residual difference between two waves (50 Hz and 50Hz) on the left and (50 Hz and 60Hz) on the right.

The rate of change in the phase difference is a function of the particle's velocity. Thus, the average value of the ζ potential can be obtained (McNeil-Watson, Tscharnuter and Miller 1998). PALS is integrated into Brookhaven Instruments, as shown in **Figure 2-5**, increasing the measurement sensitivity by three orders of magnitude compared to the LDE method. However, it is imperative to state that most commercial instruments, including ZetaPALS, are made to be user-friendly. Users often overlook the complexity of the measurement because of the overly simple integrated PALS method. This notion that one can "walk up, put a sample in the chamber, and press a button" results in an apparent lack of understanding of the integrated technique and its limitations. Many common measurement errors arise from not having enough particles (often referred to as "sample count" in commercial instruments), sample contamination in nanodot samples, or simply because the particles are too small to be measured.

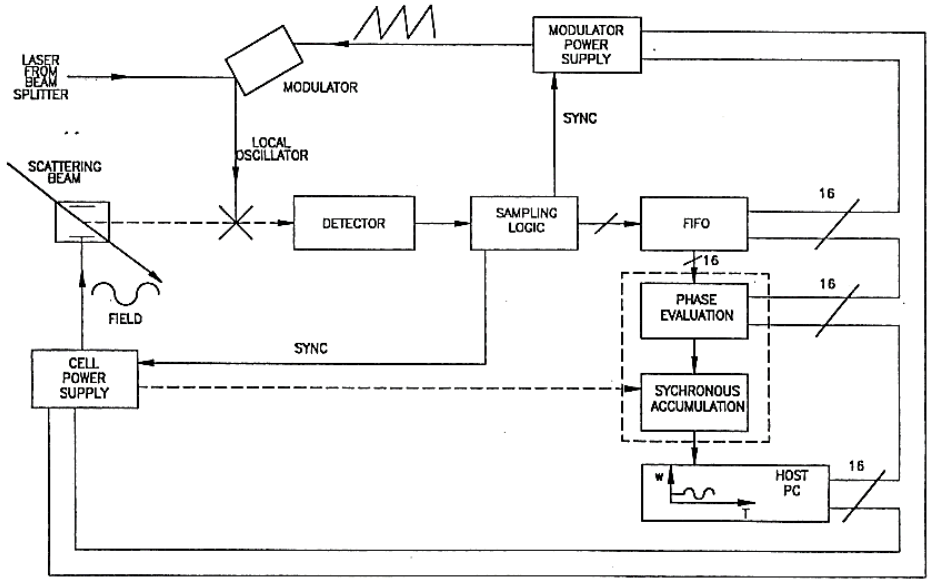

Figure 2-5 PALS schematic as depicted by McNeil-Watson, Tscharnuter, and Miller (1998).

2.3.2 Zeta Potential Applications

Electrophoretic mobility measurements and the resultant ζ potential have various applications ranging from biomedical uses such as helping to characterize the surfaces of bacteria, blood cells, and viruses, to certain industrial uses. They play an important role in the study of the flocculation process, assisting in the filtration of water contaminants. In this study, the main focus is the application of ζ potential to enhanced oil recovery (EOR) in the petroleum industry. The ζ potential provides crucial input regarding the stability of surfactant solution films on rock surfaces. Many EOR researchers have used ζ potential to study the stability of surfactant solutions as charges for oil, water, and rock when determining the thickness of the double layer between a solution and rock interface (Hirasaki 1991). Mostly, they have studied the stability of dispersed rock particles in surfactant solutions. A range of ζ potential values denoting stability levels is available, with ±30 mV being the "cutoff" for indicating a stable dispersion.

These stability levels were discussed by Riddick (1968), who explained that such levels could apply to colloids with fairly large particle diameters, and may not be suitable for nanomaterials. Therefore, an absolute ζ potential value denoting stability applies only in purely electrostatically stabilized dispersions, and even in this case, there are exemptions. In this context, the surface properties of solutions are related to their half-life stability. According to Losso et al. (2005), the half-life stability of a solution with a ζ potential of −11 mV was shorter than that of a solution with a ζ potential of −53 mV, indicating that solutions with higher ζ potential values are more stable in the long run than are solutions with low ζ potential values. Applying this concept to surfactant solutions, stable surfactant solutions sharing the same composition tend to have higher ζ potential values when mixed with the same rock particles. Indeed, other conditions such as pH level, particle size, sample count number, and conductivity also have to be the same.

2.3.3 Zeta Potential and Wettability

Some authors have claimed that there is a relationship between wettability and ζ potential. In theory, CA is complex; however, it is often used to explain the interactions among oil, rock, and brine, and any chemical EOR solution in the form of wettability. It is worth noting that both CA and IFT are discussed in detail in a separate chapter of the present research. In the current chapter, the relationship between ζ potential and wettability is investigated. Alvarez and Schechter (2016) found that higher ζ potential values result in more water wetness. In their work, five different surfactants were evaluated, with the objective of finding the best-performing surfactant additive that also promotes higher imbibition recovery in Bakken. CA, along with IFT and ζ potential, were

measured for every surfactant. Their findings showed that the ζ potential values increased with increases in surfactant concentration. Also, higher ζ potential values correlated with lower CA values, indicating more water-wetness.

Following a similar logic, unstable solutions denote intermediate-wet systems and low ζ potential magnitudes. This hypothesis is valid only if charges affecting CA are the same charges influencing the electric potential at the EDL. An electric field exists around the three-phase contact area, and the rock-oil interfaces are responsible for its activation. In this electric field, the distribution of electric potential around this area is related to the distribution of the electric charges at the contact region. Various factors such as the volume of oil drop that influences IFT, original charge of the rock surface, surface smoothness, and adsorption of solutions into the rock surface all affect the distribution of electric charges. With this in mind, many complexities prevent establishing a clear link between ζ potential and CA. Lu, Najafabadi, and Firoozabadi (2017) investigated CA and ζ potential via experimental and molecular simulations, but did not find a clear link between ζ potential and CA, even though in theory they are close.

Their findings can be attributed to the fact that ζ potential is not measured at the oil-solution and solution-rock interfaces of a solution film, but rather far away from the solution-rock interface. In such cases, the measured ζ potential values are linked to the interfacial charges away from the solution-rock interface, which is further than the region where CA is measured. A flat rock chip needs to be in contact with an aqueous solution and oil to measure CA. The aqueous solution is adsorbed into the rock chip, causing an alteration in the charge influenced by the charge of the solution-rock and oil-solution

interfaces. As shown in **Figure 2-6**, the charges tend to favor the repulsion of the two interfaces, resulting in a thicker film that causes the rock surface to be more water-wet. The rock-solution and solution-oil charges are difficult to determine through electrophoresis experiments. The ζ potential values for rock-solution and oil-solution are most likely not equal to the charges from the rock-solution and solution-oil charges of the created film.

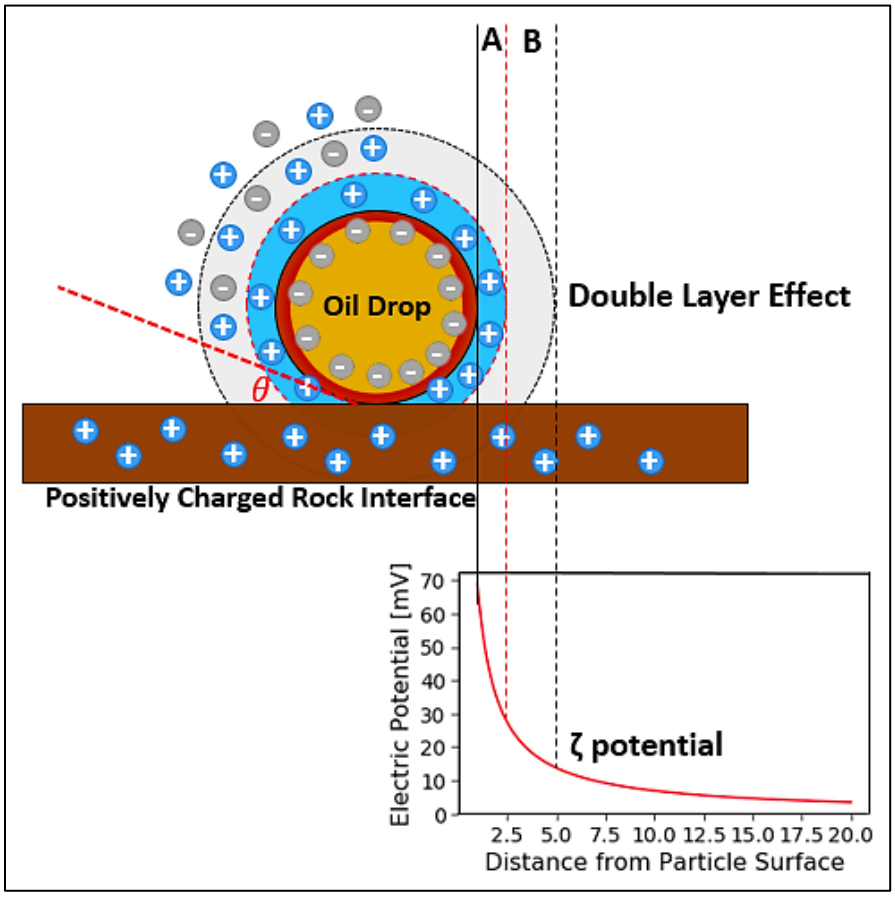

Figure 2-6 Schematic of a negatively charged oil drop and thin, negatively charged particle on a positively charged rock surface. (A) denotes the stern potential, while (B) indicates the slipping plane.

2.4 Surfactant-Assisted Spontaneous Imbibition

Surfactant-assisted spontaneous imbibition (SASI) is a method for improving the recovery of oil by adding a surfactant to the imbibition fluid. Surfactants have multiple

distinctive amphiphilic attributes that attract to both oil and water molecules. The molecular nature of a surfactant causes a significant reduction in IFT and wettability alteration in the oil-water-rock interface. According to research conducted by Rassenfoss (2017), the field-scale effect of SASI produced 15% to 20% of the entire field-scale performance. Alvarez, Tovar, and Schechter (2017) and Alvarez, Saputra, and Schechter (2017) tested the SASI approach to improving oil recovery in rock and oil samples collected from the Wolfcamp formation. Four different surfactants were tested: nonionic, nonionic/cationic, anionic, and nonionic/anionic. The charge carried by the hydrophilic head of the surfactant molecule was the main difference among the four tested surfactants. Nonionic surfactants have neutral heads, anionic surfactants have negatively-charged heads, cationic surfactants have positively-charged heads, and mixed surfactant blends normally have two types of surfactant molecules.

Spontaneous imbibition experiments performed on the quartz-rich Wolfcamp rocks demonstrated that production from SASI ranged from 29% to 34% of the original oil in place (OOIP), while experiments with solutions not mixed with a surfactant produced oil from OOIP in the range of 7% to 10%. Wettability tests indicated that the anionic surfactant altered wettability to the water-wet region. Notably, adding surfactants yielded the best recovery results, proving a direct link between the amount of oil produced and wettability. The Wolfcamp formation consists of two types of rock lithology: quartz-rich and carbonate-rich. Anionic surfactants were found to work best in the quartz-rich rock sample, while altered cationic surfactants produced the most substantial amount of oil compared to the anionic surfactant used in the carbonate-rich environment. The

contrast between the two lithologies indicates that each rock type reacted differently to different surfactants.

To develop an optimum surfactant solution selection workflow, it is crucial to understand the mechanism behind how surfactant-assisted spontaneous imbibition works. Imbibition is the scientific name given to the absorption process that takes place between rocks and water in mining. Three main forces drive this kind of process: capillarity, viscosity, and gravity (Menouar and Knapp 1980). In this study, the viscous force was eliminated because it is mainly created by pressure differences applied to the tested sample. Although pressure differences do exist in the field in the form of pressure drawdown, laboratory studies of spontaneous imbibition do not include pressure applied to the sample due to the primary objective of analyzing the effect of capillary forces in oil recovery. Therefore, viscous force is disregarded as a possible driving force of imbibition, leaving the driving mechanism of spontaneous imbibition to be capillary in nature or gravity-dependent.

Significant debate surrounds the action of gravity and capillary forces in the exchange of oil and water during the process of imbibition. Some scientists have argued that the difference between the densities of the oil and aqueous phases invokes imbibition caused by gravity. The lighter oleic phase floats, causing imbibition to occur at the bottom of the core. Such a pattern has been observed by incorporating a direct visual inspection of the core after the imbibition process. CT scans of the core sample have demonstrated fluid distribution and movement inside the core plug. Standnes and Austad (2003) conducted an experiment using an oil-saturated chalk core with a low IFT (0.1mN/m)

surfactant solution. The results showed that the imbibition of water took place at the bottom part of the sample. Other experiments conducted by Standnes and Austad (2003) showed a radial fluid production pattern in capillary-dominated imbibition.

Although Parsons and Chaney (1966) and Xie et al. (2005) did not include observations in their final results, they acknowledged that capillary force was the main driver in the imbibition experiments they performed. Movement of water into the rock in a radial manner is clear evidence that both fluids observe a counter-current movement, allowing interaction between them (Babadagli, Al-Bemani and Boukadi 1999; Cuiec, Bourbiaux and Kalaydjian 1994). Similar results were observed with water in CT scans run for a spontaneous imbibition study. According to Alvarez, Saputra, and Schechter (2017), CT-scan images showed a distribution of density around the scanned image, since the CT number was directly proportional to the rock/fluid density. The water had a brighter color, since it was a heavier fluid than the oil. **Figure 2-7** shows CT slices with respect to time; simultaneous water movement can be observed at the bottom of each slice, while the oil floats to the top.

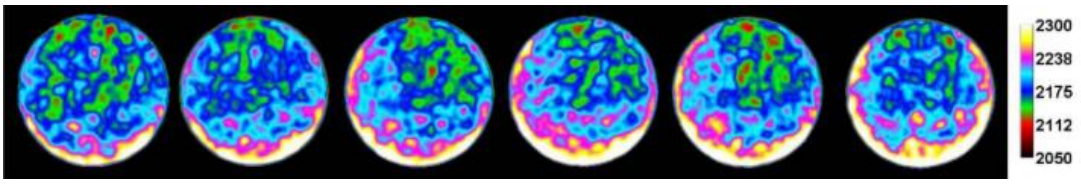

Figure 2-7 CT-scan image showing gravity-driven imbibition, reprinted from Alvarez, Saputra, and Schechter (2017).

Schechter, Zhou, and Orr (1994) concluded that both gravity and capillary forces could contribute to the spontaneous imbibition process. In their work, they defined the

transition between the dominance of one force to that of another through an expression called the inversed Bond number, $N_B{}^{-1}$, as defined by **Eq. (2-18)**. The $N_B{}^{-1}$ expression can be used as an indicator of the dominant force in the imbibition process.

$$N_B{}^{-1} = C\frac{{}^{\sigma}\sqrt{\frac{\phi}{k}}}{(\Delta p)gh} \tag{2-18}$$

where C is a representation of pore geometry, σ is the tension between the water and oil, ϕ is the porosity, k is the permeability, $\Delta\rho$ is the difference in density between the aqueous and oleic phases, g is the gravity constant, and h is the vertical length of the rock. An $N_B{}^{-1} < 1$ indicates that the gravitational force is the dominant force in the imbibition process. Conversely, an $N_B{}^{-1} > 5$ indicates that capillary force is the dominant driving force in the oil and water movement in the core plug. A value between 1 and 5 indicates that the two forces both contribute to the imbibition process.

Looking at the equation, reducing the value of interfacial tension will result in gravity taking control of the imbibition mechanism, while a low permeability value for the rock sample will result in a reverse effect, with capillary force dominating the driving force of the imbibition. This observation is crucial for the next part, where a surfactant and tight rock sample are included in the imbibition process. It is worth noting that the above equation was derived under the assumption that the rock sample would have an ultra-water-wet condition, which is mostly the case in clastic high-permeability reservoirs. Under this assumption, a reduction in IFT value by addition of a surfactant will shift the dominant force of imbibition from capillary to gravity. According to Schechter, Zhou, and

Orr (1994), a lower IFT will cause the gravitational force to overtake the capillary force in the process, as depicted by **Eq. (2-18)**.

Although water-wet rock samples rarely exist in the form of tight sandstone reservoirs, this study focuses on tight oil rock, which generally has an oil-wet wettability. It is essential to consider wettability when reviewing the driving force of spontaneous imbibition. Oil-wet surfaces not only restrict the flow of oil, but also trap oil in the pores, taking advantage of capillary force and ultimately reducing oil productivity. Addition of a surfactant to the system augments the imbibition process by causing a shift in wettability (Zhang et al. 2009). This was confirmed by several studies (e.g., Standnes and Austad 2003; Morrow and Mason 2001). A surfactant has exceptionally unique molecules due to their amphiphilic nature, which enables them to bond with both the polar and non-polar molecules, or in this case, both oil and water molecules.

Wettability alteration and IFT reduction are two of the most common parameters affected by adding surfactant to an oil-water-rock system. These two parameters are crucial in the sense of spontaneous imbibition, since IFT is an essential parameter in determining whether capillary or gravity forces dominate the imbibition process. Wettability and IFT also determine the strength of the capillary force that drives the movement of the oil and water. The strength of the capillary force can be defined by the Young-Laplace equation, as shown by **Eq. (2-19)**.

$$Pc = \frac{2\sigma \cos\theta}{r} \tag{2-19}$$

where wettability is represented by contact angle (θ), interfacial tension ($\boldsymbol{\sigma}$), and pore radius (r). Water-wet surfaces are represented by a contact angle < 90^o, which makes the capillary positive or favorable to expulsion, as explained above. Higher IFT values result in a stronger capillary force, which also increases oil production from capillary-driven spontaneous imbibition. The same implication can be obtained from a smaller pore radius. The presence of a surfactant as both wettability alteration and IFT reduction agent will affect the capillary pressure causing the spontaneous imbibition; therefore, an understanding of how surfactants impact both properties must be developed to enable the design and accurate modelling of surfactants' effect on natural imbibition.

There are four classifications of surfactant molecules, based on the charge carried on the heads of each. Anionic surfactants are surfactants with negatively-charged heads, cationic surfactants bear positive charges on their heads, nonionic surfactants have neutral heads, and zwitterionic surfactants possesses both negatively- and positively-charged heads. An oil-wet surface will have oil molecules adsorbed onto the surface and be dependent on the charge that the surface carries. In response, adsorbed oil molecules display different charges, as well. Negatively-charged surfaces cause adsorbed oil molecules to display positive charges, while positive oil molecules cause the adsorbed oil molecules to display negatively charged molecules.

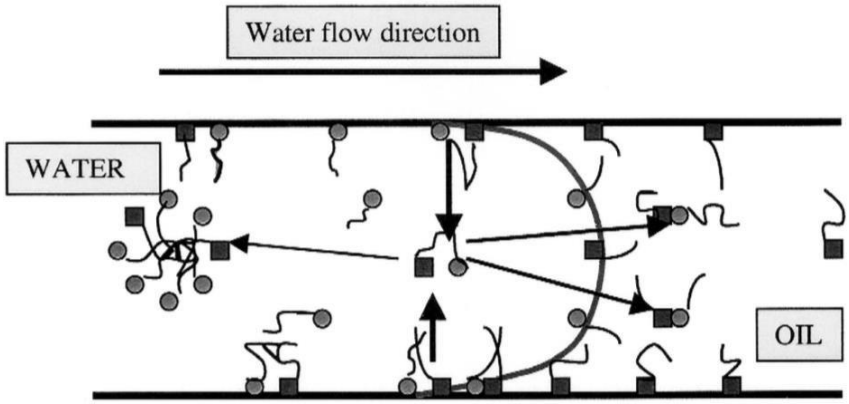

Figure 2-8 Ion pair surfactant-induced wettability alteration reprinted from Standnes and Austad (2003).

A cationic surfactant alters the wettability of the process by bonding the heads of surfactant molecules to positively-charged adsorbed oil molecules, forming ion pairs (Standnes and Austad 2003). The hydrophilic nature of the surfactant molecules formed causes pairs to detach from the rock surface, restoring its water-wetness. On a negatively-charged surface, the opposite occurs; positive charges are exhibited by the adsorbed oil molecules, and anionic surfactant forms the ion-pair configuration. The ion-pair mechanism is believed to cause the strongest wettability alteration, as permanent removal of oil molecules is involved in the mechanism (see **Figure 2-8**). Nonionic surfactants work differently because of the absence of the dominant charge on their heads. This condition results in a lack of ability to form ion pairs. The hydrophobic tail bonds with the adsorbed oil molecule, creating twin layers of the molecule on the rock surface (Salehi, Johnson and Liang 2008). The hydrophilic part of the surfactant molecule faces the pore space in the oil-surfactant double layer configuration, causing the surface to be water-wet (see **Figure 2-9**).

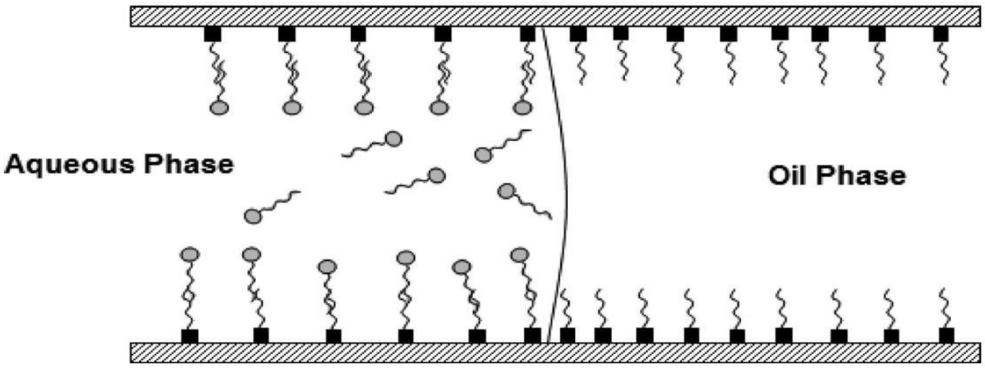

Figure 2-9 Double layer adsorption surfactant-induced wettability alteration reprinted from Salehi, Johnson, and Liang (2008).

The double layer mechanism also causes wettability alteration when similar charges of surfactant and adsorbed oil molecules are found. Temporary alteration is often related to the double layer mechanism, mainly because the bond between the adsorbed oil molecule and hydrophobic surfactant tail is relatively weak.

Adding a surfactant to the water also reduces the surface tension between the water and oil. The tension that exists between the two liquids is the energy needed to develop a new interface between the two phases. This energy is calculated by combining the surface energy of the two different fluid phases, and then subtracting the interaction energy (as explained in the surface tension section of the present research). Therefore, the result of the interaction energy defines the energy to the molecule in the bulk phase and the interaction energy to the molecule in the other phase (Rosen 2004). The surfactant molecule positions itself on the surface, replacing molecules on the interface; the hydrophilic head faces the aqueous phase and the hydrophobic head faces the oleic phase. This configuration causes an increase in interaction, since the surfactant molecule has a higher affinity for both fluid phases as compared to the original molecule on the surface.

2.5 Pore Size Distribution and Imbibition

A pore is the void space within the matrix of a porous medium. The presence of this pore structure within naturally occurring porous materials creates a distribution of pore spaces often referenced by the pore size distribution (PSD). In this research, nuclear magnetic resonance (NMR) was used, along with scanning electron microscopy (SEM), to understand the effect of PSD on the oil recovered by SASI, since almost every mechanism occurring in the porous medium is directly or indirectly affected by PSD. NMR is a form of spectroscopy that relies on the study of the interaction of light matter. Certain atomic nuclei exhibit a nuclear spin, subjecting molecules to an external magnetic field followed by light irradiation. This results in a unique behavior of light interaction with the subject compound. Such unique behavior can assist in the understanding of oil, gas, and water molecules' nanoscale-level interactions with rock surfaces.

Advanced static and dynamic NMR rock characterization can even be used to validate simulations by determining how much unbound and bound fluids are contained in the pores. The applied magnetic field's electromagnetic pulses manipulate the hydrogen atoms' magnetic moments, causing a sort of disruption. The atoms' magnetic moments get back to their original status through relaxation, which can be detected by NMR because different relaxation times transpire depending on the molecule and environment. In this case, NMR can be used to detect the response of hydrogen atoms (i.e., protons) in a magnetic field. A property of hydrogen known as spin causes hydrogen protons to act as small bars in the presence of an external magnetic field. The protons line up either parallel or perpendicular to the external field's lines of force. They are then forced to jump onto

another plane, the transverse plane, by applying a pulse sequence to them. The excited protons in the transverse plane emit energy until they return to their original equilibrium status and the signal in the transverse plane disappears.

NMR measures two properties: the strength of the signal and relaxation time characteristic. The characteristic time can be either the time the signal takes to return to its equilibrium value in the direction of the external field (T_1), or the time the signal takes to disappear in the transverse plane (T_2). Bulk relaxation is a fluid property that expresses how easily protons emit energy to one another, and can be expressed as follows: $1/T_2$ and directly proportional to η/T, where η is the viscosity, T is the absolute temperature in degrees Kelvin, and $1/T_2$ is the rate of bulk relaxation.

2.5.1 NMR Measurement

There are two primary sources of NMR signals in a porous medium: (1) the fluid far from the pore walls, and (2) the fluid on the walls of the pores. The first source gives NMR signals similar to those from bulk fluids, and is represented by lengthy relaxation times. The second fluid source, however, undergoes adsorption with the formation, which reduces the NMR relaxation time. Following this concept, a sample of fluid, core plug, or saturated core plug is essentially put under a magnetic field and excited using radio waves, depending on the required NMR signal. Different nuclei resonate at different radio waves at the same field strength, based on their nuclear magnetic moments. The processional frequency (i.e., the Larmor frequency) is a function of the magnetic field strength and can be calculated using the Larmor frequency equation:

$$\nu = \gamma . B \tag{2-20}$$

where B is the magnetic field strength measured in Tesla, $\boldsymbol{\nu}$ is the processional frequency measured in Hz (1 Hz = 1 cycle/second), and $\boldsymbol{\gamma}$ is the ratio of the magnetic momentum to its angular momentum measured in rad·s^{-1}·T^{-1} or MHz·T^{-1}. It is worth noting that the $\boldsymbol{\gamma}$ of the proton is around $2.675221900\ x10^8$ s^{-1}·T^{-1} or 0.42577478 MHz·T^{-1} and can be treated as a constant.

Protons resonate at 900 MHz under a 21 Tesla magnetic field, and thus 21 Tesla is often referred to as 900 MHz, following the Larmor frequency equation. Different waves with multiple frequencies ranging from about two million cycles per second (2 MHz, 0.046 T) to 21 million cycles per second (21 MHz, 0.49 T) are often applied to excite the nuclei in petrophysical applications. Higher frequencies are used for circumstances where a higher sensitivity is required, such as extremely low porosity samples. An NMR signal appears immediately following application of the magnetic field. The amplitude of the signal provides an indication of the total amount of fluid contained in the porous medium, whereas the time for the signal to disappear in the transverse plane (T_2) provides some insight into the porous medium where the liquid is contained. The dominant effect comes from the bulk fluids in larger pore throats, resulting in a larger area under the curve when integrating the relative signal with respect to time. In smaller pores, however, the fluids close to the pore walls tend to dominate the NMR signal, resulting in a smaller area under the curve when integrating the relative signal with respect to time.

Once the relative signal is obtained with respect to time, due to the magnetic field applied to a confined fluid sample or saturated core plug, inversion is applied to convert

the NMR signal and break it down into multiple relaxation times to create a normal distribution. NMR inversion is a very complex technique that requires solving the discrete Fredholm integral equation. There are multiple approaches to apply inversion to NMR signals, such as the truncated singular value decomposition, least-squares decomposition, and the Butler–Reeds–Dawson (BDR) methods. The most common approach to estimating solutions for the Fredholm integral equation and applying the optimum amount of smoothing based on the available NMR signals is the BDR approach (Butler, Reeds and Dawson 1981).

The outcome of the inversion process is a time distribution showing the population of the measured (i.e., T_1 and T_2) relaxation times that constitute the combined NMR signal obtained from the core. Since lengthy relaxation times come from large pores and short relaxation times come from small pores, the time distribution obtained from the inversion process represents the PSD in the core. Ideally, there is one (i.e., T_1 and T_2) component for each unique pore space in the core. However, when conducting spectroscopy experiments for special core analysis (SCAL), analyses are usually set to a maximum of about 256 individual (i.e., T_1 and T_2) components for each pore space, depending on the required analysis.

2.5.2 NMR Applications

There are many applications of NMR in the petroleum industry. NMR has been used in open hole logging for the past 40 years. The primary use of NMR in logging is identifying moveable and bound fluids contained in a porous medium. Moveable fluid denotes pore spaces excluding clay-bound water and bound water that are not moveable

in the NMR sense. The moveable fluid amount obtained through NMR may or may not represent the actually moveable oil or gas in the oilfield. Residual hydrocarbon saturations, including heavy oil and bitumen, can appear as part of the moveable fluid in the spectroscopy measurement. However, this limitation can be mitigated by using higher processional frequencies. Thus, modern tools can provide accurate estimations of the effective porosity by summing the irreducible and moveable fluids contained in the rock without the need for shale or resistivity correlations. Nevertheless, even though NMR logs can provide extensive information for identifying zones with moveable and bound fluids, they are still relatively rare to come by due to being highly costly and time-consuming.

The use of NMR has become widespread in SCAL conducted in laboratories, due to its nonintrusive nature. Cores are often hard to come by, and crushing them is the most widely used method for obtaining many rock properties. Also, permeability is difficult to calculate without a coreflood system. It becomes even more difficult to obtain for tight rocks because injecting fluid into them is time-consuming and in most cases almost impossible. For this reason, researchers often use NMR to determine PSD prior to and after core flooding and recovery analysis. NMR permeability is a reliable replacement for effective permeability and can be estimated from the relaxation time by using either the Timer-Coates (Coates et al. 1991), Kenyon, or Schlumberger models. One advanced NMR use for core analysis that has emerged recently is the determination of P_c. There are multiple ways to obtain P_c from NMR. The most common method built into most NMR software involves saturating the core with a single fluid and scanning it using 1D NMR. The core is then spun in a centrifuge, changing the fluid distribution contained within the

core. Then, another 1D measurement is carried out. The above steps are repeated at different centrifuge spin speeds. The P_c value is then calculated based on the centrifuge speed and changes in the NMR saturation profile. In the end, NMR is able to provide an accurate estimate of multiple SCAL outcomes ranging from PSD to capillary pressure calculations, which makes it an effective core analysis tool for EOR research purposes.

2.5.3 Relaxometry and Imbibition Distribution

The published works regarding the effect of PSD and rock texture characteristics on the SASI mechanism are scarce, at best. Extensive effort was expended searching for research articles pertaining to this subject, without success. However, some recent experiments were described in the literature that were performed in an effort to understand the mechanism of spontaneous imbibition in tight formations through the use of NMR. Kesserwan et al. (2016) presented an experimental study that employed NMR technology to establish a comparison between organic-rich carbonate shale from the Eagle Ford (EF) and Middle East (ME) formations. Both were found to consist mostly of calcite (i.e., were carbonate-rich), along with different amounts of other minerals such as clays and TOC. Spontaneous imbibition experiments, however, were conducted using 5% KCl brine and diesel for the key purpose of determining the wetting behavior of the EF and ME samples. Imbibition rate, as well as the amount of fluid imbibed, were obtained using NMR T_2 measurements, and the results were plotted depending on the rock structure, fluid imbibition type, and direction of imbibition.

After fluid imbibition experiments were performed, it was found that both the EF and ME samples successfully imbibed brine; therefore, these organic-rich shale samples

were of a mixed wettability. Experiments also showed that EF samples imbibed the brine faster than the diesel, whereas the ME samples imbibed the diesel faster than the brine. However, the reason for such results was not discussed. Furthermore, the brine was observed to continuously gravitate towards the large pores, while the diesel drifted into smaller pores in the ME samples. The opposite was observed in the EF imbibition samples; the diesel imbibed into large pores, while the brine invaded the smaller pores.

Lyu et al. (2018) conducted an experiment under all face open boundary conditions in an effort to understand fluid distribution in tight formations after the imbibition process. Their work revealed that the rate of volume change during the imbibition process based on the NMR peak analysis was not the same, indicating a difference in imbibition between small and large pores. A limitation of their work, however, transpired from failing to explain the displacement process with regards to the decrease in overall volume after imbibition. Such a limitation hinders understanding of the mechanism as a condition of volume conservation, and almost a 1:1 displacement was not met, based on the NMR peaks shown in their work.

Another experimental and analytical study was conducted by Ren et al. (2019), with the objective of investigating the imbibition behavior of fracturing fluid and understanding the effects of certain fundamental parameters such as interfacial tension, permeability, oil viscosity, and the salinity of the imbibition fluid. Their work confirmed the exitance of an optimal interfacial tension range corresponding to maximum imbibition recovery. They also concluded that during imbibition, the oil produced from larger pores, termed “moveable oil,” was equal to that from smaller pores, termed “irreducible pore

throat space." This conclusion is different from that arrived at by Lyu et al. (2018), where the majority of the movement/displacement during imbibition was found to occur in small pores. Such a discrepancy in conclusions mandates a thorough investigation that includes a sufficient number of samples. This will increase precision and preserve the constituency of the results. Both of the above-mentioned studies included a couple of tests. It is worth noting that a small sample size can result in a wide confidence interval, or in other words, a higher risk of error in statistical hypothesis testing.

CHAPTER 3

EXPERIMENTS AND METHODOLOGY

In this chapter, all experiments and measurements pertaining to wettability alteration and the addition of surfactants are presented, along with the methodology and results. This includes an analysis of the core samples and oil used throughout this work. The rock analysis encompasses the geological information for the reservoir from which the samples were acquired, rock sample preparation, X-ray diffraction, and oil density measurement. The next section discusses the fluid systems employed in this study, including a description of each fluid and its concentration. The contact angle is addressed next, followed by the interfacial tension measurements. The ζ potential concept and measurements are also discussed in detail in this chapter. Finally, it is worth noting that due to the large number of experiments, along with the nature of the tight, low-quality rocks analyzed, data gathering and processing of the laboratory experiments took more than eight months to complete. However, the time-consuming nature of this approach was a minor price to pay for the amount of useful data obtained in the end, including descriptions of the rocks and oil, and useful data regarding the aqueous solutions tested.

3.1 Rock Samples

Sidewall core samples from two Wolfcamp oil wells in the Midland Basin area were obtained and used in all experiments, including: contact angle, ζ potential, surfactant adsorption, and spontaneous imbibition. The high price of sidewall core retrieval made the core samples a limited commodity and difficult to come by. Yet the use of sidewall cores the in laboratory experiments was crucial, as they are the most representative of the

condition of the rocks intersected in horizontal drilling. Matching oil was acquired from a sounding well intersecting the same formation.

The same oil was used across all experiments, in order to preserve the natural compatibility between the reservoir rocks and formation oil used. In this work, 10 sidewall core samples and several crushed and chipped rocks were received. Cores 1" in diameter and with different lengths were used for spontaneous imbibition; crushed, chipped, polished, or trimmed rocks were used for ζ potential, surfactant adsorption, and contact angle measurements. The core samples were divided into two main categories: quartz-rich and carbonate-rich. The quartz-rich samples came from the same well at the same depth, while the carbonate-rich samples came from a different well at the same depth. The mineral composition for each general category was obtained using XRD, as shown in **Figure 3-1**.

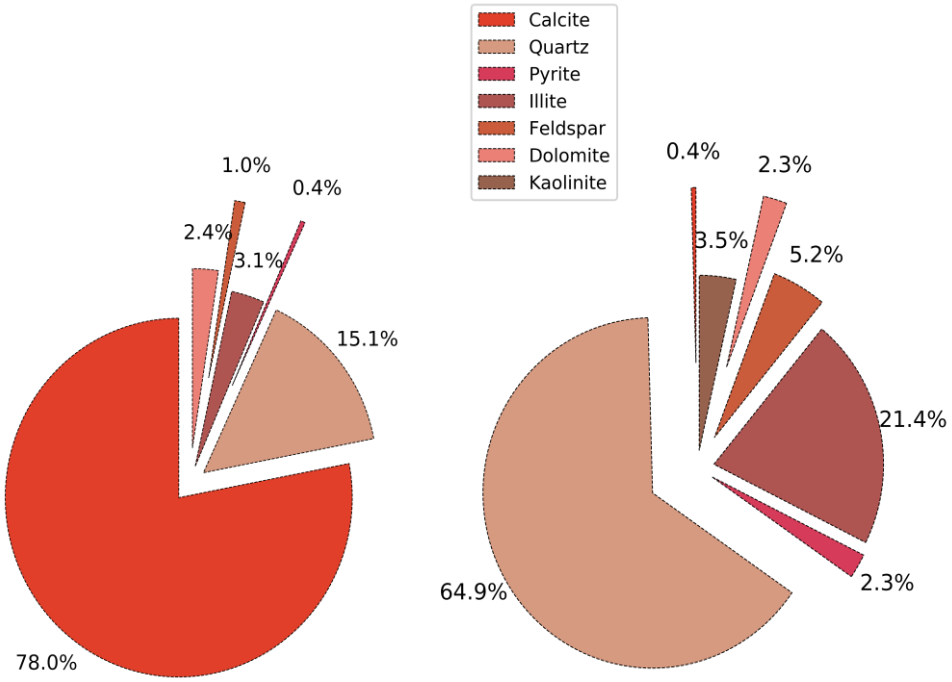

Figure 3-1 Average mineral composition of the quartz-rich samples (right) and carbonate-rich samples (left) obtained via XRD.

The carbonate-rich samples fell into the carbonaceous category, as their calcite content was almost five times that of the quartz. The quartz-rich samples had a significant amount of clay content in the form of illite, measured at approximately 21%. Some dolomite, feldspar, pyrite, and kaolinite minerals were also detected, but in small percentages. The importance of rock composition is apparent; it affects numerous parameters such as wettability, mechanical strength, porosity, and the amount of bound fluid contained within the rock. Even though the above-mentioned parameters are influenced by the rock composition itself, they can be related through correlations by comparing the trends presented in many other studies. **Table 3-1** shows the dimensions of each core sample, along with their masses after cleaning (i.e., drying) and density. The carbonate-rich core samples are denoted by the letter C, while the quartz-rich samples are indicated by the letter Q.

Table 3-1 Dimensions, clean masses, and densities of the core samples

Name	***Diameter, in***	***Length, in***	***Bulk Volume, cc***	***Mass After Cleaning, g***	***Rock Density, g/cc***
C1	0.9704	2.6784	31.4763	84.58	2.687
C2	0.9704	2.7158	31.9162	87.6	2.744
C3	0.9732	2.6284	31.0641	83.5	2.687
C4	0.9696	2.643	31.0092	84.99	2.74
C5	0.9696	2.2608	26.5252	71.93	2.711
Q1	0.9724	2.5413	29.9899	71.23	2.371
Q2	0.9972	2.0748	25.7493	62.548	2.429
Q3	0.9965	2.0736	25.6941	61.6049	2.397
Q4	0.9965	1.9579	24.2598	57.6821	2.377
Q5	0.9952	2.1572	26.664	64.796	2.43

3.2 Cleaning and Aging

It is most likely that the condition of the acquired core samples changed due to their becoming accustomed to other ambient conditions during transportation and packing. Also, the core samples weren't preserved in wax when they came in, which is another reason to suspect possible reservoir condition changes. Fluid saturation and wettability are two of the critical properties that may have changed; therefore, it was decided to clean the cores, vacuum them, and age them back into formation oil to reinstate their original condition. The wettability of a rock surface will most likely change to oil-wet when in contact with oil, due to oil adsorption. Following this concept, the original wettability (i.e., oil-wetness) of the reservoir rocks was restored by aging the core samples in oil. Before aging, however, the core samples and chips were cleaned, following the Dean-Stark method. The core samples were boiled for two weeks in toluene and one week in a methanol extraction in a Dean-Stark apparatus. The samples were then taken to the vacuum oven and dried for two weeks before being placed in saturation chambers at 8,000 psi, as shown in **Figure 3-2**.

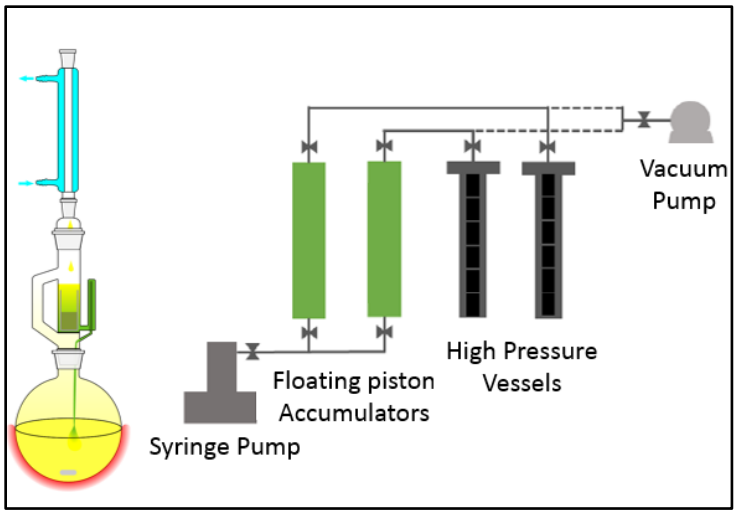

Figure 3-2 Dean-Stark apparatus schematic for core plug cleaning (left) and pressurized saturation vessels and pumps schematic.

3.3 Fluid Systems Description

3.3.1 Oil Properties

The oil used in this study was a Wolfcamp B dead oil. The density of the oil was measured at approximately 0.72-0.76 [g/cc] at 155°F; this was considerably light, as expected, because the oil was recovered from a well located in the Permian Basin targeting the lower Sparberry and upper Wolfcamp formations. The basic oil properties are tabulated below:

Table 3-2 Basic Wolfcamp B oil properties

Density at 60°F [g/cc]	0.82
Density at 155°F [g/cc]	0.72-0.76
API at 60°F [°]	39
API at 155°F [°]	56
Viscosity at 60°F [cp]	2.05
Viscosity at 155°F [cp]	0.62

3.3.2 Surfactant Solution Properties

A total of five different fluid system were used in this work, with water being the fifth fluid and base case. The main differences among the fluids were their respective compositions and charges. The concentration of the surfactants is defined in the unit of gallon per thousand gallons (i.e., gpt), which means a gallon of pure surfactant per thousand gallons of solvent, in this case water. A solution with a concentration of 1gpt was prepared by mixing a gallon of surfactant in one thousand gallons of water. In a more research-friendly concentration approach, gpt can also be converted to vol%, where 1gpt is equal to 0.1vol%. **Table 3-3** contains the necessary data regarding the content and composition of each fluid system.

Table 3-3 Surfactant system compositions and properties

Surfactant	*Composition*	*Weight [%]*	*Density [lb/gal]*	*Color Pellet*
Nonionic 1	Isopropyl Alcohol	15 to 40	7.6	
	Citrus Terpenes	10 to 30		
	Water	10 to 30		
	Ethoxylated Castor Oil	15 to 40		
	Polyoxymethylene	5 to 10		
Nonionic 2	Isopropyl Alcohol	10 to 30	8	
	Citrus Terpenes	3 to 7		
Nonionic 3	Isopropyl Alcohol	10 to 30	7.7	
	Citrus Terpenes	10 to 30		
Cationic	Isopropyl Alcohol	10 to 30	7.9	
	Citrus Terpenes	5 to 10		
	Ethoxylated Alcohol	3 to 10		
	Quaternary Ammonia Compound	5 to 10		

3.4 Interfacial Tension

In this work, IFT measurements were performed statically. The statical methods employed (e.g., pendant drop, sessile drop) involve the droplet being in an equilibrium shape in a forcefield that tends to deform the droplet, such as gravity or centripetal forces, and the force of interfacial tension, which tends to minimize the surface area of the droplet. The difficulty involved with such methods revolves around acquiring accurate density measurements for the liquid of interest (here, oil) and its surrounding phase (here, water or the surfactant solution). Such methods are also time-consuming, due to the time needed to reach equilibrium. Highly viscous liquids with additives and gelling agents like polymers are the most affected by statical IFT measurements, as they are more prone to the thermal degradation that occurs during the wait time. However, in this case, the oil was light and the additives used were not more viscous than water. For these reasons, the

pendant drop method was elected to measure the IFT values of the aqueous systems in relation to oil.

The pendant drop method is the most widely used in the petroleum industry for IFT measurements, due to its simplicity, accuracy, and reliability. The mechanism functions simply by suspending a droplet of heavier liquid in a bulk of lighter liquid phase. The droplet is kept suspended from the tip of the syringe once a balance between gravity and interfacial tension is reached, as shown in **Figure 3-3**.

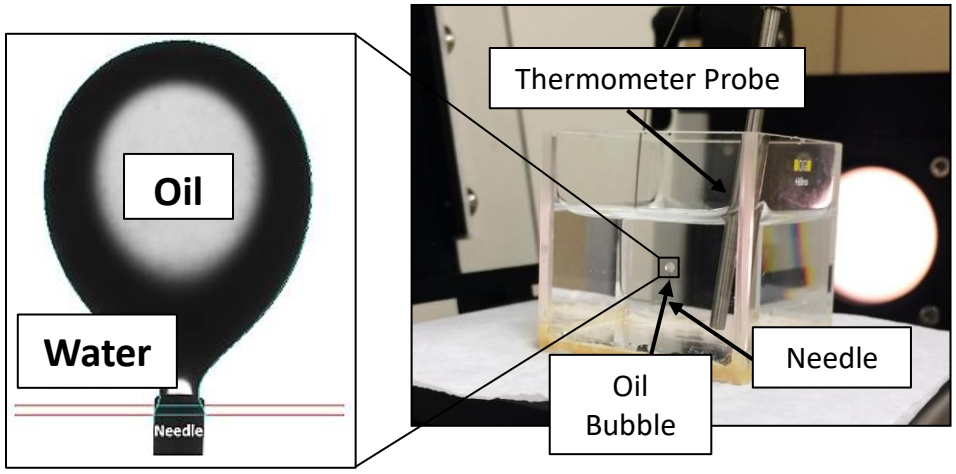

Figure 3-3 Inverse pendant drop method schematic.

A J-shaped needle was used to dispense the oleic phase upward in the aqueous phase. The J-shaped needle was important because the oil was lighter than the aqueous phase, meaning that dispensing downward was not possible. The IFT measurements were performed using Dataphysics OCA 15 Pro, as shown in **Figure 3-4**. During the experiment, the drop was assumed to be symmetrical around a central vertical axis; a view of the drop was accessible from all angles. Also, the drop was in a completely static and

motionless condition. The dimensional characteristics of the droplet were only governed by gravity and IFT forces.

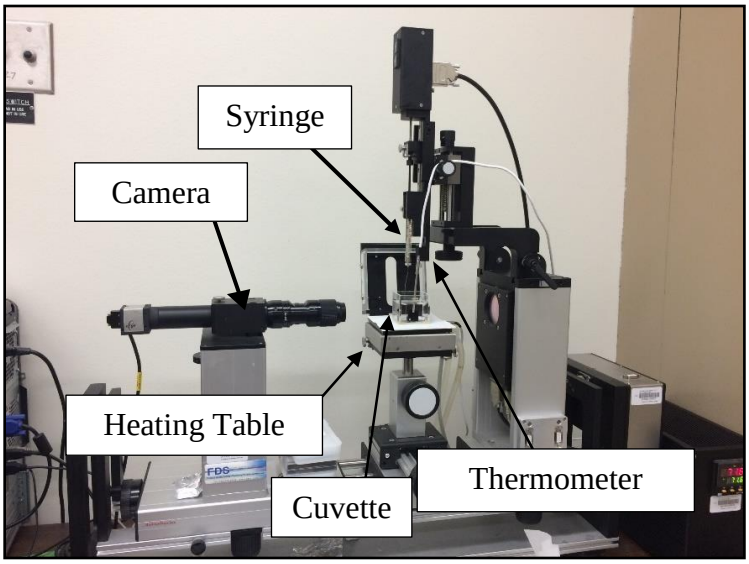

Figure 3-4 Dataphysics OCA 15 Pro used for IFT and contact angle measurements.

The IFT measurements were performed at $155^{o}F$, the Wolfcamp B reservior temperature. This was accomplished by heating the aqueous phase in the cuvette on top of the heating table. A temperature probe was used to monitor the temperature of the system during the heating process. This ensured that the desired temperature was reached. After reaching the desired temperature, a motorized syringe with a J-shaped needle containing oil was used to slowly dispense an oil bubble into the aqueous phase until the bubble reached equilbruim and detached from the tip of the needle. The motorized needle was allowed for even increments of oil as low as 0.001µL to be dispenesed, eliminating the negative impact of fluid inertia during dispensing. A built-in high-speed camera system was used to capture images of the bubble, while software calculated the IFT based on the given density of the oil at the reservior temperature.

In this work, the IFT for the Wolfcamp oil with water was found to be approximately 22 mN/m. All surfactant solutions reduced the interfacial tension of the oil and water. The IFT for the surfactant solutions was measured at two different surfactant concentrations: 1gpt and 2gpt. The addition of the cationic surfactant reduced the IFT the most, to 4.55 and 3.63 mN/m at 1gpt and 2gpt, respectively. The addition of nonionic surfactants appeared to influence the IFT in a similar fashion; the addition of 1gpt of Nonionic 1 reduced the IFT from 22 to 5.56 mN/m, while the same concentration of Nonionic 2 and Nonionic 3 reduced the IFT to 5.69 and 6.12 mN/m, respectively, as shown in **Figure 3-5**.

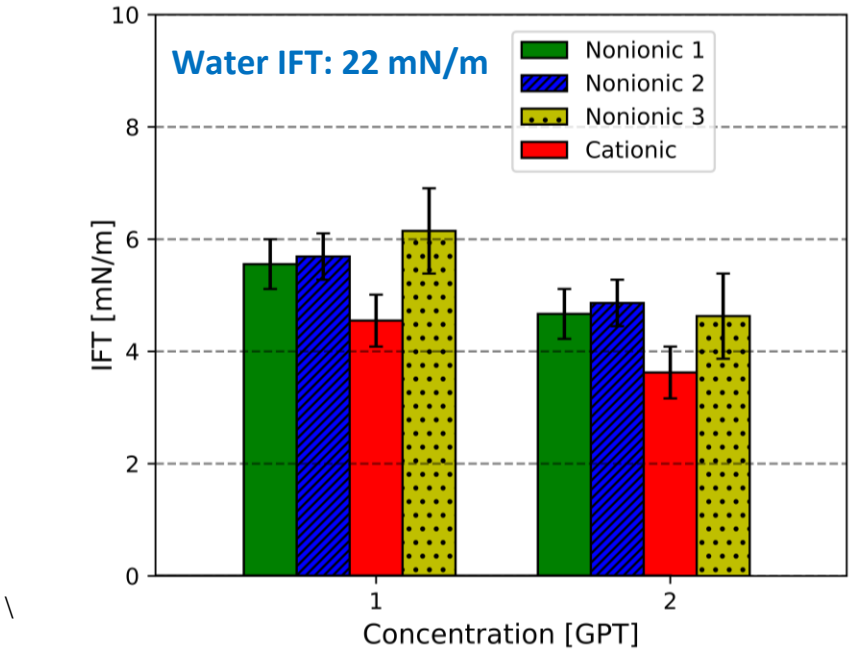

Figure 3-5 Interfacial tension of the tested aqueous solutions at different concentrations.

IFT is an unorthodox parameter, as high IFTs can increase capillary pressure, resulting in greater imbibition. Low IFTs, however, assist in getting oil out of small pores. Sometimes in imbibition experiments where core samples are initially saturated with oil, the ultimate recovery increases with a reduction in IFT, even with the consequent

reduction in capillary pressure. Such a phenomenon can be attributed to the transition from capillary-dominated flow to gravity-dominated flow as the IFT is reduced. However, relatively higher IFT values are desirable in imbibition experiments, because higher IFTs correlate to larger capillary driving force capacity. Extremely high IFTs, however, are not desirable, because they may lead to blocking as represented by lower relative permeability curves (compared to oil and water systems with lower IFTs).

3.5 Contact Angle

In the present research, contact angles were measured utilizing Dataphysics OCA 15 Pro in captive bubble mode. The advantage of the captive bubble method is that it requires a solid sample to be submerged in liquid, which sequentially ensures that the substrate is in contact with an aqueous solution. Using this method also minimizes the risk of contamination of the solid-aqueous solution interface that may form as a result of the oil drops. Additionally, it provides simpler and more explicit ways of investigating the dependence of the contact angle on temperature, since it is more perspicuous to monitor the liquid's temperature via the captive bubble method than through sessile drop. However, the captive bubble technique has some disadvantages. It requires far more liquid compared to other methods (such as sessile drop). Also, swelling of the solid surface upon immersion and continuous dissolution of the surface film by the liquid can give rise to different degrees of intricacy in the captive bubble method.

In this work, however, measurements were completed as quickly as possible to eliminate the effect of dissolution of the surface film by the aqueous solution. Aged solid rock chips (1cm x 1cm) from the subject formations were separately immersed in heated

aqueous solutions on top of a stage. The oil was dispensed to be in contact with the bottom surface of the rock chips. In order for the experiment to be successful, it was important that the needle be kept in the bubble throughout the measurement time. This is because the balance of the advancing angle can be deeply affected by the removal of the disturbance. This also provides stability, so that the bubble does not drift over the solid surface when the plane is not perfectly horizontal, which is often the case with unpolished rock surfaces. A built-in high-speed camera system was used to capture the images of the oil bubble when in contact with the rock surface, while the captive bubble software calculated the angle formed between the oil bubble and the surface. The contact angles calculated from the Dataphysics OCA 15 Pro captive bubble software were the angles of the surface and bubble with respect to the oil phase. However, as explained in **Chapter 2**, the Young convention used for contact angle data is in respect to the aqueous phase, and not the oil phase. Therefore, a conversion was applied to the contact angle data obtained from the software, as shown in **Eq. (3-1)**.

$$\theta_y = 180 - \theta_m \tag{3-1}$$

where θ_m is the measurmed contact angle from the software and θ_y is the Young contact angle with respect to the aqueous phase, in degrees.

The contact angles for each fluid system at two different concentrations were measured at the reservoir temperature. To ensure consistency of the contact angle measurements, each was performed by dispensing around 0.1μL of oil. Also, multiple trials were conducted, and the results were averaged to preserve repeatability and minimize measurement error. In this work, it was found that the natural wettability of the

Wolfcamp B2 formation was in both the intermediate and oil-wet regions, at 99° and 122° for the quartz-rich and carbonate-rich samples, respectively. All fluids that had surfactants added to them managed to alter the wettability from the natural condition to either the intermediate or water-wet regions, depending on the environment and concentration (see **Figure 3-6**).

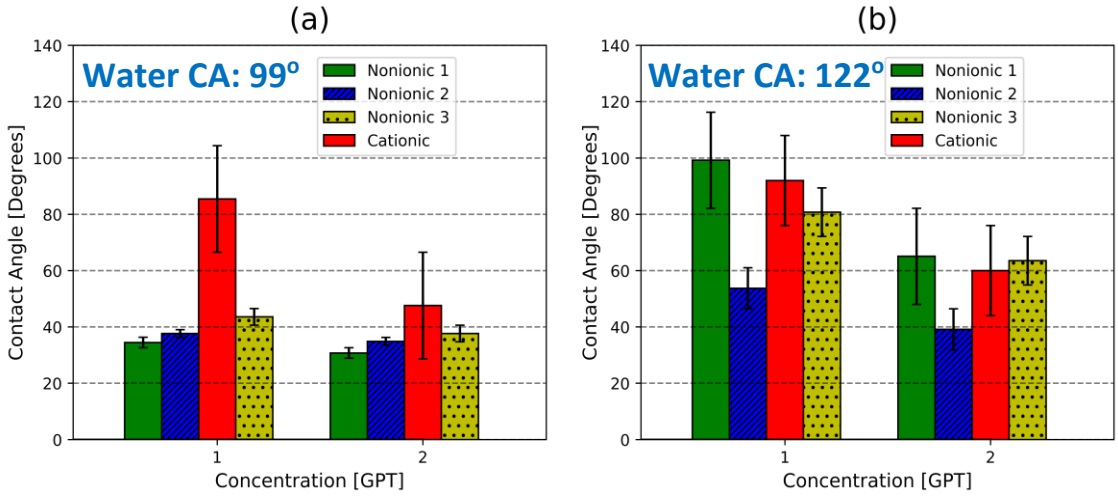

Figure 3-6 Contact angles for the four tested fluid systems at 1gpt and 2 gpt. Figure (a) represents the quartz-rich environment, while (b) represents the carbonate-rich environment.

General wettability in the quartz-rich environment was found to be approaching intermediate to water-wet for all tested systems, including water. Nonionic 1 altered the wettability the most in the clastic environment; the contact angle was reduced from 99° to 34°. However, it is clear that the addition of any of the tested nonionic surfactants significantly altered the wettability, as compared to the cationic surfactant in the quartz-rich environment. Increasing the concentration of the nonionic surfactants from 1gpt to 2gpt did not result in a significant wettability alteration, as compared to the cationic surfactant where the contact angle changed drastically from 88° to 42°. This behavior can

be attributed to the stability of the surfactant, which is addressed separately in the ζ potential section.

The carbonate-rich environment was more challenging. All surfactants altered the wettability, at least to some extent. Nonionic 1 altered the wettability the least; the contact angle was reduced from 122^{o} to 92^{o}. It is still feasible to add surfactants at different concentrations, however, since the addition of any of the tested nonionic surfactants altered the wettability compared to the base case, which was extremely oil-wet. The ability to alter wettability to the water-wet region is crucial, as it shifts the capillary forces to be more favorable during the imbibition process. Oil-wet wettability causes a negative capillary pressure, as can be deduced from the Young-Laplace equation which, in turn, reduces the imbibition and encumbers the flow of oil by trapping the oil in the pore spaces. Conversely, water-wet wettability results in a positive capillary pressure, enhancing the imbibition process and boosting production of oil out of the pore spaces. For illustration, compilations of different contact angles for the tested fluid systems in different environments are shown in **Figure 3-7** and **Figure 3-8**. The wettability alteration performance of a surfactant is easily observed by looking at the oil bubbles. Water-wet bubbles are more spherical than oil-wet oil bubbles, which tend to stick more to the surface.

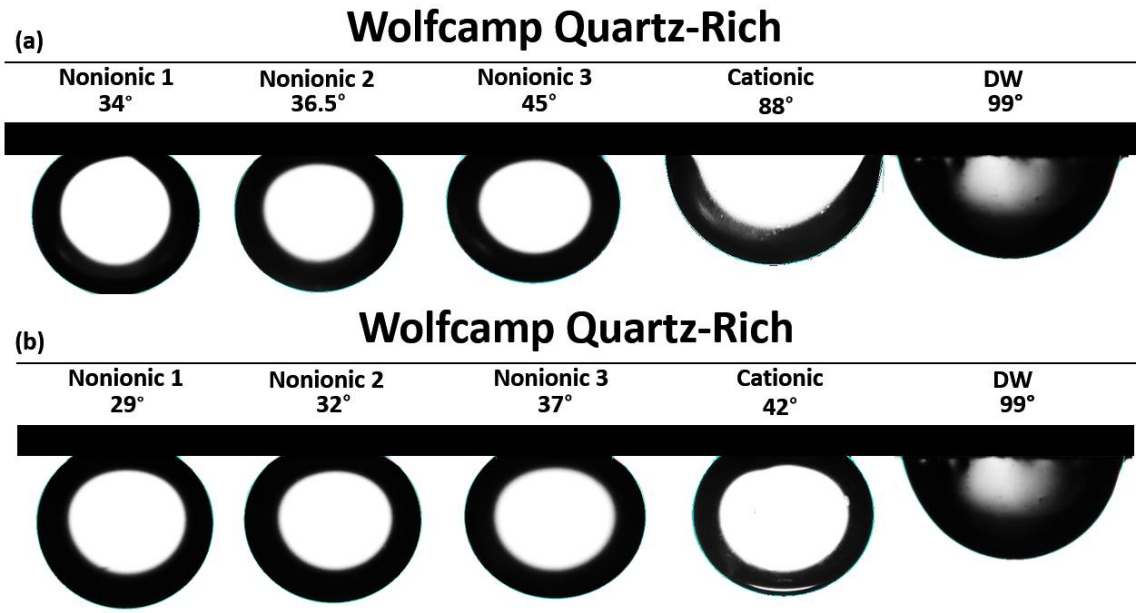

Figure 3-7 Contact angle illustration of the five tested fluid systems in the quartz-rich environment: (a) 1gpt and (b) 2gpt.

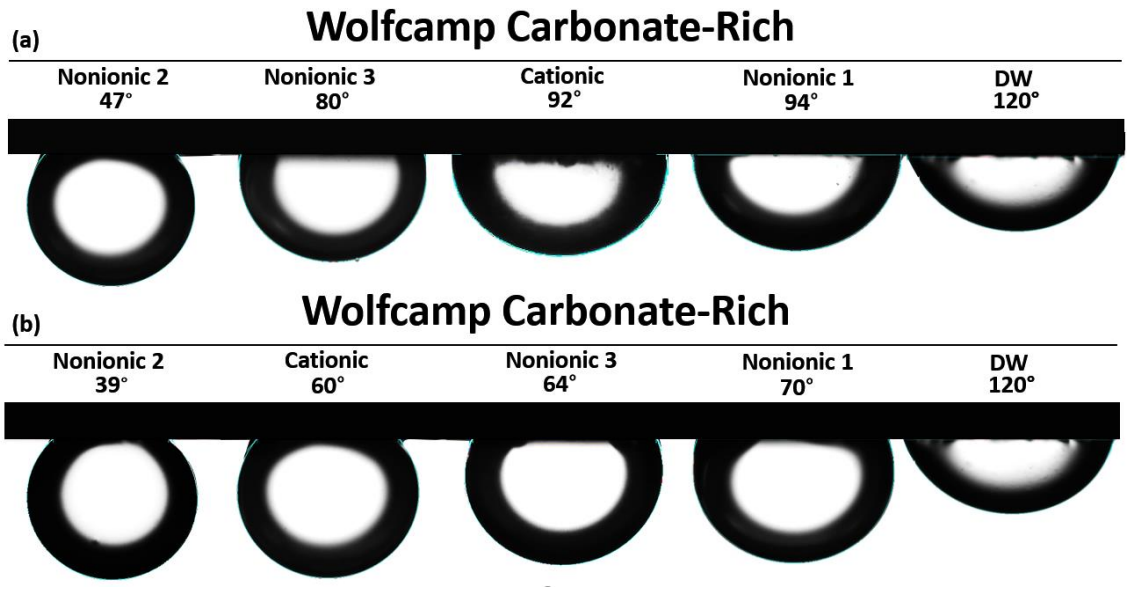

Figure 3-8 Contact angle illustration of the five tested fluid systems in the carbonate-rich environment: (a) 1gpt and (b) 2gpt.

3.6 Zeta Potential

ZetaPALS from Brookhaven Instruments, as shown in **Figure 3-9**, was used to measure the ζ potential of the rock/surfactant interfaces. The ζ potential for the four surfactants at different concentrations (i.e., 0.52gpt, 1gpt, and 2gpt) was measured and evaluated. The results are presented in this section, which is divided into three subdivisions: the ζ potentials of the rock/surfactant interfaces, ζ potential of oil/surfactant interfaces, and ζ potential vs. CA.

Figure 3-9 NanoBrook ZetaPALS for ζ potential measurement.

3.6.1 Zeta Potential of Rock/Surfactant Interfaces

The ζ potential of the rock/surfactant interface was measured by separately mixing 0.1 g of solid particles from carbonate- and quartz-rich Wolfcamp B2 formations in 5 mL of pre-prepared surfactant solution at the desired concentrations. Next, the mixture was sonicated in a bath sonicator for 1 minute to ensure proper mixing. Sonicated samples were left for 4 to 8 hours to reach equilibrium before measurements were taken. The time-based variation depiction of the ζ potential of the quartz- and carbonate-surfactant systems

is shown in **Figure 3-10**. The results of the time-based variation analysis indicate that the ζ potential was relatively stable after 4 to 8 hours in the cases of the evaluated mixtures.

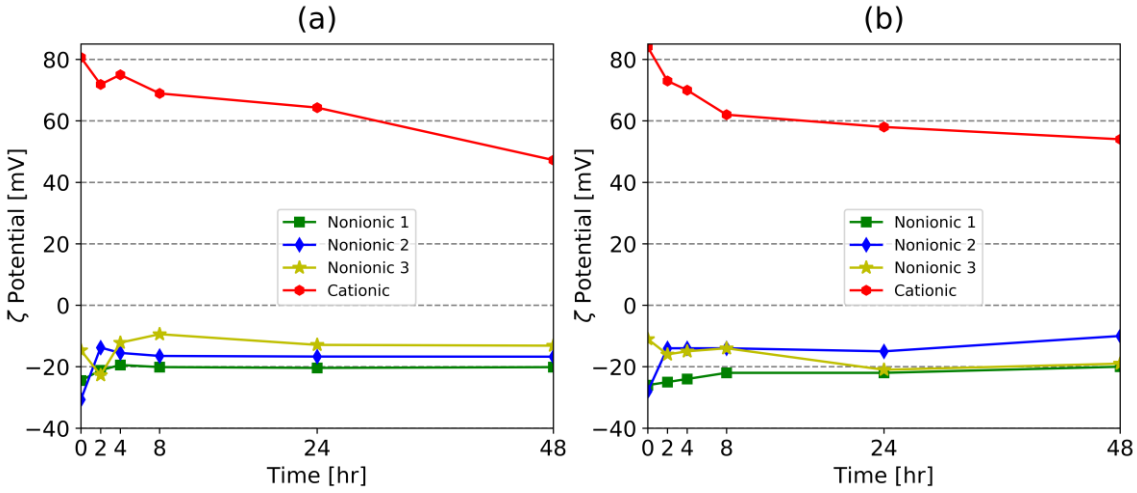

Figure 3-10 Effects of time lapse on the ζ potentials of rock/surfactant interfaces measured at 2gpt: (a) quartz-rich and (b) carbonate-rich.

The trend in ζ potential for the rock/surfactant interfaces with various concentrations appears to be similar in the carbonate and quartz cases. The ζ potential of the carbonate-rich distilled water system was found to be around −27.3 mV, whereas the ζ potential of the quartz-rich distilled water system was found to be around –29.9 mV, slightly more negative compared to the former. This was due to the low solubility of the calcium carbonate. Aa shown in **Figure 3-11**, all surfactant solutions, excluding Nonionic 3, followed a predictable trend, where the ζ potential increased with the concentration. This trend was clear in the cationic case, but not as clear in Nonionic 1 or Nonionic 2.

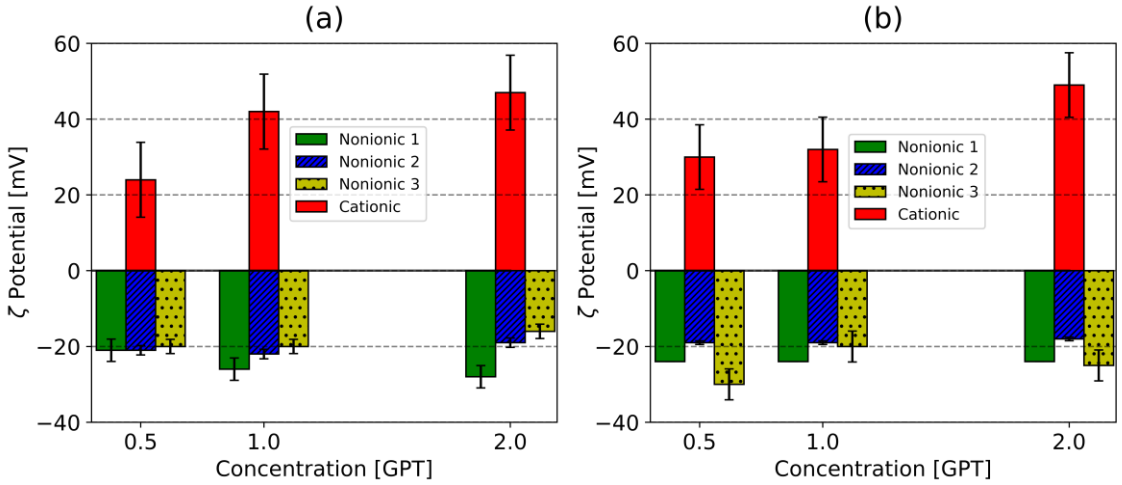

Figure 3-11 Effects of surfactant concentration on the ζ potential of the rock-surfactant interface: (a) quartz-rich and (b) carbonate-rich.

It appears that Nonionic 2 reached its maximum stability at 0.5gpt and 1.0gpt when mixed with Wolfcamp B2 carbonate- and quartz-rich rock particles, respectively. The behavior of the nonionic surfactant with a solvent (i.e., Nonionic 3) was different from those of the other surfactants. The measured ζ potential fluctuated due to the effect of the solvent on the rock particles, triggering the formation of an unstable double layer that changed with time (see **Figure 3-11**).

3.6.2 Zeta Potential of Oil/Surfactant Interfaces

ZetaPALS was also used to measure the ζ potential of the oil-surfactant interfaces. The ζ potential of the oil-surfactant interface was measured by mixing a small drop of Wolfcamp B2 oil with a surfactant solution. The ζ potential of the oil droplets in DW was found to be around −45 mV, more negatively charged than that of the carbonate- and quartz-rich rock particles in DW. The highly negative ζ potentials for oil dispersed in DW solutions was mainly associated with the buildup of hydroxyl ions at the oil/brine interfaces. It is worth noting that the average ζ potential of xylene dispersed in a low salt

content solution was found to be around −80 mV, while the ζ potential values for dodecane and hexadecane dispersed in the same low salinity solution were found to be around −60 mV (Marinova et al. 1996).

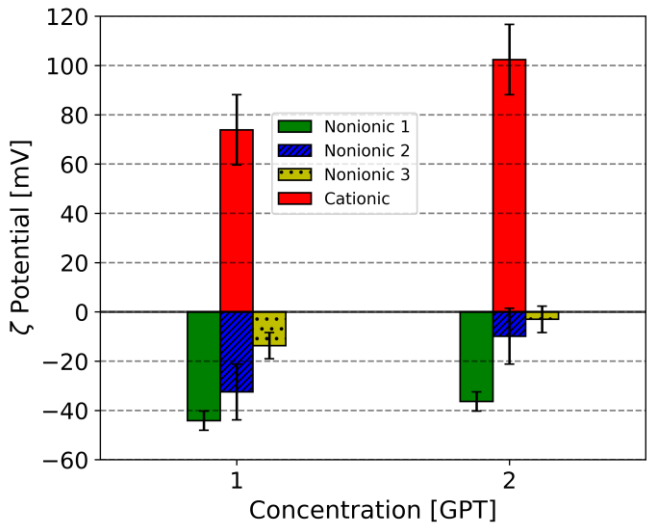

Figure 3-12 EffectS of surfactant concentration on the ζ potential of the oil-surfactant interface.

The ζ potential values of oil droplets in the tested cationic surfactant were found to be extremely positively charged, around +80 mV. Oil droplets are negatively charged under normal pH conditions, and the cations attached intensely to the oil droplets, causing the observed increase in double-layer electric potential. It appears that the hydrophilic heads of the cationic surfactant attached more to the aqueous solution, while the hydrophobic tails oriented towards the oil droplet's surface, rendering the surface more water-wet. The two nonionic surfactants exhibited similar behavior; the ζ potential decreased in magnitude, becoming less negative with as the concentration increased.

3.6.3 Zeta Potential vs. Contact Angle

In this section, ζ potential and CA are plotted against one another for further analysis and the identification of a possible direct relationship between the two. The

dataset available for this work was not sufficient to establish a satisfactory sample size. Increasing the sample size decreases the width of the confidence interval, which results in a reduction of the standard error for data analysis and statistical inference. Therefore, Park and Schechter's (2018) data were also used in conjunction with the data presented in this study. Figure 6 shows a composite scatter plot with the ζ potential plotted on the y-axis and CA plotted on the x-axis. Data analysis and statistical inference evaluations are included here via two histogram plots for each axis, respectively.

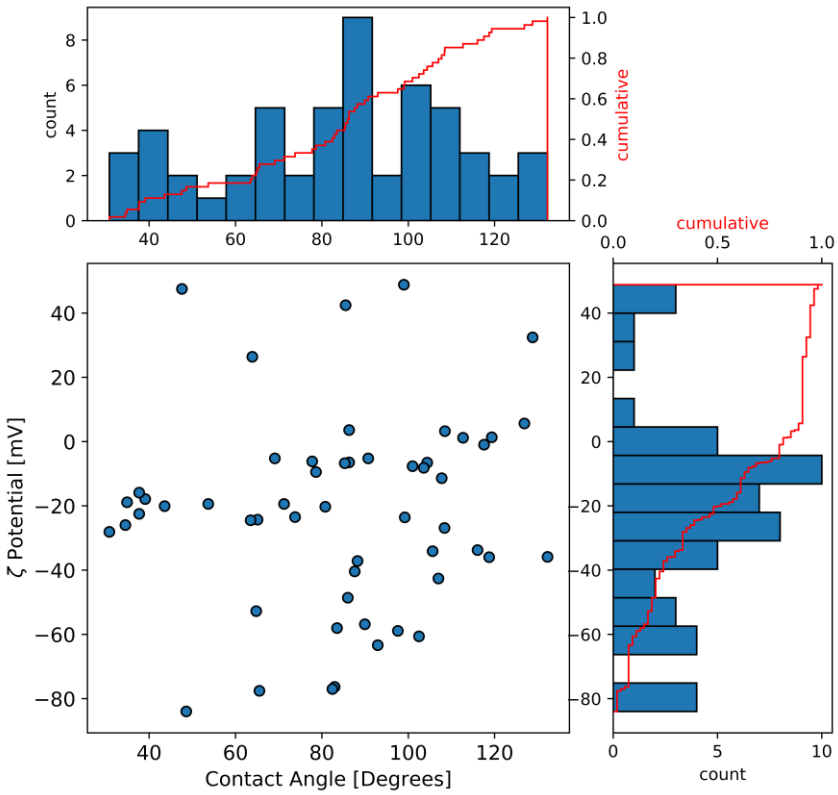

Figure 3-13 The ζ potential of the rock-surfactant interface vs. contact angle: (right) ζ potential count and density distribution, and (top) contact angle count and density distribution.

Figure 3-13 indicates that there was no apparent relationship between the two variables. This means that high absolute ζ potential values were just as likely to occur with extremely water-wet surfaces as they were with oil-wet surfaces. This lack of

predictability in determining the ζ potential from the given CA value and associated amorphous appearance of the scatter plot led to the conclusion that there was no direct relationship between the measured ζ potential of the rock-surfactant interface and CA.

3.7 Adsorption Isotherm

The surfactant adsorption isotherm was measured using a Hitachi U-4100 UV-Vis Spectrophotometer. This instrument has the ability to emit light with wavelengths ranging from 190nm to 3000nm, allowing for a robust wavelength analysis and calibration curve construction. **Figure 3-14** illustrates the configuration for liquid measurment.

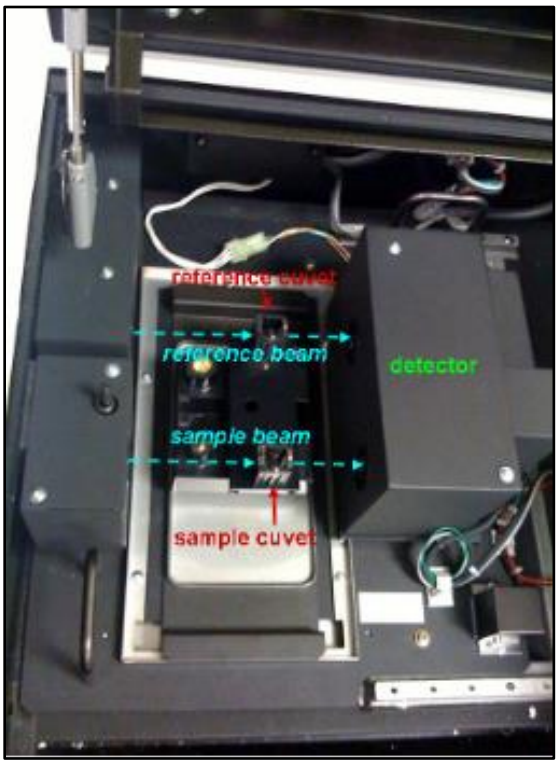

Figure 3-14 Hitachi U-4100 UV-Vis liquid adsorption configuration.

In this work, calibration curves were consutructed by comparing the light adsorption on a sample solution (i.e., surfactant) with the adsorption on a reference solution (i.e., distilled water). Each surfactant had a unique wavelength characteristic; thus, a

wavelength curve for each surfactant at different concetrations was contructed, ranging from 190nm to 300nm. The unique wavelength of each concetration for each surfactant was determined by analyzing changes in the wavelength curves, as shown in **Figure 3-15**.

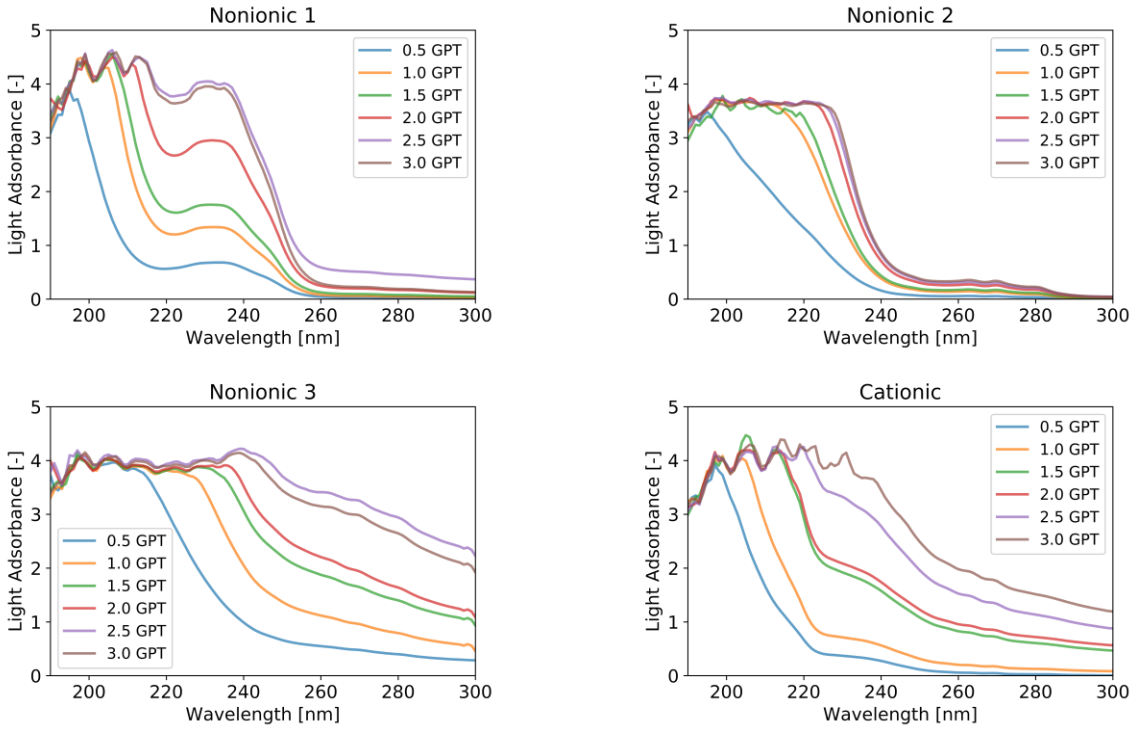

Figure 3-15 Wavelength curves for Nonionic 1, 2, and 3 and Cationic.

The initial adsorbance of light value was deterimend for each surfactant concetration by selecting the light absorbance value at the unique wavelength. The unique wavelength values for Nonionic 1, Nonionic 2, Nonionic 3, and Cationic were found to be 212nm, 227nm, 230nm, and 220nm, respectively.

Calibration curves were built by plotting the surfactant concentrations on the x-axis and light adsorbance at different concentrations on the y-axis, as shown in **Figure 3-16**.

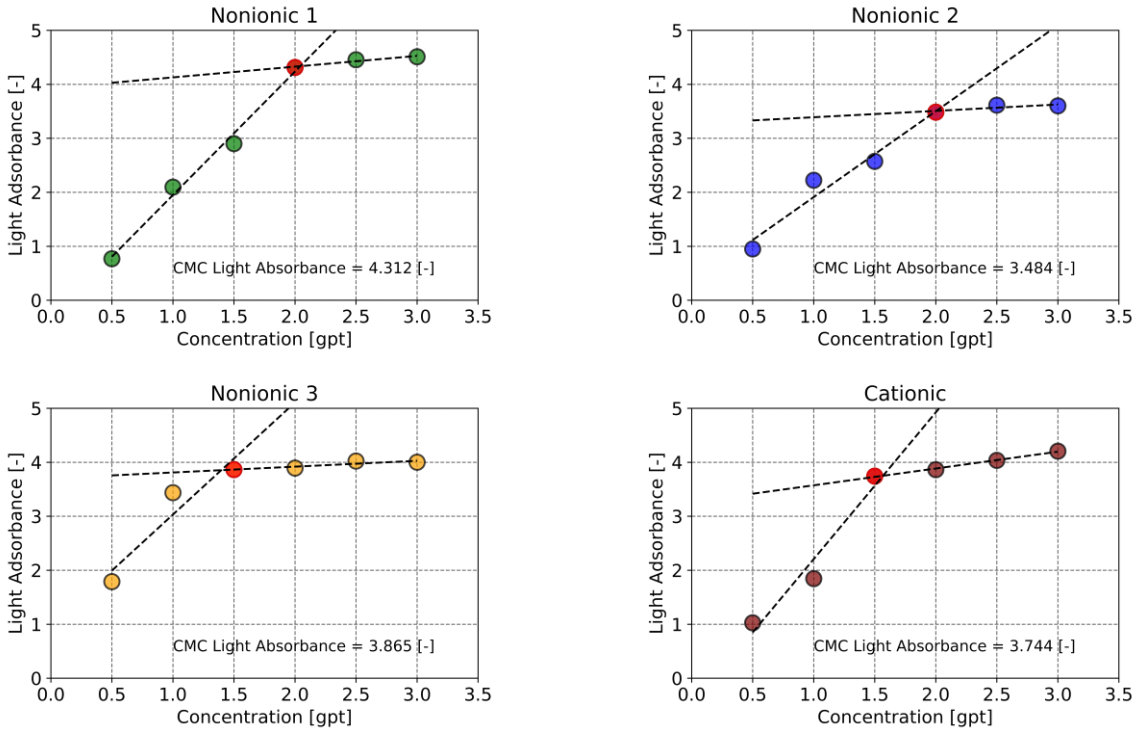

Figure 3-16 Light absorbance curves for Nonionic 1, 2, and 3, and Cationic.

The change in slope denotes the deflection point, indicating that the surfactant solution reached the critical micelle concentration (CMC). This phenomenon occurs when surfactant concentrations higher than the CMC no longer follow the Beer-Lambert law upon which the adsorption isotherm measurement is based. Using adsoprtion data above the CMC in simulations or any other adsorption-based study is not advisable.

The surfactant adsorption was measured after construction of the calibration curves. The rock chips were cleaned by soaking them in toluene for three days, followed by methanol for two days; then, the chips were vacuum-dried for two days. After the cleaning process, the chips were powedered and filtered, removing any particles larger than 300 microns. Adsorption was calculated using **Eq. (3-2):**

$$\theta_A = \frac{0.119 * (\phi i - \phi f) * V_{Surf} * \rho_{Surf}}{w_{rock}} \quad (3\text{-}2)$$

where θ_A is the adsorption in mg/gr-rock, ϕi is the initial surfactant concentration in gpt, ϕf is the final surfactant concentration in gpt, V_{Surf} is the volume of the surfactant in ml, ρ_{Surf} is the densitiy of the pure surfactant solution in lb/gal, and w_{rock} is the weight of the added powdered rocks in grams. **Figure 3-17** shows the adsorption isotherm; the surfactant concentration is on the x-axis and adsorption at different concentrations, calculated using **Eq. (3-2)** is on the y-axis.

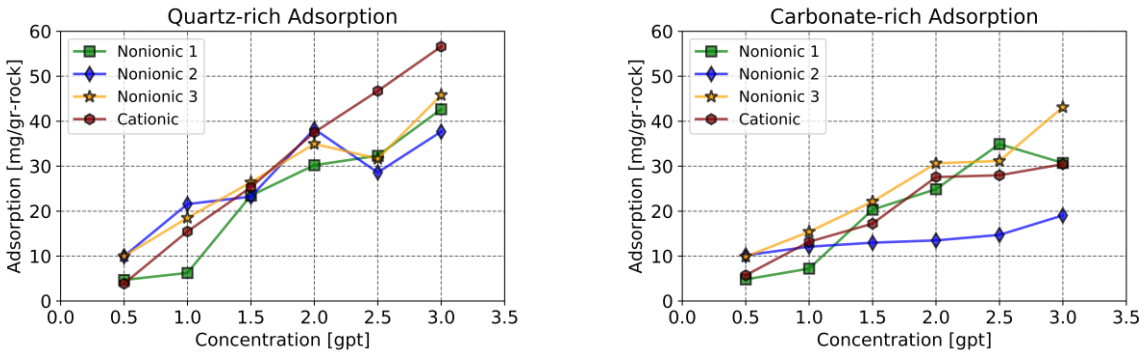

Figure 3-17 Adsorption isotherm for the four tested surfactant solutions in the Wolfcamp quartz- and carbonate-rich formation.

CHAPTER 4

SPONTANEOUS IMBIBITION AND FLUID DISPLACEMENT

Spontaneous imbibition is defined as the process during which a wetting phase imbibes a porous medium by surface energy through the action of capillary forces. Capillary pressure is related to contact angle and interfacial tension. It is the product of interfacial tension and curvature of the interface, which depends on surface forces and pore size distribution. Following this concept, the resulting displacement is spontaneous if the pore size distribution and curvature of the interface allow the interface to advance. Spontaneous imbibition plays a significant role in oil recovery and is employed in several applications such as waterflooding in heterogeneous reservoirs, alternating water, and gas injection and surfactant assistance in unconventional reservoirs. Surfactant-assisted spontaneous imbibition oil recovery is of particular importance in tight rocks, especially when such rocks have very low permeability. Currently, much of the existing oil reserves are located in moderate to low-quality rocks, which are typically denoted by a very low permeability and moderately low porosity. Most low-quality rocks exhibit productive initial oil production through hydraulic fracturing. Oil production from such low-quality rocks has placed the United States among the largest oil producers in the world, besides Saudi Arabia and Russia (Doman 2018). However, this may not continue due to the quick depletion caused by the limited amplification magnitude of the permeability.

Oil recovery in low permeability rocks via water injection is dependent on the spontaneous imbibition of water, which is extremely slow and generally does not yield acceptable results. The natural wettability of the subject formation examined in the present

research was found to be intermediate, as evaluated and presented in **Chapter 3**. Water is theoretically able to imbibe oil saturated cores and recover hydrocarbons by capillary forces in a countercurrent movement. Following this principle, water's ability to imbibe into low permeability core plugs can be employed to slightly improve oil recovery. The entire process, along with results produced by similar formations, were demonstrated by Alvarez and Schechter (2015, 2016) and Park and Schechter (2018). Their work underscores the importance of exploring other options to improve oil recovery from such resources and has led to the use of EOR applications in the subject formation.

4.1 Imbibition in the Matrix

There are three types of imbibition: pseudo-quasistatic, spontaneous, and dynamic forced (Morrow and Mason 2001). Pseudo-quasistatic imbibition is directly related to capillary forces. Capillary forces are measured with respect to the wetting phase fluid profile. Recovery is then measured by analyzing the increase in oil volume by a series of capillary pressure reductions. The dynamic exhibition of oil recovery, however, is measured by forcing brine, surfactants, or polymers through a porous medium under pressure. This type of imbibition analysis is usually carried out in high permeability rocks, as it can be performed in a laboratory through core flooding. Spontaneous imbibition is the most common approach to measuring imbibition-based oil recovery, due to its simplicity and versatility. This type of measurement is the main subject of the present work. In this process, the core plug is immersed in brine, surfactants, or a polymer solution, and the oil recovery is periodically recorded. Capillary pressure is not usually measured during spontaneous imbibition experiments as it often changes; this is in contrast

to capillary pressure in pseudo-quasistatic imbibition, where it is deliberately reduced. The change in saturation is monitored volumetrically, and the results are presented as recovery factors of the oil initially in place, with respect to time.

4.2 Computed Tomography Scanning

Computed Tomography (CT) scans are instrumental in monitoring the movement of fluid in and out of core plugs during spontaneous imbibition experiments. According to Hove, Ringen, and Read (1987), there are multiple methods for monitoring fluid movement during a core displacement test. In the present work, CT imaging was used to observe fluid movement into the cores with respect to time during the spontaneous imbibition experiments. Modified Amott cells were placed between the X-ray source and stationary array detectors. Then, electricity was pulsed into the X-ray tube, creating a ray that passed through the modified Amott cells and was received by the detectors. After the X-ray source completed a pass (denoted by 360 cycles), mathematical processing of the different X-ray values was performed by a computer. An open source software package called ImageJ was used to generate color-coded slices, based on changes in density.

CT numbers are proportional to fluid density and often detected using a dopant agent such as potassium iodide (KI). CT numbers range from -1,000 for air to +3,000 for extremely dense materials; pure water without a doping agent has a 0 CT value. Due to this drastic change in CT number, Garg et al. (1996) presented a technique for constructing a distribution of residual oil during experimental core flooding. The proposed methodology commences with subtracting raw images, normally post-saturation and post-flooding. The saturations are then computed from the CT numbers, as shown in **Eq. (4-1)**:

$$\mathrm{So}_t = \frac{CT_{t-}CT_{Dry}}{CT_{postsaturation-}CT_{Dry}} \quad (4\text{-}1)$$

where $CT_{postsaturation}$ is the CT number after the core is fully saturated with oil, which is often denoted by $CT_{initial}$; CT_{Dry} is the CT number after the core is fully cleaned and dried in an oven. The subscript t in CT_t denotes the time at which the core plug is scanned. Porosity maps for each slice can be obtained following the same principle, as shown in **Eq. (4-2)**:

$$\varphi = \frac{CT_{postsaturation-}CT_{Dry}}{CT_{oil-}CT_{Air}} \quad (4\text{-}2)$$

where $CT_{postsaturation}$ is the CT number after the core is fully saturated with oil, CT_{Dry} is the CT number after the core is fully cleaned and dried in an oven, and $CT_{oil-}CT_{Air}$ denotes the difference between the pure CT numbers of oil and air. Alvarez et al. (2014) proposed a simpler method for monitoring fluid distribution through a term called "penetration magnitude." This term can be calculated by **Eq. (4-3)**.

$$\text{Penetration Magnitude (PM)} = CT_{t-}CT_{Base} \quad (4\text{-}3)$$

The base CT number is the lowest average CT number for the core sample. It is often equal to CT_{Dry}. $The\ CT_t$ value is the CT number at the time of the scan, which is consistent across this work.

4.3 Discussion

Surfactant-assisted spontaneous imbibition (SASI) experiments were conducted after evaluating the ZP, CA, and IFT. In cases of tight rocks, the porosities of the cores are usually obtained through nitrogen or mercury injection. In this work, however, an average porosity value for each core was qualitatively obtained using NMR, due to its

nonintrusive nature. Those values were then compared to values estimated from averaged CT numbers. Modified Amott cells were employed to hold the cores while immersed in aqueous solutions. The volume of the produced oil was measured through a graduated tube at the top of the cell, as shown in **Figure 4-1.**

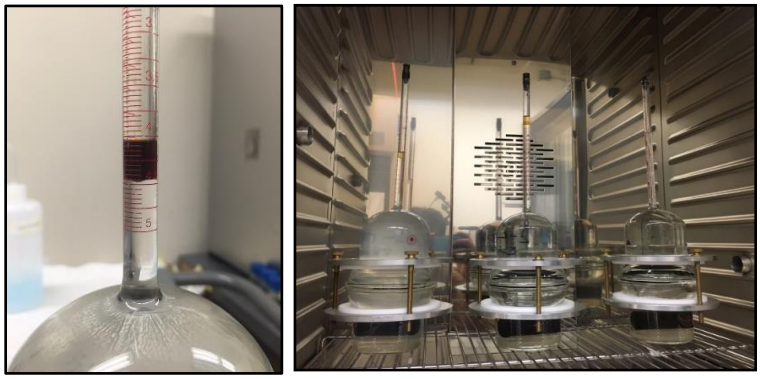

Figure 4-1 Schematic of a modified Amott cell depicting the graduated tube (left) and Amott cells inside an oven (right).

The Amott cells were then placed in an oven at reservoir temperature, 155 °F in the case of the subject reservoir (i.e., Wolfcamp). Volumetric results were obtained using **Eqs. (4-4)** and **(4-5)**.

$$V_{core} = \frac{\pi}{4} * D^2 * L \tag{4-4}$$

$$HCPV = Volume * \phi * (1 - S_w) \tag{4-5}$$

where V_{core} is the total volume of the core, D is the diameter, L is the length, $HCPV$ is the hydrocarbon pore volume, ϕ is the porosity, and S_w is the water saturation. In the present case, the water saturation was 0 because the cores were fully saturated with oil. The recovery factor (RF) was then calculated using **Eq. (4-6)**:

$$Recovery\ Factor\ (\%) = \frac{V_{oil,\ produced}}{HCPV} * 100 \tag{4-6}$$

It is also beneficial to monitor fluid movement in the cores; thus, the Amott cells were scanned periodically using a Toshiba Aquilion TSX-101A Medical CT, as shown in **Figure 4-2**. The aqueous solutions were doped with 4 wt% KI to enhance the contrast for improved visualization.

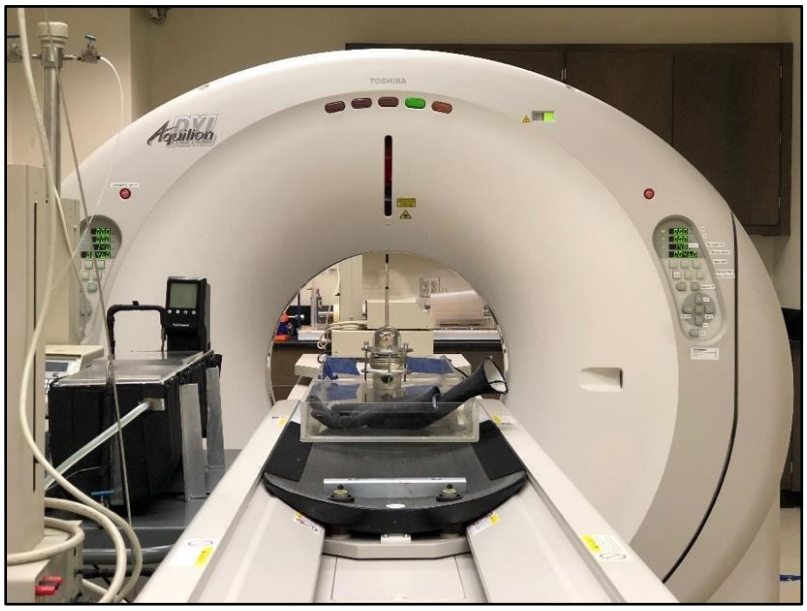

Figure 4-2 Toshiba Aquilion TSX-101A CT scanner.

The initial penetration percentage was calculated by modifying **Eq. (4-3)** into **Eq. (4-7):**

$$Initial\ penetration\ (\%) = \frac{CT_{0-}CT_{base}}{CT_{final-}CT_{base}} * 100 \qquad (4\text{-}7)$$

4.4 Results

Based on the ZP, CA, and IFT results, 1gpt was selected to be the optimum concentration for the surfactant solutions, due to its financial feasibility and affinity for close wettability alteration of higher concentration solutions. An SI for water was also performed as a base case to compare with the surfactant solutions. Five aqueous solutions were used for SASI on 10 Wolfcamp quartz- and carbonate-rich samples, divided evenly and denoted by Q and C, respectively, as shown in **Table 4-1**.

Table 4-1 Data on Core Samples and Fluids used in SASI Analysis

Sample	Diameter, in	Length, in	Bulk Volume, cc	SI Aqueous Solution
C1	0.9704	2.6784	31.4763	DW + 1gpt Nonionic 1 + 4 wt% KI
C2	0.9704	2.7158	31.9162	DW + 4 wt% KI
C3	0.9732	2.6284	31.0641	DW + 1gpt Nonionic 2 + 4 wt% KI
C4	0.9696	2.643	31.0092	DW + 1gpt Cationic + 4 wt% KI
C5	0.9696	2.2608	26.5252	DW + 1gpt Nonionic 3 + 4 wt% KI
Q1	0.9724	2.5413	29.9899	Nonionic 1 + 4 wt% KI
Q2	0.9972	2.0748	25.7493	DW + 4 wt% KI
Q3	0.9965	2.0736	25.6941	Nonionic 2 + 4 wt% KI
Q4	0.9965	1.9579	24.2598	Cationic + 4 wt% KI
Q5	0.9952	2.1572	26.664	Nonionic 3 + 4 wt% KI

Scans were taken after the cores were thoroughly cleaned, both during the saturation process and periodically throughout the SASI experiment. The evaluation of the penetration magnitude is presented in this section to illustrate the fluid penetration into the core samples during oil displacement. This part of the study is divided into two key sections: (1) surfactant-assisted spontaneous imbibition oil recovery and (2) oil displacement monitoring via CT imaging.

4.4.1 Surfactant-Assisted Spontaneous Imbibition Oil Recovery

As the ultimate experiment in this work, spontaneous imbibition provided a tremendous amount of data for analysis. The most important data were the spontaneous imbibition recovery curves of the ten fluid systems tested in this study. The recovery curves were constructed in the form of recovery factors in order to accommodate the different sizes of core plugs used in the experiment. Recovery factors were calculated by dividing the volume of oil recovered (as measured from the built-in graduated cylinder in

the modified Amott cells) by the initial oil in place for each core plug. The initial oil in place was calculated by subtracting the weight of the cores' post-saturation from the weight of the cores prior to saturation, and dividing the weight difference by the oil density. This approach was used to eliminate the uncertainty associated with qualitative porosity and irreducible water saturation measurement. Rock dimension data, including weights, are listed in **Table 4-2**.

Table 4-2 Rock Dimension Data*

Data	C1	C2	C3	C4	C5	Q1	Q2	Q3	Q4	Q5
D [in]	0.97	0.97	0.97	0.97	0.97	0.97	1	1	1	1
L [in]	2.68	2.72	2.63	2.64	2.26	2.54	2.07	2.07	1.96	2.16
V_bulk [cc]	31.48	31.92	31.06	31.01	26.53	29.99	25.75	25.69	24.26	26.66
m_AC [g]	84.58	87.6	83.5	84.99	71.93	71.23	62.55	61.6	57.68	64.8
m_AR [g]	85.32	87.73	84.25	85.15	72.21	74.03	64.34	63.42	59.35	66.71
m_BSI [g]	85.3	87.7	84.24	85.12	72.2	74.03	64.31	63.4	59.34	66.69
m_ASI [g]	85.23	87.68	84.18	85.11	72.17	74.19	64.46	63.5	59.46	66.85
ρ_oil [g/cc]	0.85	0.85	0.85	0.85	0.85	0.85	0.85	0.85	0.85	0.85
OOIP [cc]	0.85	0.12	0.87	0.15	0.32	3.29	2.07	2.11	1.95	2.23

*m_AC is the weight after cleaning, m_AR is the weight after saturation, m_BSI is the weight before SI, and m_ASI is the weight after SI

Oil recovery from quartz-rich core samples ranged from 19.2% to 33.7%, as shown in **Figure 4-3**. It was found that oil production through imbibition was still present in the base case fluid system, where no surfactant was added to the aqueous phase. The addition of a surfactant was proven to be highly advantageous to oil production. The recovery factor increased from 18% in the base case, up to 35%. The production rate also increased as the time needed to reach half of each corresponding ultimate recovery was faster than the base case.

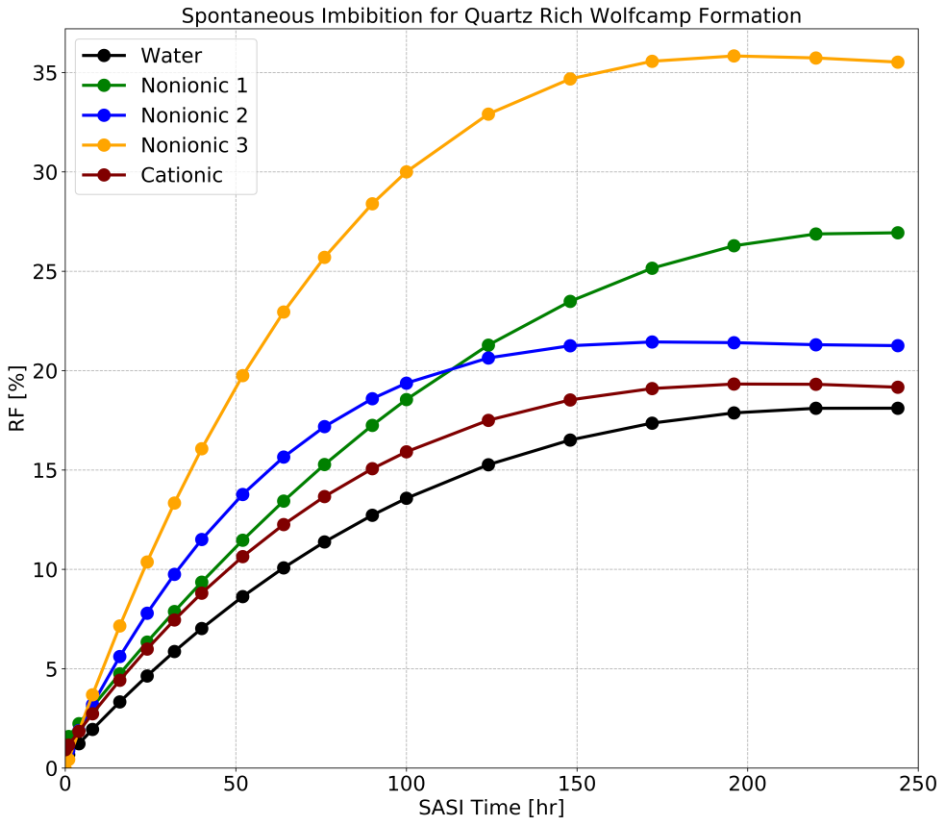

Figure 4-3 SASI results for Wolfcamp quartz-rich core samples.

Nonionic 1 and Nonionic 2 resulted in similar oil recoveries, 27.3% and 21.3%, respectively, with 9.2% and 3.2% additional oil recovery compared to the distilled water base case, respectively. The cationic surfactant performed similarly to the base case in the quartz-rich samples, where the measured recovery factor was 19.2% with 1.1% additional oil recovery (as compared to the distilled water base case). Nonionic 3 yielded the highest oil recovery in the quartz-rich samples at 35.9%, with 17.8%, 16.7%, 14.6%, and 8.6% additional oil recovery as compared to distilled water, Cationic, Nonionic 2, and Nonionic 1, respectively.

Comparing the imbibition results of each surfactant, the best recovery improvement in the quartz-rich environment was achieved from Nonionic 3, followed by

Nonionic 1, Nonionic 2, and Cationic. The contact angle and IFT data measured for Nonionic 3 are shown in **Figure 4-4**.

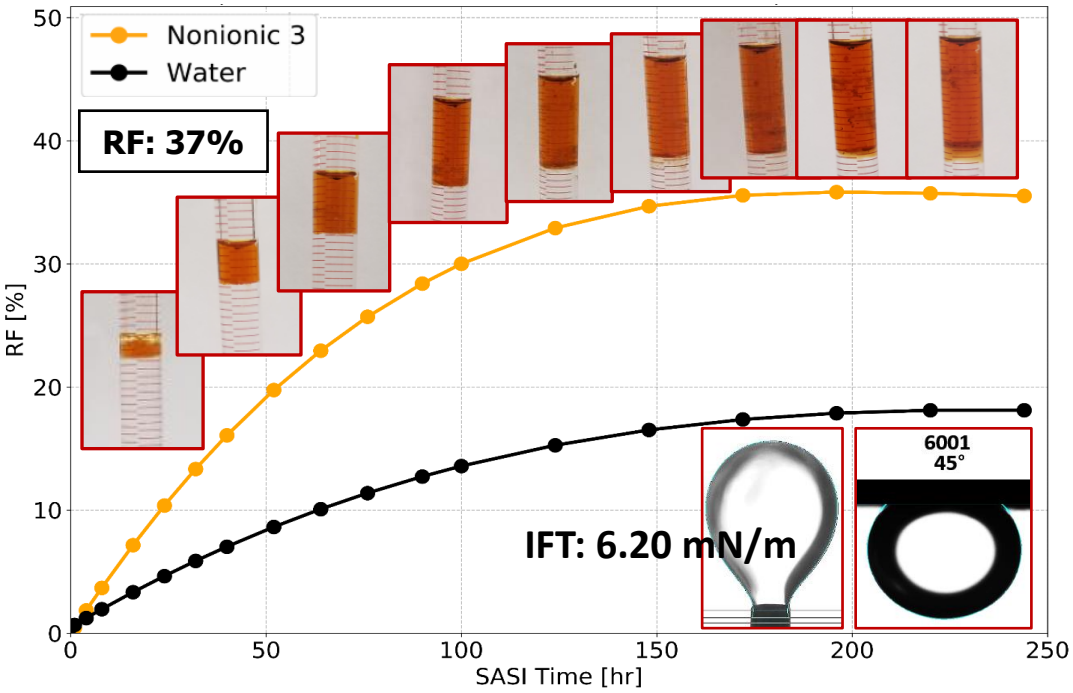

Figure 4-4 Oil recovery, IFT, and contact angle comparison for Nonionic 3.

The surfactant's level of effectiveness in enhancing oil production from SASI was expected. The magnitude of capillary pressure is a function of both the IFT and orientation of the force, which was determined by the wettability of the system. Nonionic 3 was observed to have the largest IFT of the tested surfactants; however, this was not by a significant margin. The contact angle and IFT data for the other surfactants, along with the recovery curves, are shown in **Figure 4-5** to **Figure** 4-7. Following the same conceptual analysis, Nonionic 1 should have shown a similar performance to that of Nonionic 2 in the quartz-rich environment, as the capillary force for Nonionic 1 as defined by the IFT and contact angle data was found to be extremely close to that of Nonionic 2. Different recoveries were observed with regards to the imbibition recovery curve; Nonionic 1

produced more oil than did Nonionic 2. This discrepancy can be attributed to the variance in petrophysical parameters between the two cores, which is discussed in Chapter 5 in terms of pore size distribution. The reasons for this outcome likely include a higher frequency of smaller pores, along with a high permeability path presented in terms of bedding planes or microfractures. The lowest recovery factor was observed in the distilled water case, followed by the cationic surfactant. This was expected due to their poor ability to alter wettability compared to the other tested aqueous solutions.

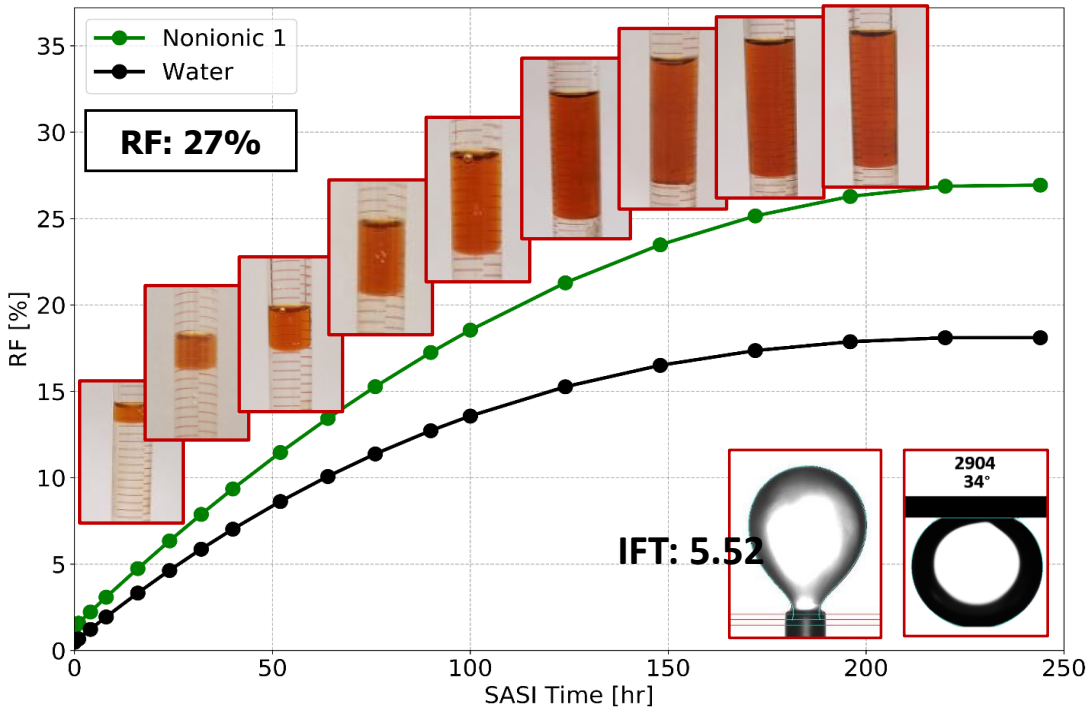

Figure 4-5 Oil recovery, IFT, and contact angle comparison for Nonionic 1.

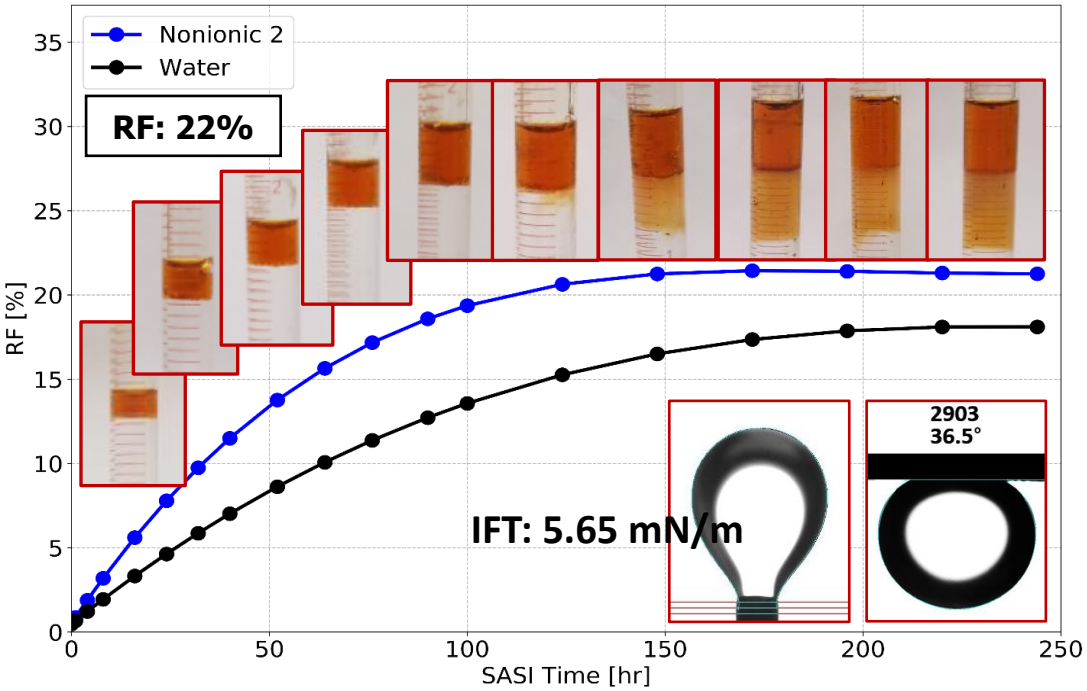

Figure 4-6 Oil recovery, IFT, and contact angle comparison for Nonionic 2.

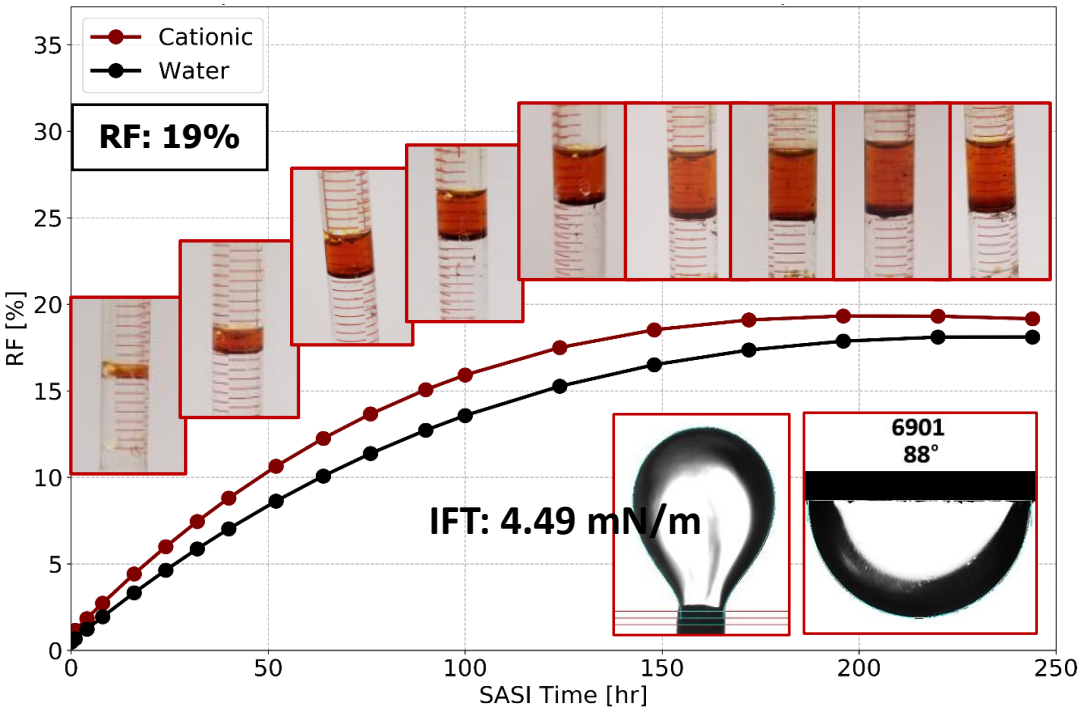

Figure 4-7 Oil recovery, IFT, and contact angle comparison for Cationic.

Oil recovery from the carbonate-rich core samples ranged from 14.8% to 49%, as shown in **Figure 4-8.** All nonionic surfactants performed similarly, 14.8%, 15.2%, and 17.2% for Nonionic 1, Nonionic 3, and Nonionic 2, respectively. Cationic outperformed all of the tested surfactant solution systems in the carbonate-rich environment, where the measured recovery factor was around 49%. When comparing the imbibition results for the surfactants in the carbonate-rich environment, the best recovery improvement was achieved with the cationic surfactant. The contact angle and IFT data measured for the cationic system are shown in **Figure 4-9**. The effective performance of the surfactant with regards to enhancing the oil production from SASI was as expected. The charge of the surfactant is likely the reason for its superb performance in this environment. In this case, the mechanism responsible for the additional observed oil production during SASI can be connected to the formation of ion pairs between the positive heads of the surfactant molecules and acidic hydrocarbon components in the oil that was adsorbed on the surface of the carbonate-rich rocks. As explained by Austad et al. (1998), as opposed to cationic surfactants, nonionic surfactants form a monolayer on the surface of carbonate-rich rocks through the interaction of their hydrophobic tails with crude oil that is adsorbed on the rock surface.

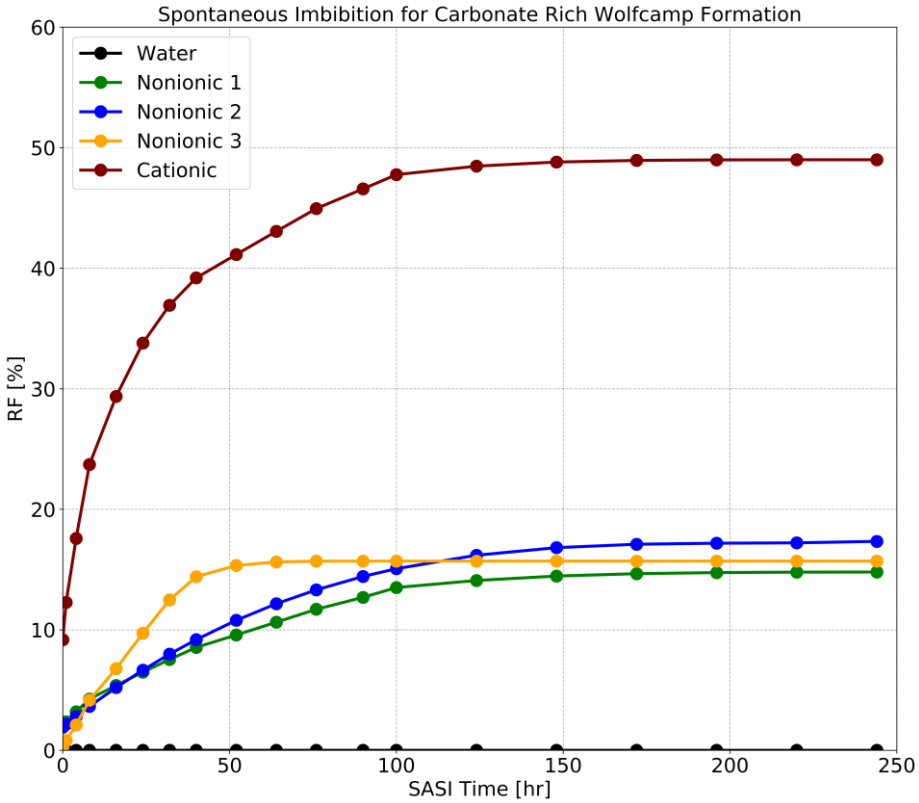

Figure 4-8 SASI results for Wolfcamp carbonate-rich core samples.

The monolayer formed on the surface of the carbonate-rich rocks and hydrophilic heads covering an oil-wet rock surface can possibly shift the wettability of the rock. As the wettability alteration mechanism is different between cationic and nonionic surfactants and the monolayer from nonionic surfactants is weaker than the ion pairs formed by cationic surfactants, this could explain the reason behind the unexpected performance of Cationic in the carbonate-rich environment. The contact angle and IFT data for the nonionic surfactants, along with the recovery curves, are shown in **Figure 4-11** to **Figure 4-12.**

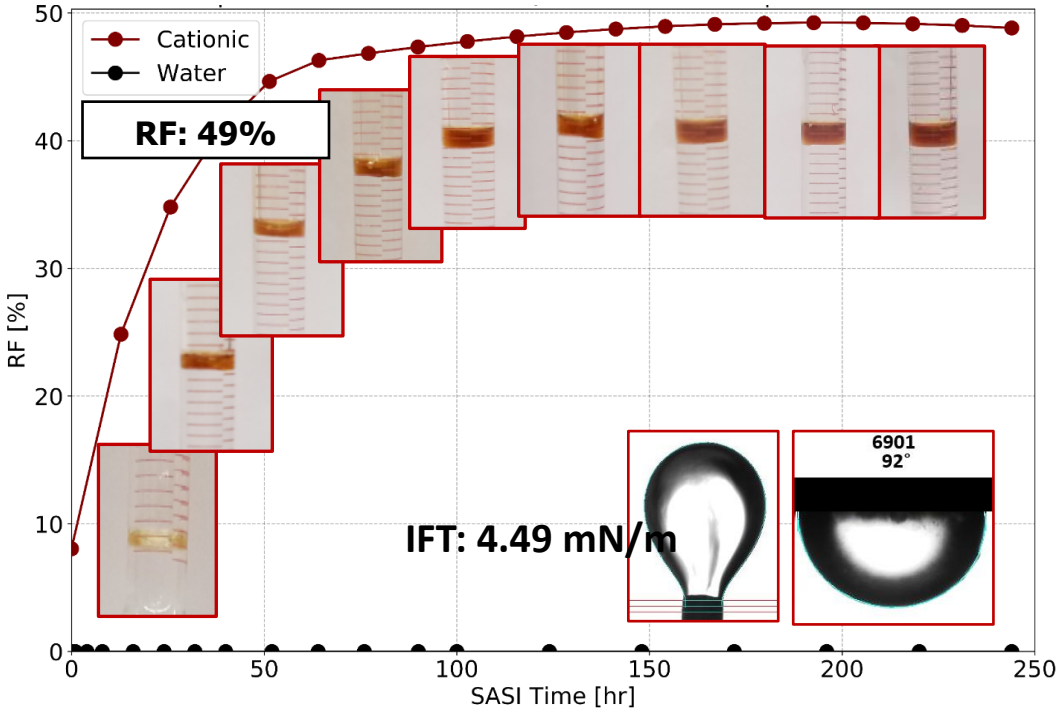

Figure 4-9 Oil recovery, IFT, and contact angle comparison for Cationic in the carbonate-rich environment.

As all nonionic surfactants have the same wettability alteration mechanism, it is fair to compare them to one another based on the magnitudes of the capillary forces. Nonionic 2 outperformed the other nonionic systems; this was expected because it had the lowest contact angle. However, in general, all of the nonionic surfactant systems achieved similar recoveries (within a 5% difference) due to their similar ability to alter the wettability, along with their similar IFTs. Most managed to at least shift the wettability from extremely oil-wet to an intermediate wettability. No oil recovery was observed on the imbibition recovery curve. This was expected, due to it having the highest IFT and contact angle of all the systems tested in the carbonate-rich environment.

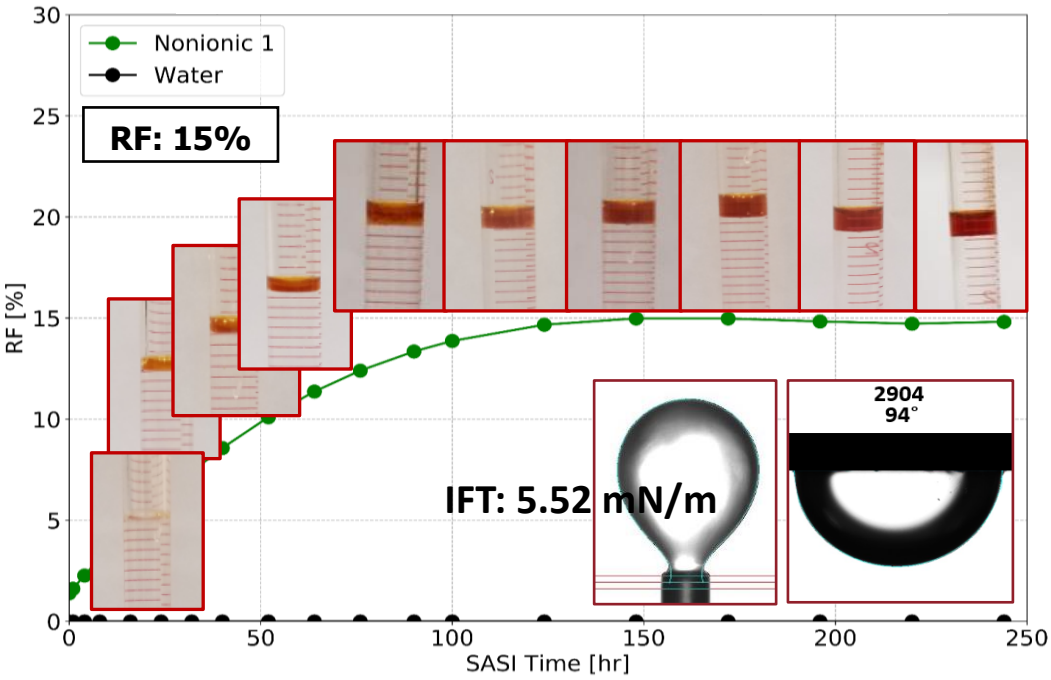

Figure 4-10 Oil recovery, IFT, and contact angle comparison for Nonionic 1 in the carbonate-rich environment.

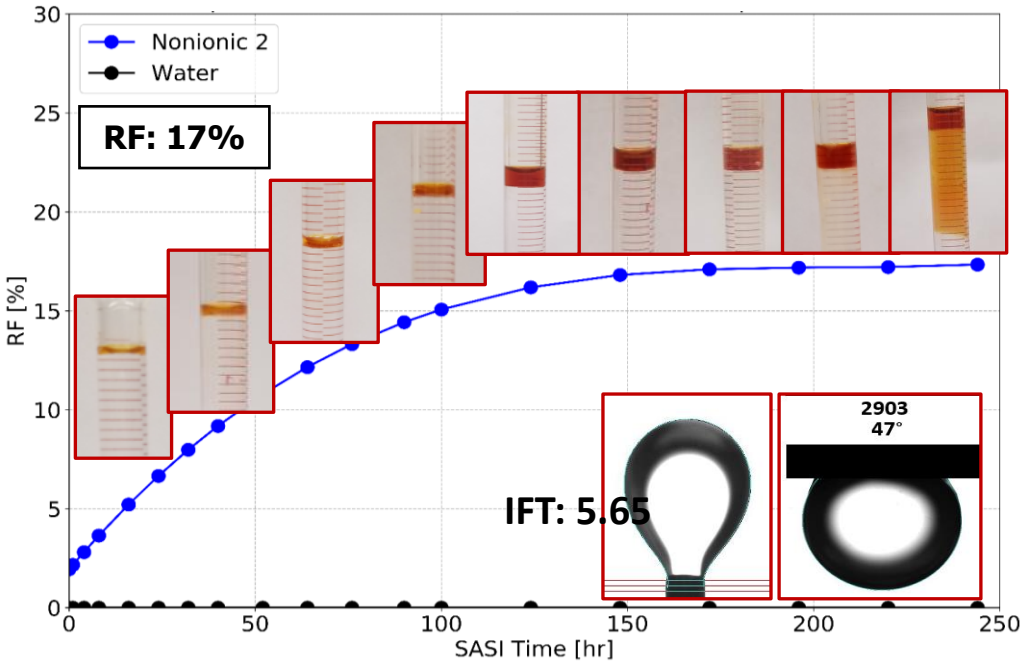

Figure 4-11 Oil recovery, IFT, and contact angle comparison for Nonionic 2 in the carbonate-rich environment.

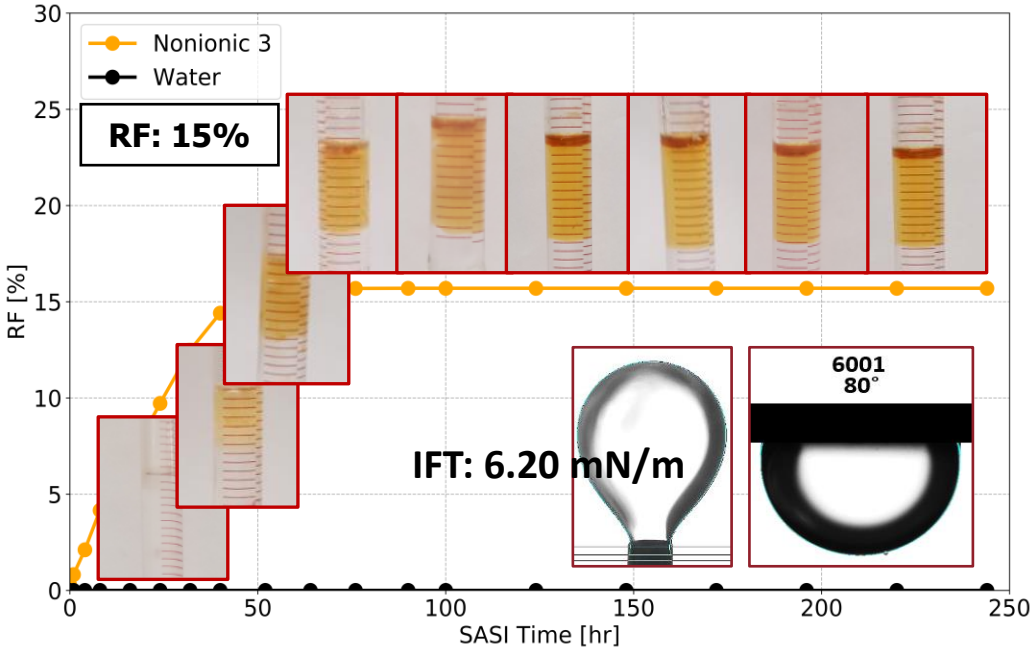

Figure 4-12 Oil recovery, IFT, and contact angle comparison for Nonionic 3 in the carbonate-rich environment.

4.4.2 Computed Tomography Scan Imaging and Oil Displacement

Images obtained from the CT scanner were processed using ImageJ software to optimize the image quality. A color bar was assigned to each image not only to provide a better contrast among the different porosities distributed in the core sample, but also to monitor the fluid's displacement throughout the SASI experiment. Brighter colors (i.e., higher CT numbers) represent higher densities while darker colors (i.e., lower CT numbers) represent lower densities, as shown in the color bar for each figure presented in the oil displacement analysis section. Quartz-rich core plug samples were observed to have similar threshold configurations. Carbonate-rich core samples were observed not to have similar threshold configurations, which can be attributed to the heterogeneity of each core sample. However, to better monitor the oil displacement and surfactant imbibition, the image threshold was kept constant for all scans performed at different times for each core

plug. The orientation of the XYZ 3D plane used in scanning the core samples is shown in **Figure 4-13.**

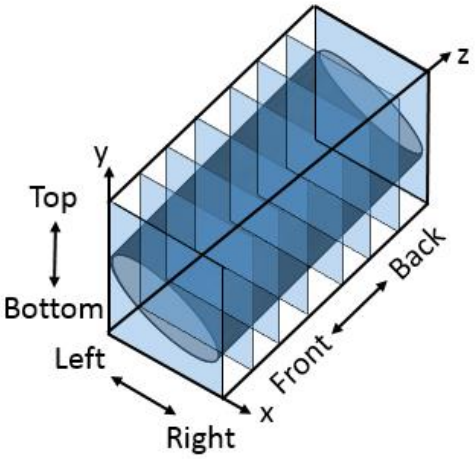

Figure 4-13 XYZ plane orientation for the core plugs in the CT scanner.

The CT scanner scanned the samples in all directions, including the entire length of each sample (i.e., the z-direction). The present research examined multiple slices separately, taken in the xy direction from each core sample. Changes in the CT numbers throughout SASI were directly related to fluid imbibition and oil displacement. The oil CT number was close to 300 HU (doped with 5 wt% iodobenzene) while the doped water/surfactant had a CT number of approximately 850 HU (doped with 4 wt% potassium iodide), both at reservoir temperature. This substantial difference in CT numbers allowed for clear monitoring of the fluid displacement in the cores during the experiment. Imbibition was observed through a positive increase in the CT numbers, over time. The greater the change, the more oil that was displaced in the cores by the water/surfactant.

The general trend observed for all core samples was that the overall color of the slices lightened as the SASI time increased, an indication of the aqueous phase imbibing into the rock sample and replacing the oil. CT images at different times during the SASI experiments on quartz-rich samples are shown in **Figure 4-14** to **Figure 4-18**. In most of

the quartz-rich samples, it can clearly be seen that imbibition occurred in the initial or final slices, with minimal changes in the slices taken from the middle of the plugs. This can be attributed to the fact that the majority of the oil was contained in the two fronts of the plugs, with negligible amounts in the centers. Another observation is that the majority of the imbibition commenced from areas where the CT number was high (i.e., low porosity) to begin with, indicating that the imbibed fluid got into smaller pores first, as evidenced by Slice 21 in **Figure 4-14**. Slice 120 in the same figure shows a bedding plane, which acted as a high permeability path for the fluid to imbibe into smaller pores; the green color (i.e., a lower average CT number) turned to a bright blue color (i.e., a higher average CT number). The concept was applied to the rest of the quartz-rich samples' CT images, and the observed trend was similar in all.

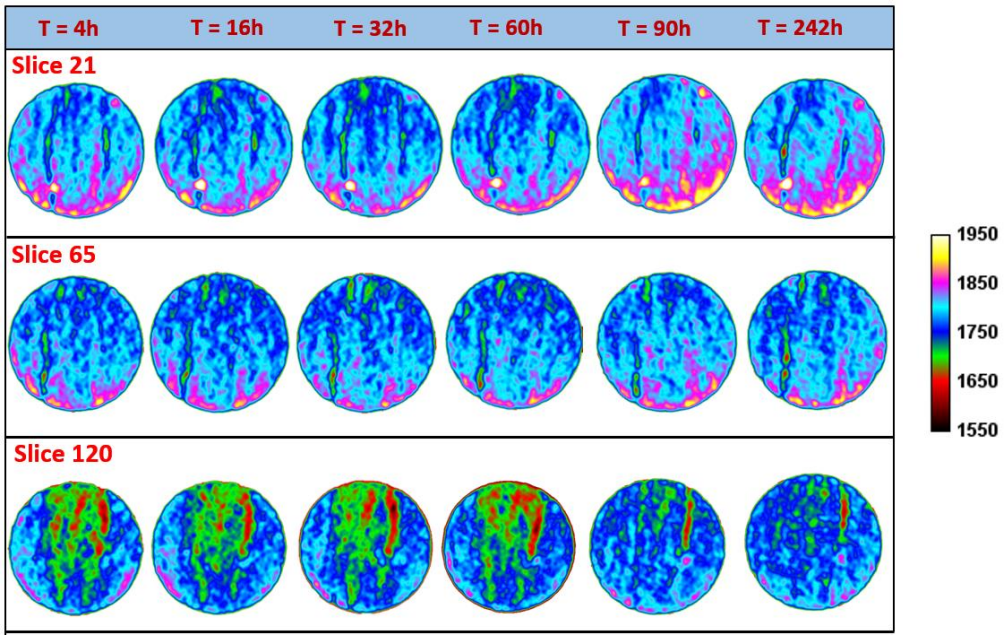

Figure 4-14 Certain xy time slices taken from Quartz-rich 1 during spontaneous imbibition from Nonionic 1.

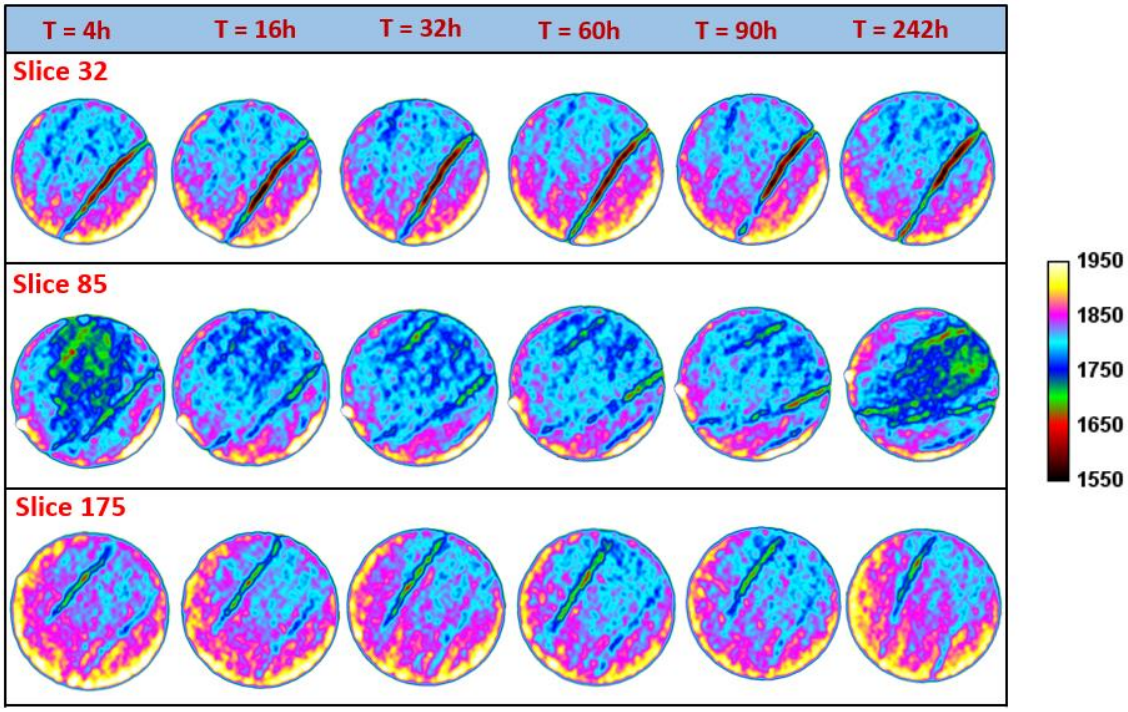

Figure 4-15 Certain xy time slices taken from Quartz-rich 2 during spontaneous imbibition from water.

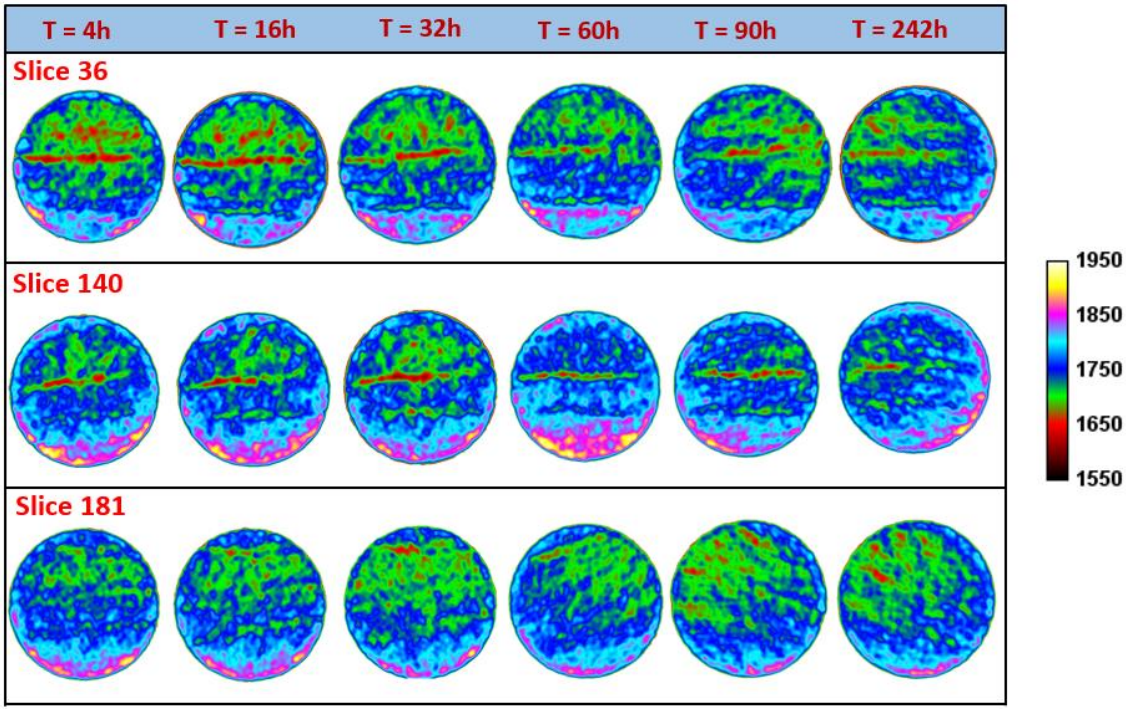

Figure 4-16 Certain xy time slices taken from Quartz-rich 3 during spontaneous imbibition from Nonionic 2.

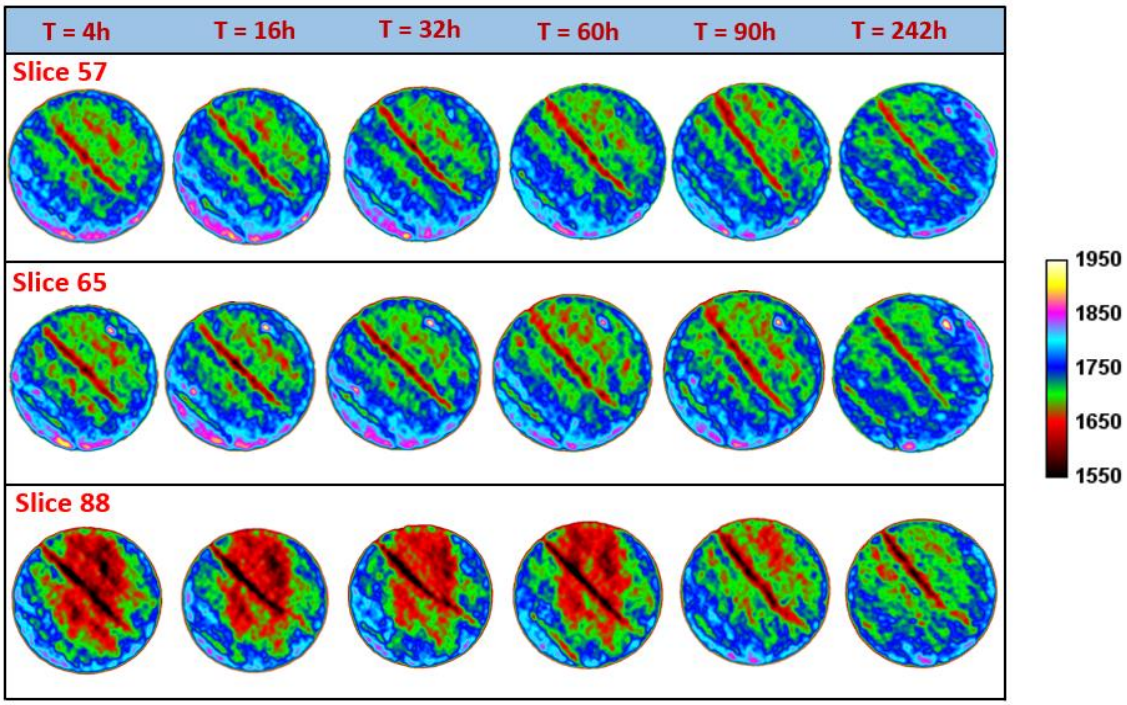

Figure 4-17 Certain xy time slices taken from Quartz-rich 4 during spontaneous imbibition from Cationic.

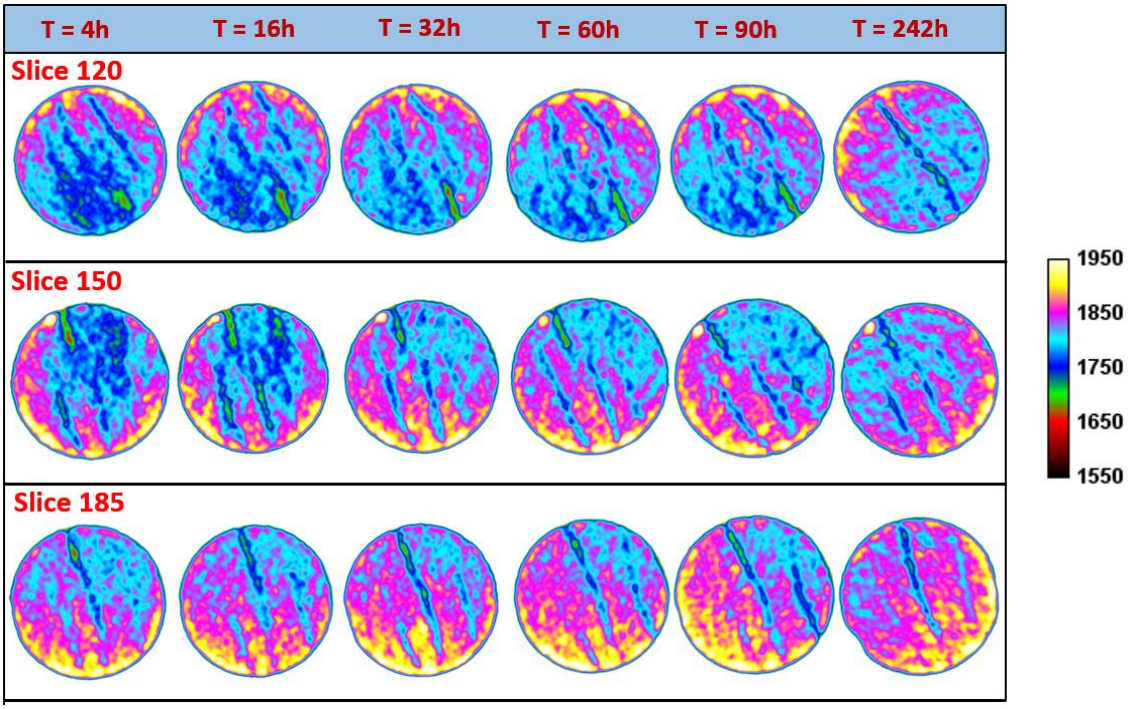

Figure 4-18 Certain xy time slices taken from Quartz-rich 5 during spontaneous imbibition from Nonionic 3.

It can be seen in most of the images that the carbonate-rich core samples were tighter in general, with greater average CT numbers than those of the quartz-rich samples. The majority of the imbibition occurred in smaller pores, as larger pores were less frequent. However, there are two observed cases where imbibition occurred in both small and large pores almost equally (i.e., C1 and C3). No movement (i.e., displacement) was observed in Carbonate# 2, as shown in **Figure 4-20**. All 200 slices were analyzed, and no clear movement was found. **Figure 4-19** to **Figure 4-23** show the xy CT images for all carbonate-rich samples at different times during the SASI experiments. None of the carbonate-rich cores showed any indication of bedding planes or high permeability streaks, which is another clear distinction between the carbonate and quartz samples.

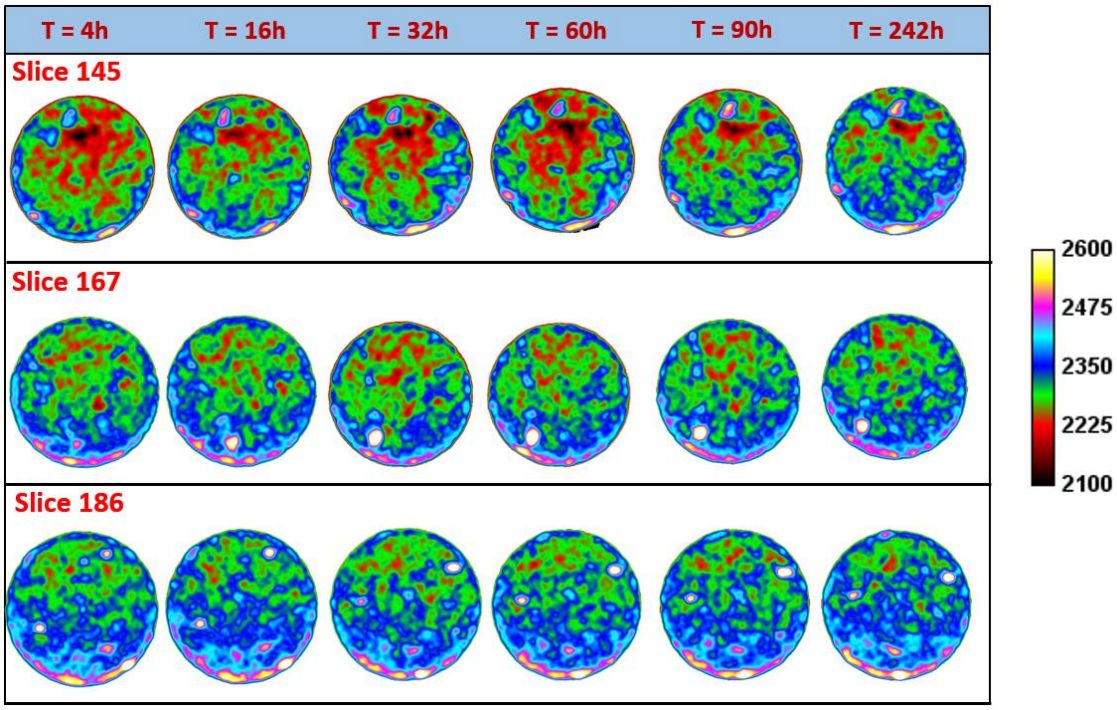

Figure 4-19 Certain xy time slices taken from Carbonate-rich 1 during spontaneous imbibition from Nonionic 1.

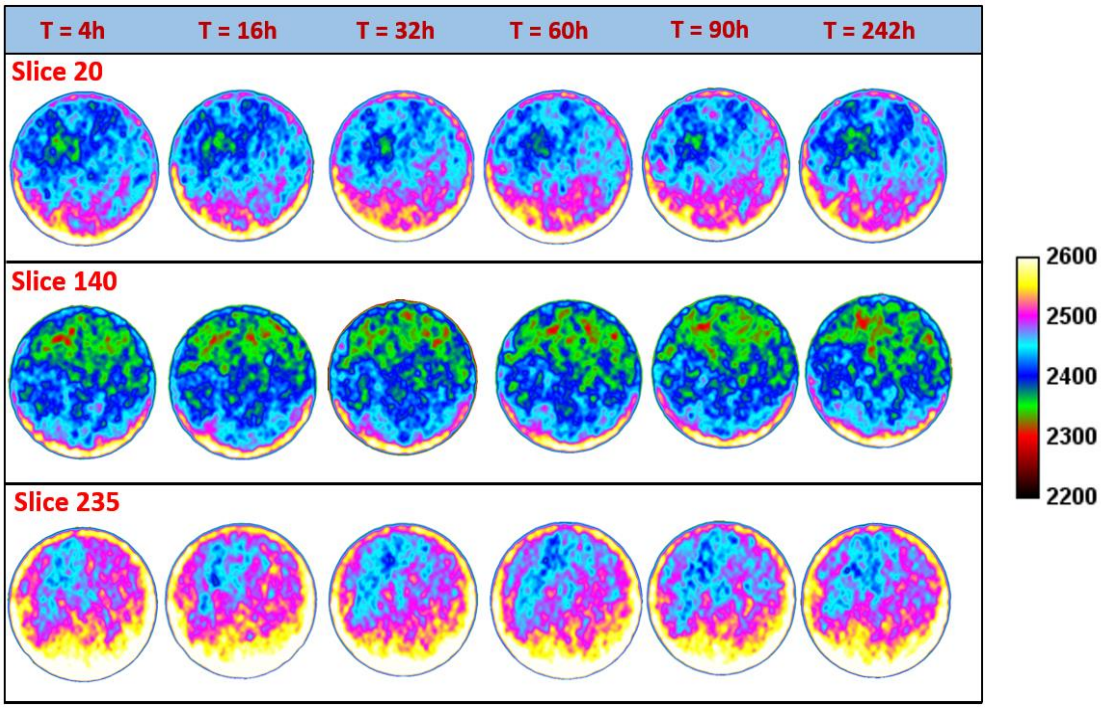

Figure 4-20 Certain xy time slices taken from Carbonate-rich 2 during spontaneous imbibition from DW.

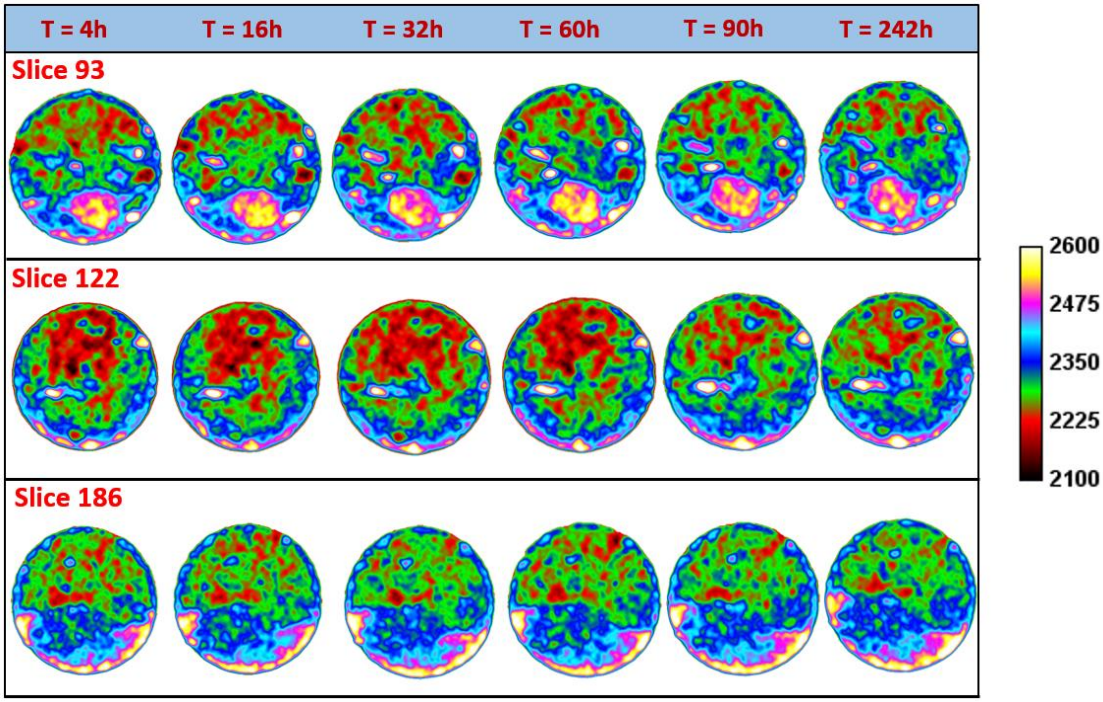

Figure 4-21 Certain xy time slices taken from Carbonate-rich 3 during spontaneous imbibition from Nonionic 2.

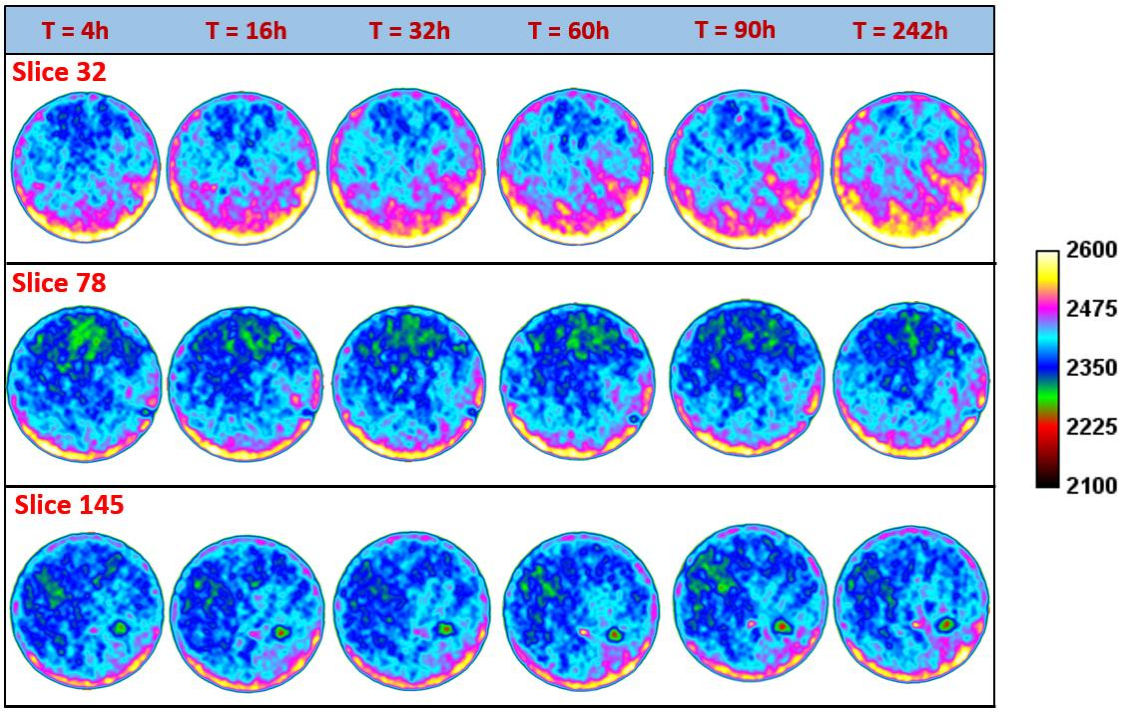

Figure 4-22 Certain xy time slices taken from Carbonate-rich 4 during spontaneous imbibition from Cationic.

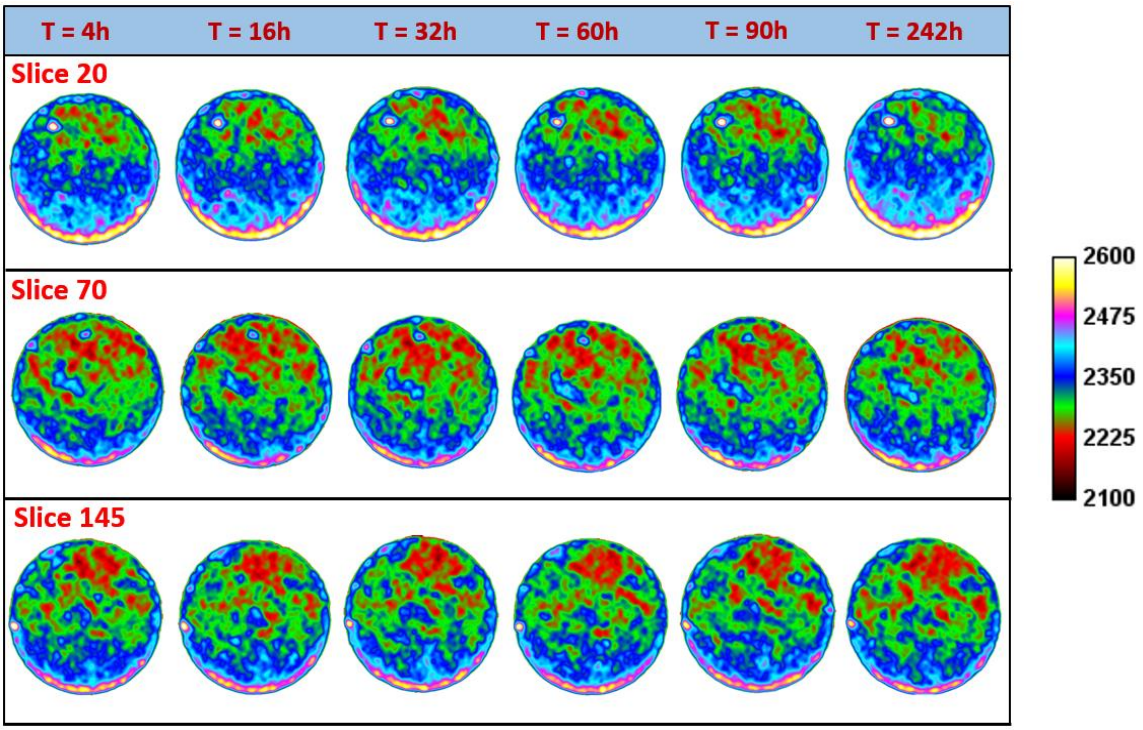

Figure 4-23 Certain xy time slices taken from Carbonate-rich 5 during spontaneous imbibition from Nonionic 3.

CHAPTER 5

TEXTURE CHARACTERIZATION AND SPONTANEOUS IMBIBITION FLUID TYPING AND DISTRIBUTION

During spontaneous imbibition, a wetting liquid is drawn into the porous medium of a core by capillary forces. In uniform systems such as homogenous clastic formations, the liquid imbibes, forming a continuous interface and making the PSD effect almost negligible. However, the spontaneous imbibition mechanism in tight rocks is not well understood. Many researchers believe that high permeability cores tend to exhibit low levels of spontaneous imbibition oil recovery because of the low capillary forces. Uncertainty arises from the fact that it is not known if the non-wetting fluid, be it surfactant or water, imbibes into small pores, resulting in oil recovery from those small pores. If this is true, a hybrid of spontaneous imbibition and gas injection, be it CO_2 or sales gas, could provide the optimum approach, retrieving the most oil from tight rocks after primary depltion through EOR means. For this reason, the effects of PSD on spontaneous imbibition were analyzed through NMR T_2, spatial (2D) NMR mapping, and FE-SEM imaging.

5.1 Methodology

In this research, T_2 relaxation times were used as an indication of the PSD; meanwhile, (2D) NMR mapping was used for displacement analysis because core plugs and displacement processes are not homogeneous. The (2D) NMR mapping, often called soin-echo single point imaging (SE-SPI) (Petrov and Balcom 2011), was used to differentiate between fluids based on their various viscosities. For instance, water and

kerogen are easily differentiated using T_1 and T_2 maps, due to their different apparent viscosities. The T_1 and T_2 values tend to be similar for fluids with low viscosities. As viscosity increases, however, T_1 and T_2 deviate (Bloembergen, Purcell, and Pound 1947). The main limitation of this technique relates to low permeability rocks. Long acquisition times for (2D) NMR maps resulting from small signal-to-noise ratio (SNR) and large tau values make these maps unusable for tight rocks. This problem is usually mitigated by utilizing a higher frequency spectrometer.

Field emission scanning electron microscope (FE-SEM) imaging was employed in this work to achieve the best fit, in order to minimize the error associated with determining conventional rock relaxivity. Polished rock chips were prepared using a low-viscosity medium before the final polish to reduce damage induced from mechanical polishing. The surface rock relaxivity was calculated statistically using the lognormal distribution mean obtained from a Gaussian fit, which is consistent with the NMR T_2 logarithmic mean. A Python Scipy statistics package (i.e., Scipy.stats.lognorm) was used to fit the data and calculate the log mean and variance accordingly.

5.2 Discussion

Capillary pressure is related to the contact angle and interfacial tension. As explained in **Chapter 2**, capillary pressure is a function of contact angle, interfacial tension, and pore radius. In this work, instead of using a centrifuge to obtain the P_c, capillary forces were investigated via NMR. The T_2 value, along with surface relaxivity, were used in the Young–Laplace equation in place of the pore radius r. The main emphasis

on T_2 can be attributed to the greater body of information acquired and shorter measuring time compared to T_1. Inverse T_2 can be expressed by **Eq. (5-1)**:

$$\frac{1}{T_2} = \frac{S}{T_2} + \frac{D}{T_2} + \frac{B}{T_2} \tag{5-1}$$

where the surface relaxation is represented by $\frac{S}{T_2}$, diffusion relaxation due to the effects of the magnetic gradients $\frac{D}{T_2}$, and bulk relaxation $\frac{B}{T_2}$, and all are measured in 1/ms. The above equation can be further expanded into **Eq. (5-2)**:

$$\frac{1}{T_2} = \rho \frac{S}{V} + \frac{D(\gamma GTE)2}{12} + \frac{1}{T_2 B} \tag{5-2}$$

where $\frac{1}{T_2 B}$ is extremely small compared to $\frac{1}{T_2}$, and thus can be neglected. Also, G in the second term denotes the magnetic gradient, which is 0 in a uniform magnetic field. Thus, the second term can also be neglected.

Since fluid interaction with the rock surface is the dominant relaxation mechanism, the transversal relaxation rate $\frac{1}{T_2}$ can be approximated following the Brownstein and Tarr (1979) approximation, as shown in **Eq. (5-3)**:

$$\frac{1}{T_2} = \rho \frac{S}{V} = \rho \frac{c}{r} \tag{5-3}$$

where ρ is the surface relaxivity, a constant denoting the influence of relaxation induced by fluid interaction with the rock surface; $\boldsymbol{r}$ is the pore radius; and $\boldsymbol{c}$ is the shape factor, which is often assumed to be 2 for cylindrical samples or 3 for spherical samples. The surface relaxivity can be estimated iteratively by matching the relaxation times obtained from the NMR with the independent PSD measurements, solely using NMR data, or through other means such as by employing rock surface area correlations. Benavides et al.

(2017) proposed another method for estimating surface relaxivity that is based on simulating the NMR T_2 signal for a given surface relaxivity function using the random walk method, while different surface relaxivity functions are ranked based on correlation of the resulting simulated T_2 distributions, as compared to the measured T_2 distribution. The only drawback of this method is that it requires a micro-tomographic image of the subject rock sample, which is often unavailable.

Surface relaxivity depends on the paramagnetic mineral content of the rock sample. Thus, clay minerals such as illite, kaolinite, and smectite are often more of interest than any other minerals in the rock sample. The linear correlation between surface relaxivity and illite content was introduced by Saidian and Prasad (2015), who claimed that it resulted in a decent estimation with an R^2 of 0.79. The correlation is as follows:

$$\rho = 0.067 \times fil + 0.56 \tag{5-4}$$

where *fil* is the wt% of illite. The correlation was obtained by analyzing more than 28 Bakken samples through a nitrogen adsorption technique, as explained by Kuila (2013), and then correlating with the NMR T_2 distribution. In this work, the rock relaxivity was obtained by fitting the SEM results from different polished rock chips with the NMR results obtained from scanning the whole core. Since the pore radius is proportional to the relaxation time T_2, r in the Young-Laplace equation can be replaced by the term $cT_2.\rho$, as shown in **Eq. (5-6)**:

$$\mathrm{Pc} = \frac{2\sigma \cos\theta}{\mathrm{r}} \tag{5-5}$$

$$Pc = \frac{2\sigma \cos\theta}{c.T_2.\rho} \tag{5-6}$$

where the wettability is represented by contact angle θ, interfacial tension σ, pore radius r, relaxation time T_2, surface rock relaxivity ρ, and shape constant c.

5.3 Results

A series of low field NMR measurements, including T_2 and 2D spatial NMR, was conducted to evaluate the effects of PSD on spontaneous imbibition oil recovery. Crude oil movement was evaluated by monitoring the viscosity difference before and after the spontaneous imbibition experiment, through 2D NMR mapping. The NMR instrument used in this study was a Maran Ultra 23 MHz NMR analyzer located in the Aramco Advanced Research Center in Houston. A higher frequency (i.e., 23 MHz) was used for higher sensitivity, in order to detect and analyze small pores. The data were extracted with green imaging technology (GIT), transformed using a BDR model, and processed through the application of linear interpolation on 15,000 by 15,000 grid blocks, using Python. The main NMR measurement parameters are listed in **Table 5-1.**

Table 5-1 NMR Measurement Parameters

Parameter	Value
Recycle Delay, ms	1,000
Number of TI Values	30
Dwell Time, ms	0.008
Gain, dB	49
T2Max, ms	100
Number of Echoes	4,386
Level	0.5
Tau, ms	0.057
Filter	125
Window	1
T1Max, ms	100
Calibration, m.u.	0.00004
P180, ms	0.0218
P90, ms	0.0104
Resonant Frequency, kHz	0.0103

Rock chips were embedded in epoxy and then polished with different grits to ensure proper smoothness. Also, the embedded samples were sputter coated with a thin layer of platinum palluiduim to eliminate the charging effect resulting from the non-conductive nature of the geological samples. If the samples were left uncoated, the accumulation of electrons on the surface of the rocks would result in low-quality images with unwanted extra-white regions. Thus, coating the samples with a thin layer of platinum palluiduim acted as a channel, removing the charged electrons from the surface of the samples. The SEM instrument used in this work was a JEOL JSM-7500F, as shown in **Figure 5-1**. This instrument is an ultra-high resolution field emission scanning electron microscope (FE-SEM) equipped with a high brightness conical field emission gun and low aberration conical objective lens. This addition enabled specimen observation at magnifications up to 1,000,000x with a resolution as low as 1 nm at 5kV and 2.2 nm at 1.0kV. The SEM machine was located in the Materials Characterization Facility (MCF) at Texas A&M University, College Station Campus.

Figure 5-1 FE-SEM JEOL JSM-7500F at TAMU MCF.

5.3.1 Materials Characterization and Petrophysical Analysis

All 10 core plugs were scanned using the above-mentioned NMR system to obtain PSD post-saturation prior to conducting the spontaneous imbibition experiment. The T_2 distributions were obtained and plotted against the cumulative volume, as shown in **Figure 5-16**. The cumulative volume in the cores was the summed volume for each incremental portion obtained from the T_2 response. The incremental volume was directly proportional to the frequency of occurrence of the pore spaces in the porous medium. Rock chips were prepared from core samples taken from the same formation at the same exact depth as the core samples used for SASI. **Figure 5-2** shows some of the images taken using FE-SEM; it is evident that some rock chips had different pore structures than did others.

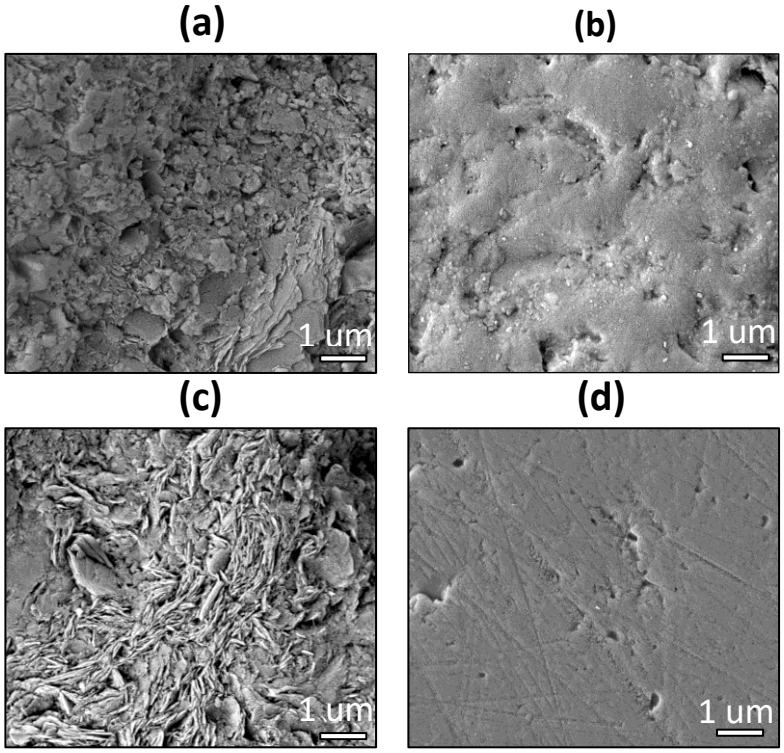

Figure 5-2 FE-SEM micrographs featuring: (a) Quartz #1 structure showing more pores of different sizes, (b) Quartz #2 pore structure showing smaller and less frequent pores, (c) illite clay mineral sheets found in most quartz-rich samples, and (D) Carbonate #4 with extremely few pores.

The FE-SEM images were processed using an open source modified python package Quantitative Analysis of Microscopy Images (AQUAMI). The package performs several thousand measurements of an image and reports information such as the mean feature dimensions, size distribution, and phase area fraction (Stuckner et al. 2017). **Figure 5-3** shows the workflow followed in this research for the quantitative PSD analysis, using the AQUAMI open source package.

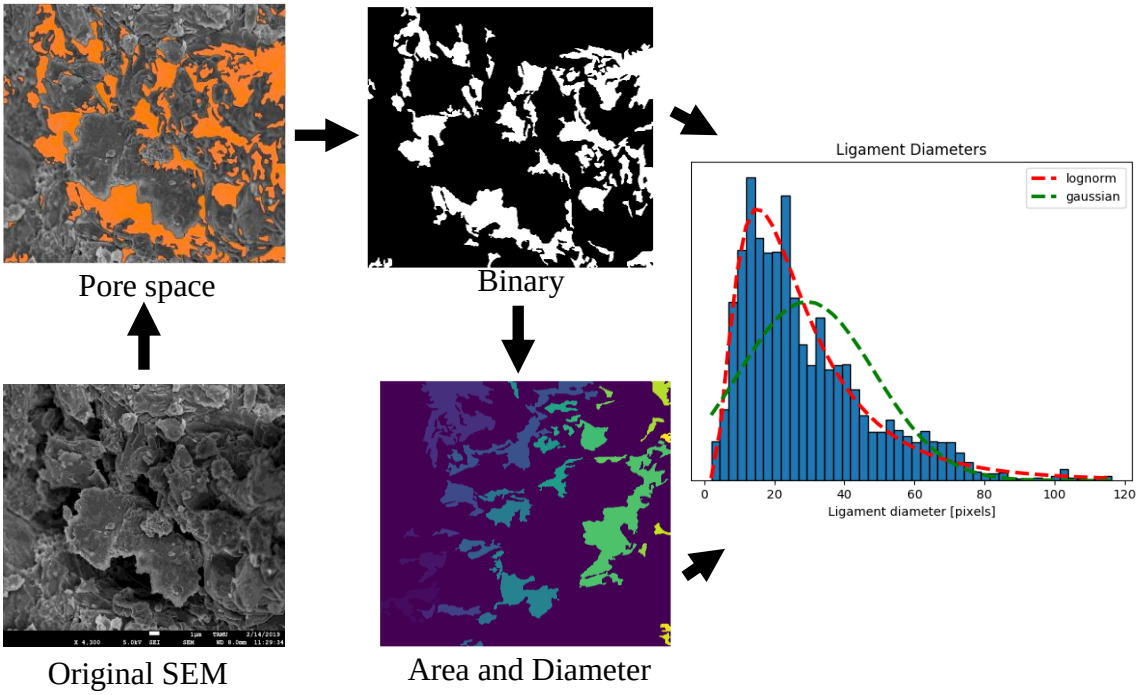

Figure 5-3 AQUAMI Python package and GUI workflow used for quantitative pore size distribution analysis of FE-SEM images.

Low-quality rocks with low permeabilities and minimal porosities have complex microstructural information that is quantifiable in theory, yet difficult to extract in practice. A perfect fit between NMR and FE-SEM pore size distribution can never be achieved, not only because of the different sample sizes needed for the two measurements, but also the high difficulty encountered in extracting accurate pore sizes from images. At

this level, image processing is more of an art than a science. Given that the samples, especially clastic samples, have some clay-bound water and a large number of inorganic pores, the result is dual or triple porosity systems. In such cases, it is difficult to compare NMR with pore size distribution because there are at least two different surface relaxivities. Therefore, it is more representative only to compare the long T_2 peak with pore size distribution in organic matter obtained from FE-SEM PSD.

The T_2/pore radius conversion can be achieved by fitting the NMR PSD with the FE-SEM PSD. However, fitting the SEM data with the NMR data requires substantial statistical analysis. In such cases, we can assume that all pores from the SEM data are spherical, and the pore radius r (μm) is related to the T_2 relaxation time, as shown in **Eq. (5-7):**

$$r = 3 * T_2 * \rho \tag{5-7}$$

Figure 5-4 to **Figure 5-8** illustrate the fitted data between the SEM and NMR for Quartz #1, #2, #3, #4, and #5. The NMR response and SEM data showed a strong correlation; the peak with the longest T_2 almost overlayed that of the normally distributed peak obtained from SEM. This strong correlation indicates that the NMR and SEM data in this case represented the pore body distribution. The average surface rock relaxivity for the Wolfcamp B quartz-rich samples was found to be around 0.0138 μm/ms, ± 0.0013 μm/ms. The only surface rock relaxivity that seemed to be relatively different was that of Quartz #1, which was evident by its larger pores and different PSD curve, as compared to the rest of the samples.

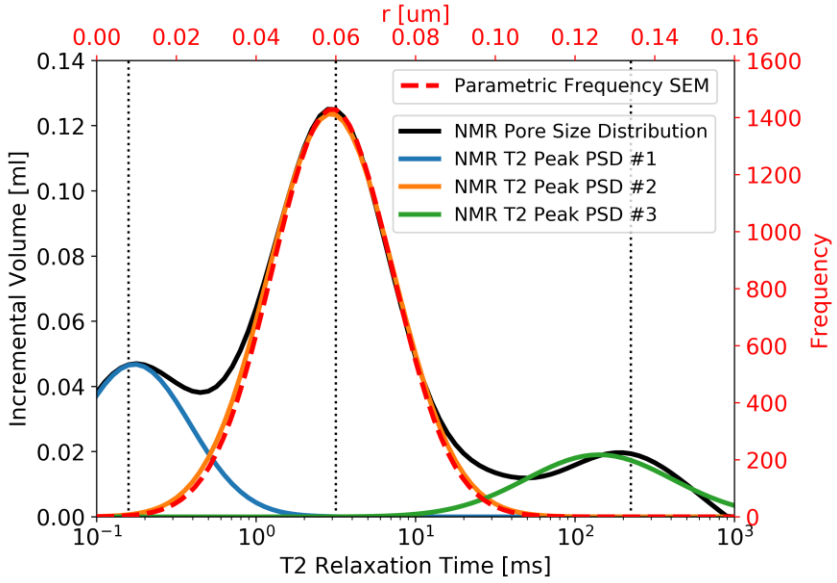

Figure 5-4 Quartz-rich #1 NMR PSD (solid black) and SEM PSD (dotted red) showing an excellent fit to the organic pores (Peak #2). FE-SEM LM: 0.0591 um, NMR T2 LM: 2.444 ms, and Rock Relaxivity: 0.00806 um/ms.

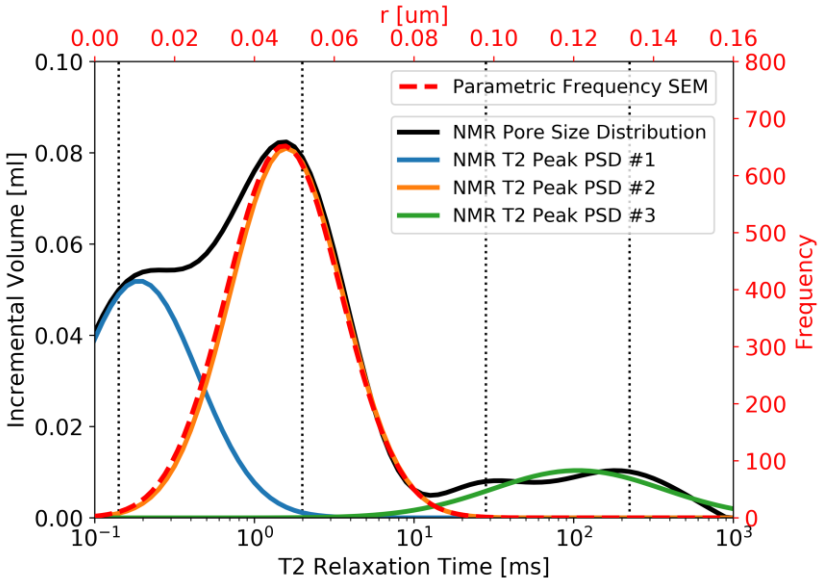

Figure 5-5 Quartz-rich #2 NMR PSD (solid black) and SEM PSD (dotted red) showing an excellent fit to the organic pores (Peak #2). FE-SEM LM: 0.0473 um, NMR T2 LM: 1.130 ms, and Rock Relaxivity: 0.0139 um/ms.

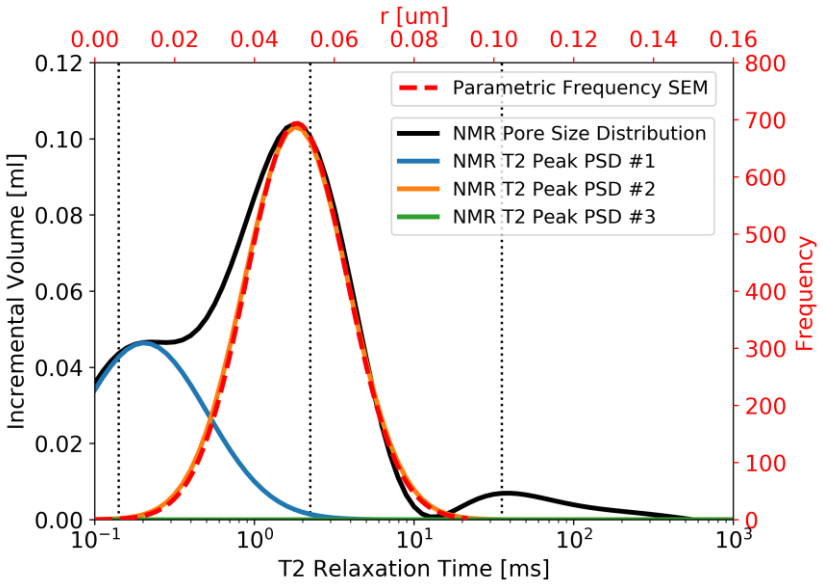

Figure 5-6 Quartz-rich #3 NMR PSD (solid black) and SEM PSD (dotted red) showing an excellent fit to the organic pores (Peak #2). FE-SEM LM: 0.0506 um, NMR T2 LM: 1.004 ms, and Rock Relaxivity: 0.0168 um/ms.

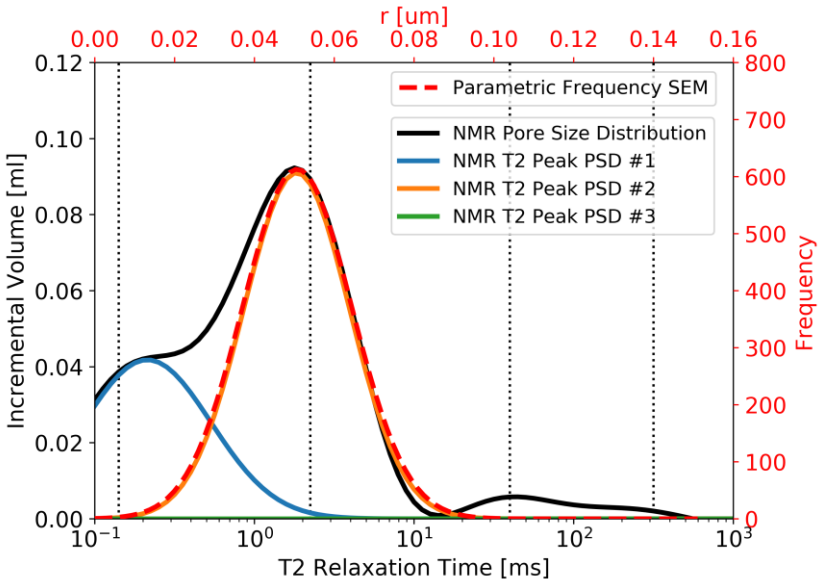

Figure 5-7 Quartz-rich #4 NMR PSD (solid black) and SEM PSD (dotted red) showing an excellent fit to the organic pores (Peak #2). FE-SEM LM: 0.0507 um, NMR T2 LM: 1.029 ms, and Rock Relaxivity: 0.0164 um/ms.

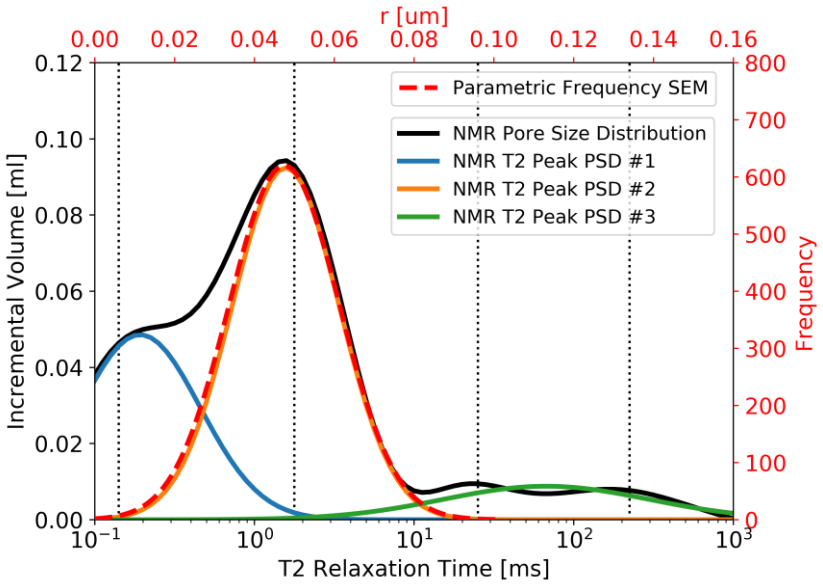

Figure 5-8 Quartz-rich #5 NMR PSD (solid black) and SEM PSD (dotted red) showing an excellent fit to the organic pores (Peak #2). FE-SEM LM: 0.0474 um, NMR T2 LM: 1.144 ms, and Rock Relaxivity: 0.01383 um/ms.

Figure 5-9 to **Figure 5-14** demonstrate the fitted data between SEM and NMR for Carbonate #1, #2, #3, #4, and #5. The NMR response and SEM data were strongly correlated. The peak with the longest T_2 almost overlayed that of the normally distributed peak obtained from SEM. Carbonate #2 had a unique T_2 distribution that could either be treated as a single Gaussian or multimodal distribution. Thus, it was fitted twice, as shown in **Figure 5-10** and **Figure 5-11**. The surface relaxivity was obtained twice for Carbonate #2. The percentage difference between the surface relaxivity values obtained from the two fitting methods was negligible, and either value could be used in practice. The average surface rock relaxivity for the Wolfcamp B carbonate-rich samples was found to be around 0.00756 µm/ms, ± 0.0001 µm/ms. The only surface rock relaxivity that seemed to be relatively different was Quartz #1, which is evident by its larger pores and different PSD curve, as compared to the rest of the samples.

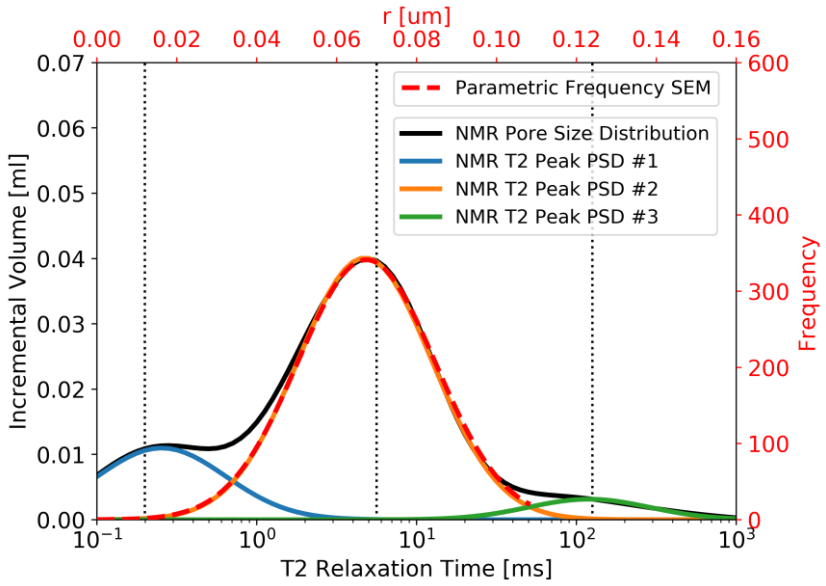

Figure 5-9 Carbonate-rich #1 NMR PSD (solid black) and SEM PSD (dotted red) showing an excellent fit to the organic pores (Peak #2). FE-SEM LM: 0.0637 um, NMR T2 LM: 2.690 ms, and Rock Relaxivity: 0.00790 um/ms.

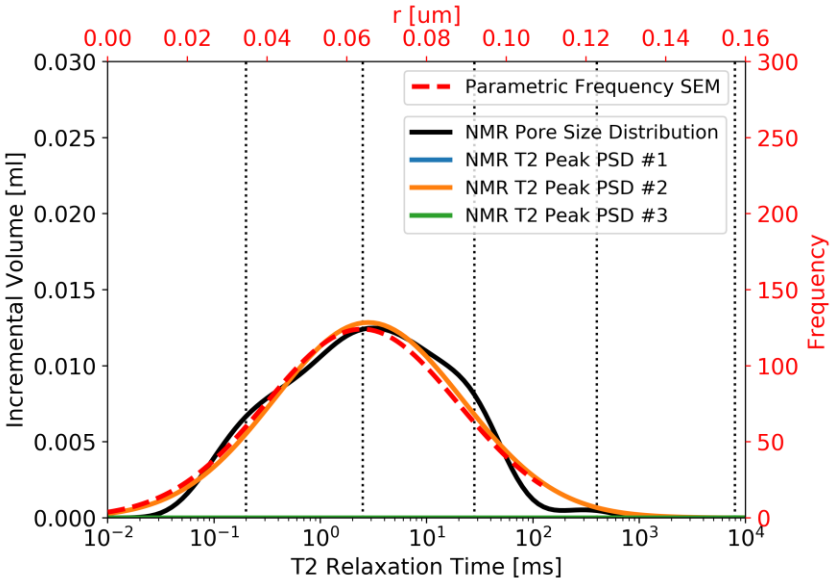

Figure 5-10 Carbonate-rich #2 NMR PSD (solid black) and SEM PSD (dotted red) showing a decent fit to the entire distribution. FE-SEM LM: 0.0670 um, NMR T2 LM: 3.220 ms, and Rock Relaxivity: 0.00698 um/ms.

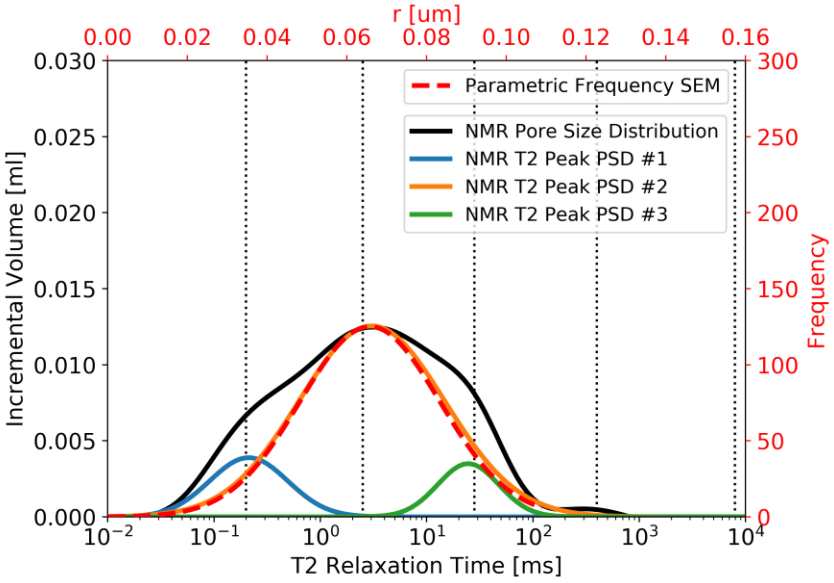

Figure 5-11 Carbonate-rich #2 NMR PSD (solid black) and SEM PSD (dotted red) refitted and showing an excellent fit to the organic pores (Peak #2). FE-SEM LM: 0.0657 um, NMR T2 LM: 3.220 ms, and Rock Relaxivity: 0.00815 um/ms.

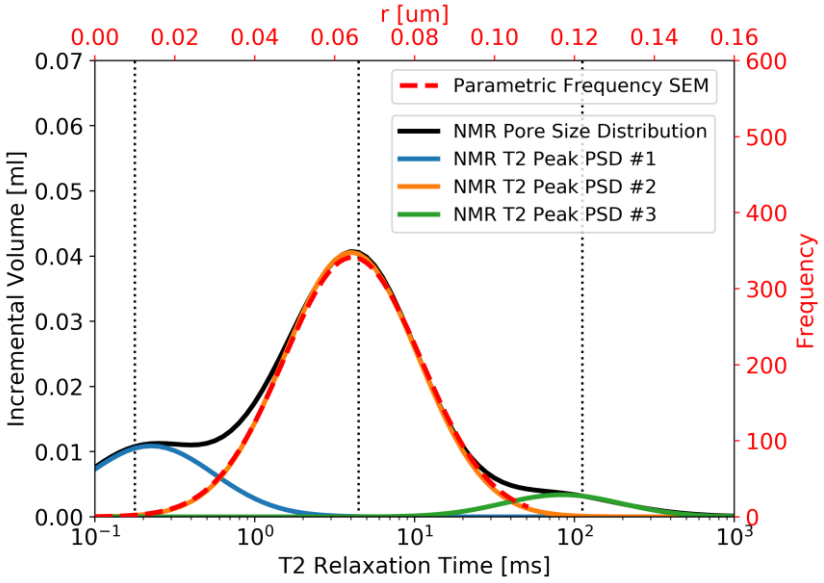

Figure 5-12 Carbonate-rich #3 NMR PSD (solid black) and SEM PSD (dotted red) refitted and showing an excellent fit to the organic pores (Peak #2). FE-SEM LM: 0.0644 um, NMR T2 LM: 2.793 ms, and Rock Relaxivity: 0.00769 um/ms.

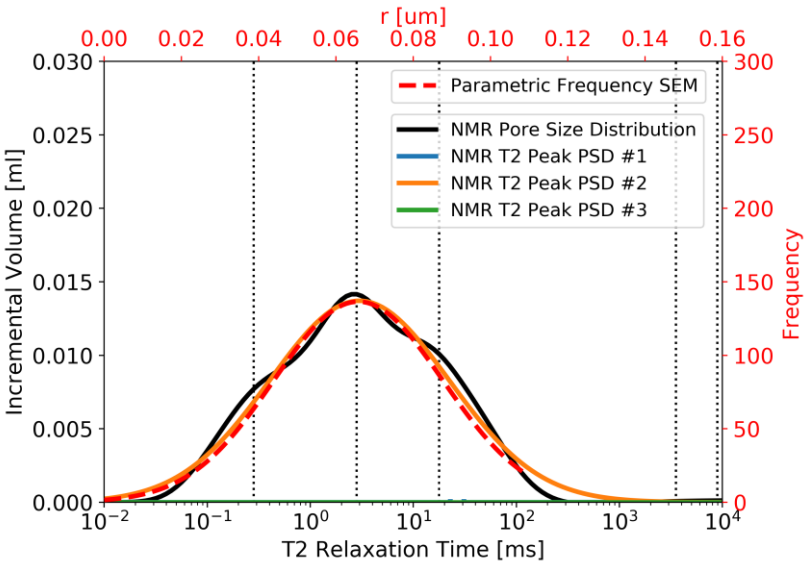

Figure 5-13 Carbonate-rich #4 NMR PSD (solid black) and SEM PSD (dotted red) showing a decent fit to the entire distribution. FE-SEM LM: 0.0657 um, NMR T2 LM: 2.963 ms, and Rock Relaxivity: 0.00739 um/ms.

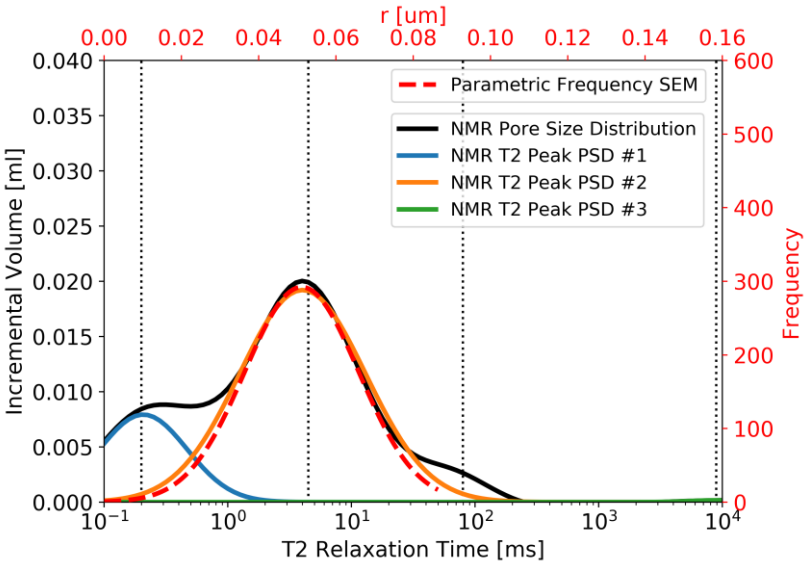

Figure 5-14 Carbonate-rich #5 NMR PSD (solid black) and SEM PSD (dotted red) showing an excellent fit to the organic pores (Peak #2). FE-SEM LM: 0.0511 um, NMR T2 LM: 2.235 ms, and Rock Relaxivity: 0.00763 um/ms.

After comparing the ρe values from the quartz- and carbonate-rich samples, it was evident that the latter had slightly larger pores on average. However, the frequency of occurrence of such pores was scarce, resulting in lower overall porosity values. It is worth noting that both NMR and SEM represent pore body distribution, while the lognormal distributions obtained from Mercury injection capillary pressure (MICP) represent pore throat distribution. Sulucarnain, Sondergeld, and Rai (2012) conducted a study attempting to match NMR spectra with MICP curves to estimate the scaling parameters for certain shale samples. In their study, Sulucarnain et al. found that the range of effective scaling surface relaxivities averaged at 0.0017 μm/ms, which is significantly smaller than what was found in this work. Such findings support the idea that NMR does indeed represent pore body distribution, while MICP represents pore throat distribution.

Figure 5-15 indicates that the majority of the oil in Quartz #1 was located in smaller pores, but pores larger than those containing CBW. Generally, fluids contained in core samples are divided into three main categories: (1) capillary-bound fluid, (2) clay-bound water, and (3) moveable fluids. In the NMR sense, bound fluid is defined as fluid that has an NMR signal below that of 33 ms in sandstone and around 100 ms in carbonates. Following the above-mentioned cutoffs, the majority of the fluids contained in the tested Wolfcamp samples were below the desired range for a moveable fluid. The T_2 cutoff for CBW or hydration water in the tested Wolfcamp samples, as referred to in Hill, Shirley, and Klein (1979), was found to be around 0.1 to 0.15ms at room temperature. Thus, the CBW appeared to be contained in micropores that were < 1 nm, which was as expected

because CBW is not free to move, due to being attached to the clay materials. Thus, producing it is not physically possible.

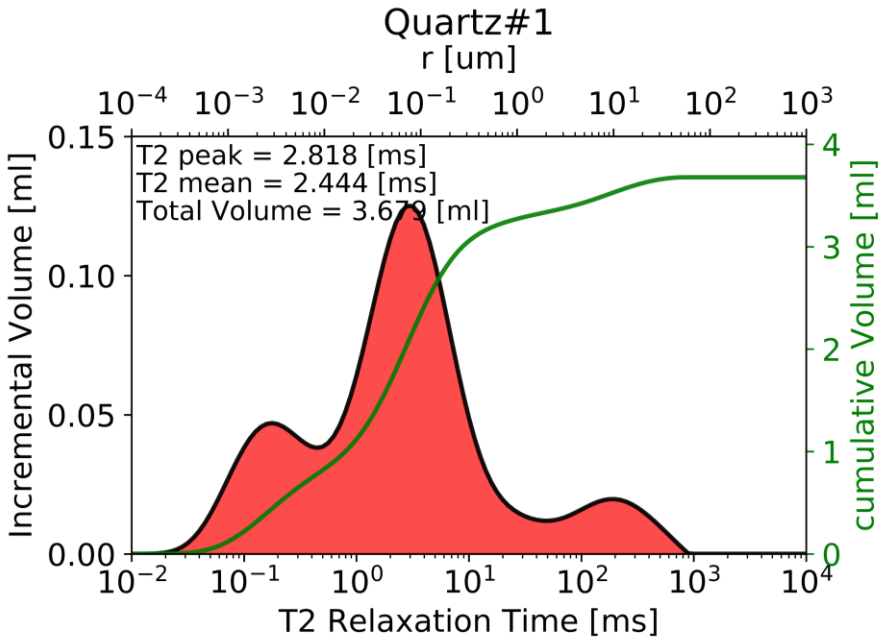

Figure 5-15 Quartz #1 T_2 distributions. The primary x-axis is the T_2 values, while the y-axis is the cumulative volume of fluid contained in the cores. The cumulative volume of the cores is plotted in green (right), while the pore radius is shown on a secondary x-axis

In this sample, the majority of the moveable oil was contained in pores ranging from 8 to 60 nm. Also, the tail at the higher T_2 values is an indication of a high permeability streak, larger pores, or even a fracture, conditions observed frequently in all of the tested quartz-rich Wolfcamp samples due to the presence of illite. The average ESR for Quartz #1 was around 58 nm. This average was obtained by utilizing the deduced surface relaxivity for Quartz #1 and converting the logaretherimic mean of T_2 to a single average logaretherimic ESR value. Applying the surface relaxivity conversion concept to the rest of the samples, we were able to produce **Figure 5-16.**

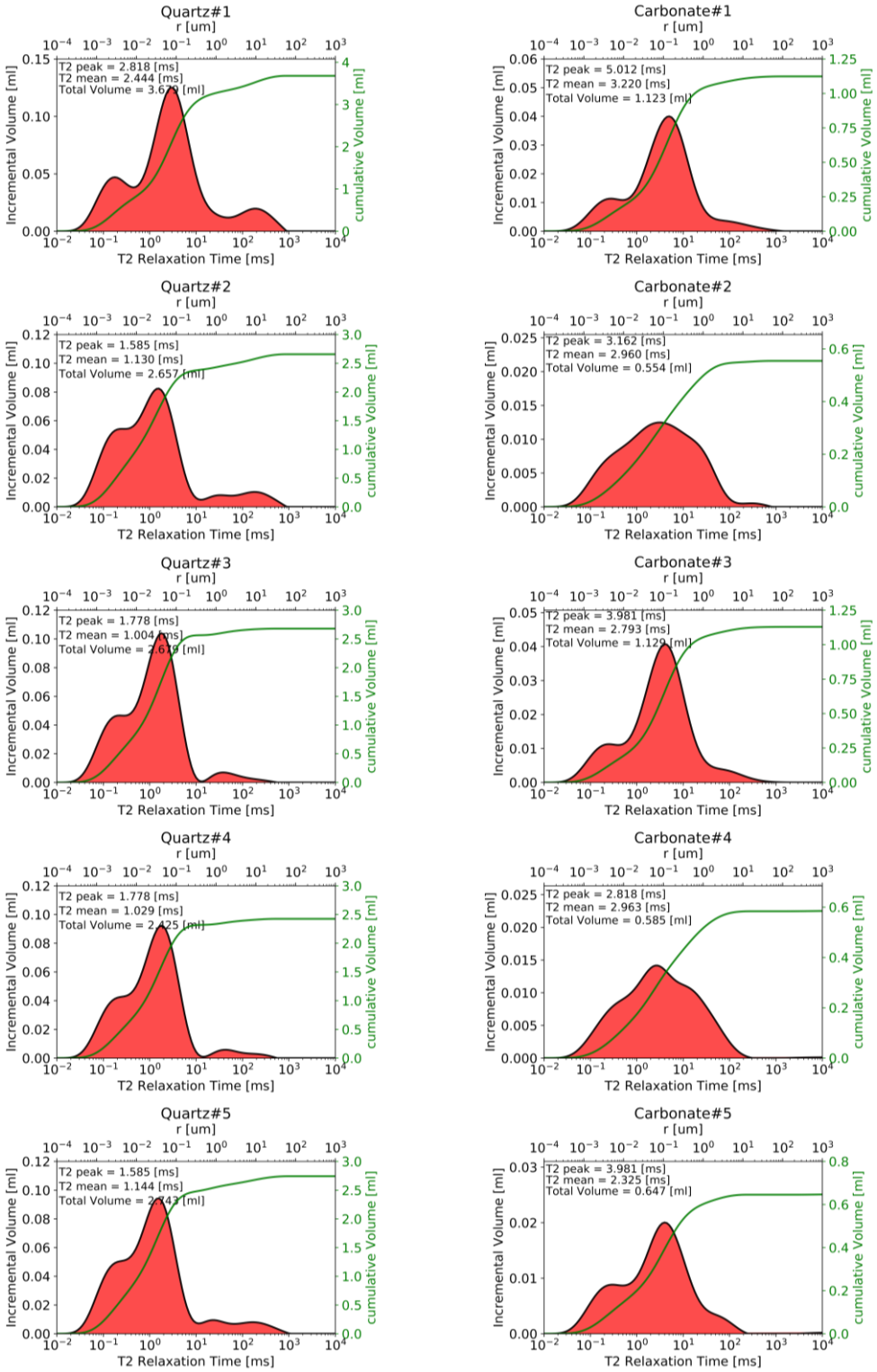

Figure 5-16 T_2 distributions for 10 cores after four weeks of oil saturation: five quartz-rich (left) and five carbonate-rich (right).

The quartz-rich cores had higher porosity values than did the carbonate-rich cores. Some appeared to have some clay-bound water (CBW), up to five times more in the quartz-rich than in the carbonate-rich samples, due to the presence of a considerable amount of clay minerals such as illite. The percentage of illite in the quartz-rich cores was up to 20%, as compared to 3.5% in the carbonate-rich cores. However, the quartz-rich cores appeared to have higher total porosities, averaging around 10.36%, as compared to 2.6% for carbonate-rich cores. The PSD was different for each core. Carbonate #2 and Carbonate #4 appeared to have an equal amount of fluid contained in the larger and smaller pores (i.e., a normal distribution), as compared to the other carbonate-rich cores. The quartz-rich cores, however, did show more uniform distributions, with Quartz #1 having more fluid contained in the larger pores, as compared to the remaining quartz-rich samples. The spatial profile of the saturated core plugs was evaluated through 2D NMR mapping. **Figure 5-17** shows a bird's eye view of the 2D NMR of the 10 cores. Each plot was normalized based on the 2D NMR response of the subject core, allowing for a more lucid observation of the fluid contained in each core. The oil appeared to be more localized in the quartz-rich cores (1 to 10 ms) outside the CBW. The oil profile was wider in the carbonate-rich cores (1 to 100 ms), despite being lower in terms of quantity. In other words, the carbonate-rich cores had less total oil volume, with most of the oil contained in larger pores, as compared to the quartz where most of the oil was localized in smaller pores. The results show that the position of each proton population in the maps are: water: $T_1/T_2 \sim 1$ to 1.5, and in some situations oil: $2 < T_1/T_2 < 9$. Gas can clearly be distinguished as $T_1/T_2 > 10$. Thus, the T_1/T_2 contrast was used for fluid identification and contribution.

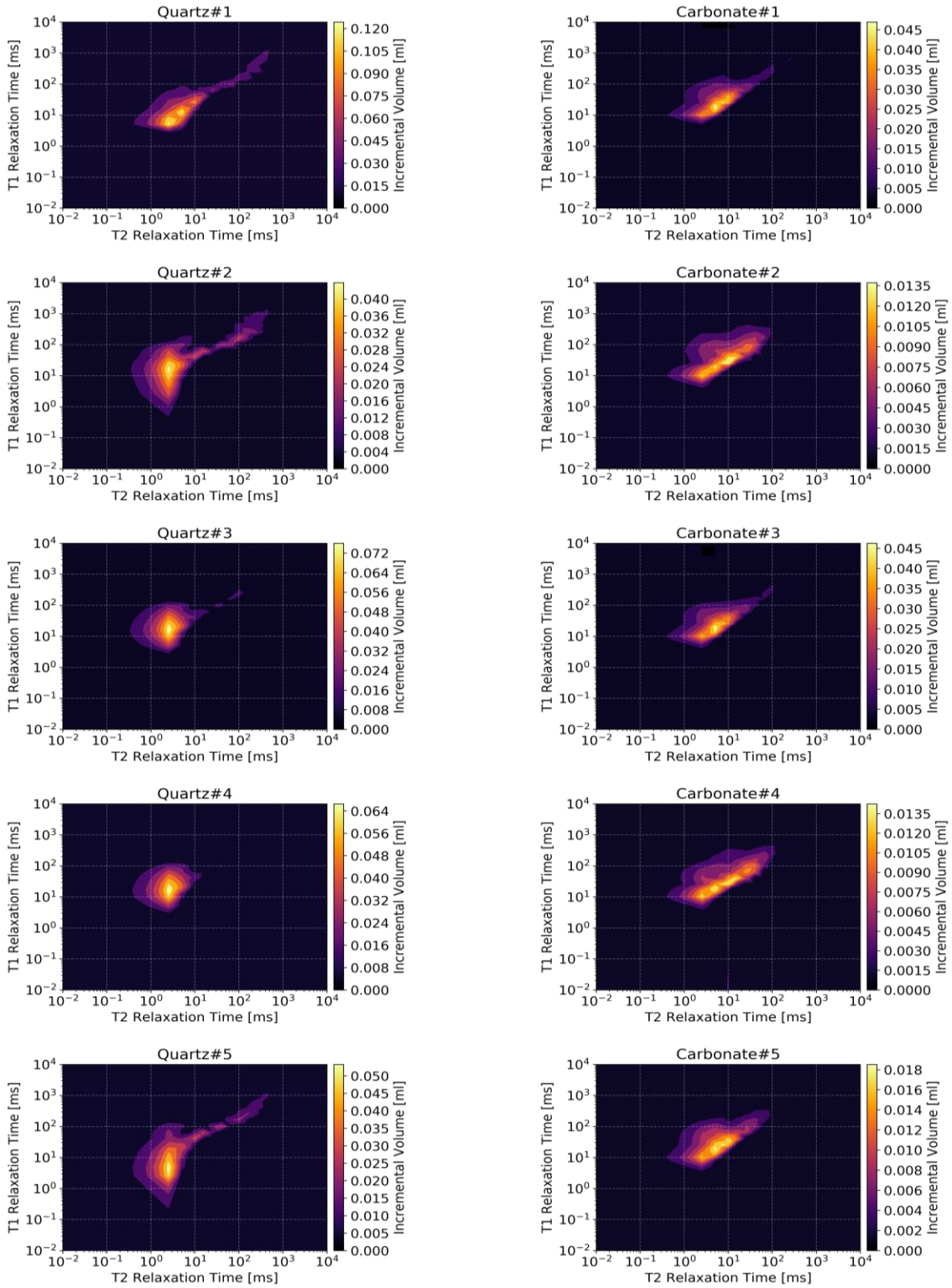

Figure 5-17 Bird's-eye views of spatial T2 distributions for 10 cores after four weeks of oil saturation: five quartz-rich (left) and five carbonate-rich (right).

5.3.2 Surfactant-Assisted Spontaneous Imbibition Fluid Analysis

There was a clear shift in the NMR response for almost all cores, indicating that another fluid besides oil was present in the porous media, as shown in **Figure 5-18**. The NMR response for the quartz-rich samples indicated a noticeable amount of produced oil and imbibed fluid. The PSD shift to lower T_2 values was caused by the difference in oil/fluid relaxivity. The densities for all of the surfactant solutions were close to that of distilled water, due to the low concentration used in the SASI experiment. Thus, the responses in terms of relaxivity and shift were identical to that of distilled water. Also, the total amount of fluid increased slightly, by an average of 0.35 ml and 0.05 ml for the quartz-rich and carbonate-rich core samples, respectively.

The increase in total fluid can be attributed to the fact that the displacement was not 1:1 with respect to intake and discharge volumes, due to the difference in compressibility between oil and water. Relatively speaking, 1.1 ml of water or surfactant solution was needed to displace around 0.9 ml of oil in both the quartz-rich and carbonate-rich Wolfcamp samples. The CBW appeared unchanged post-SASI, confirming that the quartz-rich samples tested had a significant amount of CBW, an average of 0.5 ml, which corresponded to 18% of the total fluid contained in the samples. Larger pore spaces (100 to 1,000 ms) did not contribute as much to the total produced oil, despite containing around 0.4 ml in the quartz-rich samples. The majority of the oil was produced from small pore spaces (1 to 100 ms), larger than those containing CBW. Such a phenomenon can be attributed to the higher capillarity forces exhibited by the smaller pores, as compared to the larger pores evidenced in the Young-Laplace equation.

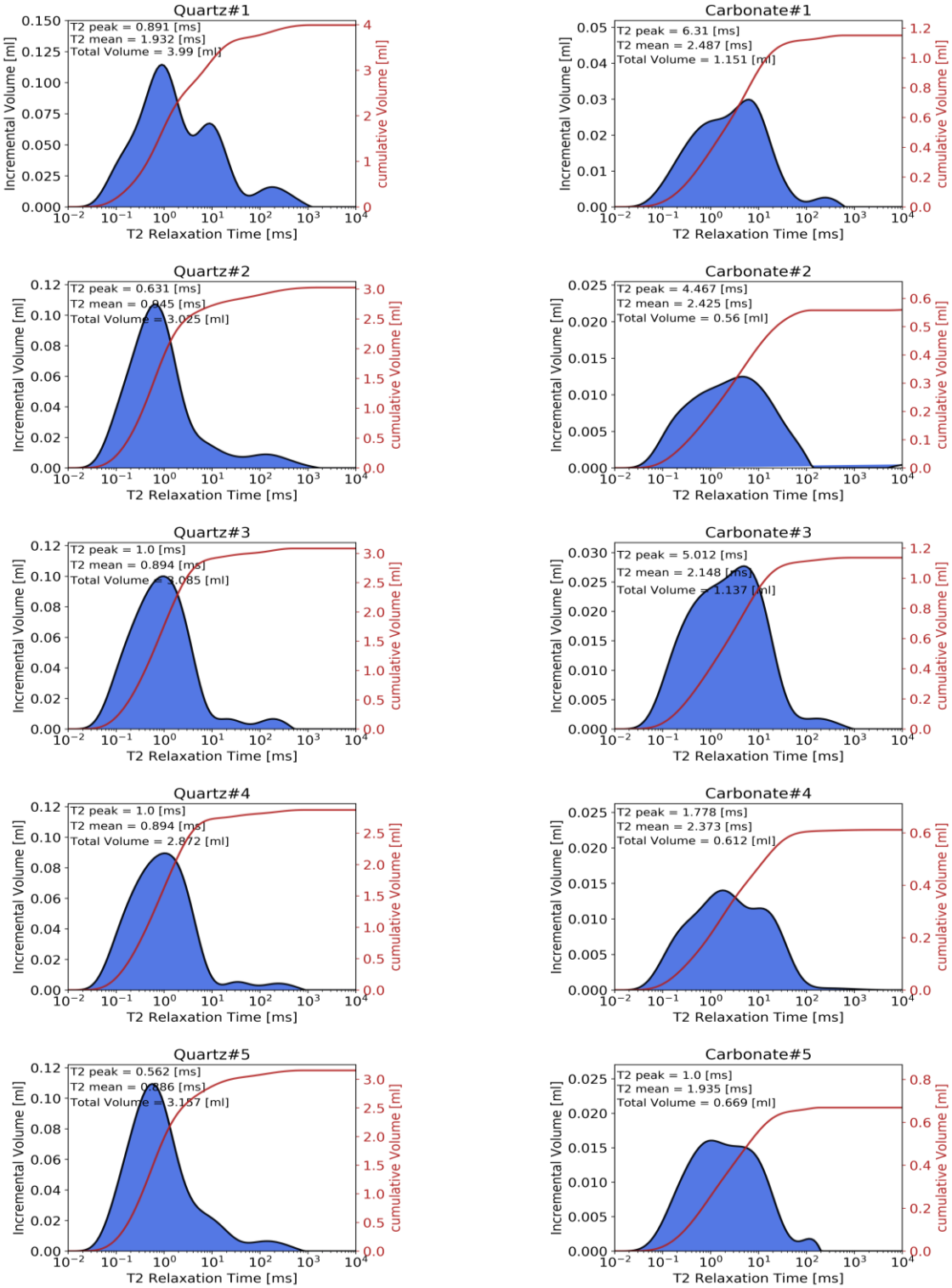

Figure 5-18 T2 distributions after SASI for 10 cores: five quartz-rich (left) and five carbonate-rich (right).

The contact angle of Nonionic 1 was found to be low in the Wolfcamp quartz-rich environment (i.e., **32º**), indicating extreme water wetness. The contact angle of Nonionic 2 was found to be low as well, in the same environment (i.e., **35º**). Both surfactant solutions had similar IFT values, and thus their recoveries by imbibition were expected to be similar. However, the oil produced from Quartz #1 was more than that of Quartz #3. As shown in **Figure 5-19**, the amounts of moveable oil contained in the smaller pores were about 3 ml and 1.7 ml for Quartz #1 and Quartz #3, respectively. The same concept was applied to Carbonate #1 and Carbonate #3, which had the same PSD yet resulted in different recoveries due to the predominant difference in wettability for both surfactants in the Wolfcamp carbonate-rich environment. Nonionic 1 had an intermediate wettability, while Nonionic 2 altered the wettability from oil wet to extremely water wet, which resulted in a higher oil recovery.

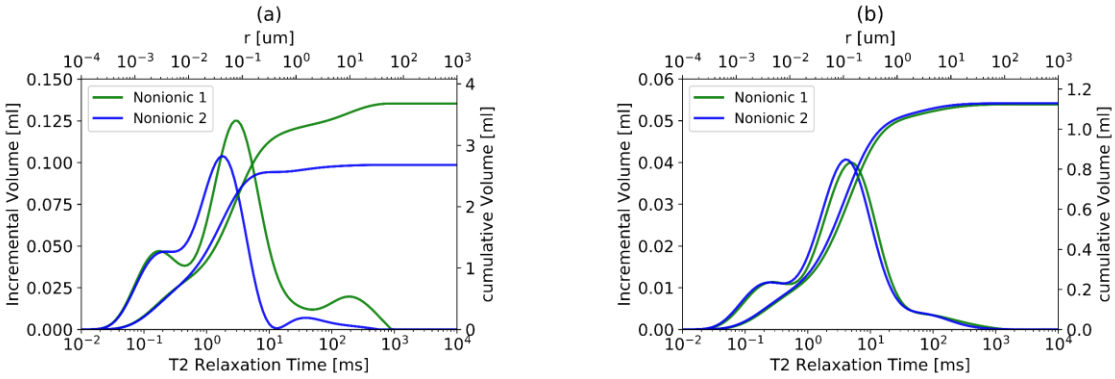

Figure 5-19 T2 distributions after saturation. The x-axis is the T2 values, while the y-axis is the cumulative volumes of fluid contained in the cores. The cumulative volumes of the cores are plotted in solid green for Nonionic 1 and dotted blue for Nonionic 2; (a) shows a clear PSD difference between Quartz #1 (Nonionic 1) and Quartz #3 (Nonionic 2), (b) shows the same PSD for Carbonate #1 (Nonionic 1) and Carbonate #3 (Nonionic 2).

Recovered oil volumes can be estimated using NMR deconvolution. This technique is employed to remove signal distortion caused by transforming the data using the BDR approach. Deconvolving the NMR spectrum breaks down the distribution into multiple peaks, focusing more on components that are interesting and discarding those that are considered less important. Three parameters (i.e., frequency, area, and line width) from the peaks of interest are needed to estimate the recovered oil volume. The deconvolution approach was undertaken using a combination of Gaussians, Lorentzian, and Voigt functions. There are multiple available open source software packages that can perform NMR deconvolution, such as Origin Pro Peak Fitting and IGOR. However, in this work, NumPy and SciPy were used to create unique peak fitting and solve the nonlinear sums of the functions. The peaks' routine was found using SciPy's "find_peaks_cwt" method. The Python package "lmfit" was then employed to automate all of the more tedious parts of the fitting process. It is worth noting that the deconvolution technique can result in non-unique solutions; thus, the same number of deconvoluted peaks was used in the analysis of each core sample in order to preserve consistency. Also, the total volumes before and after deconvolutions were preserved to eliminate any statistical inconsistencies resulting from the deconvolution.

Table 5-2 shows the imbibition distribution based on the equivalent spherical volume calculated using the obtained surface rock relaxivities and NMR deconvolution. The deconvoluted peaks for each sample before and after the SASI experiments are shown in **Figure 5-20** and **Figure 5-21**.

Table 5-2 Imbibition Contributions based on the Equivalent Spherical Radius Concept

Sample	Peak Center, ms	ESR, nm	After SI, ml	Before SI, ml	Net, ml	Imbibition %
Q1	0.35873	8.656	0.79825	0.41132	0.38693	36%
	9.9152	263.562	1.0627	0.37298	0.68972	64%
Q2	0.046848	1.9535616	0.54907	0.49066	0.05841	9%
	0.20603	8.591451	0.99087	0.53054	0.46033	71%
	7.1811	299.45187	0.25946	0.12827	0.13119	20%
Q3	0.29174	14.703696	0.85149	0.4997	0.35179	75%
	10.5221	530.3088	0.63766	0.48213	0.11553	25%
Q4	0.2819	13.86948	0.76097	0.44354	0.31743	69%
	1.2935	63.6402	0.65686	0.51553	0.14133	31%
Q5	0.049282	2.04471018	0.50708	0.50438	0.0027	0%
	0.24461	10.1488689	1.1704	0.49536	0.67504	71%
	6.3109	261.839241	0.40322	0.13408	0.26914	28%
C1	0.048097	1.1398989	0.056678	0.044545	0.012133	6%
	0.19019	4.507503	0.23511	0.17802	0.05709	28%
	10.9198	258.79926	0.25244	0.11911	0.13333	66%
C2	0.042731	0.8845317	0.038173	0.032909	0.005264	25%
	0.41875	8.668125	0.1187	0.10279	0.01591	75%
C3	0.17374	4.0081818	0.25281	0.13477	0.11804	41%
	10.8654	250.664778	0.27738	0.10802	0.16936	59%
C4	0.052596	1.16605332	0.034834	0.027575	0.007259	14%
	0.2819	6.249723	0.12541	0.11152	0.01389	27%
	1.6444	36.456348	0.15819	0.12696	0.03123	60%
C5	0.24461	5.5991229	0.16628	0.13146	0.03482	28%
	1.4177	32.451153	0.21794	0.12799	0.08995	72%

The majority of the imbibed fluid was contained in the mesopores. The cores with similar PSD values went through a similar imbibition process in the larger pores, regardless of the contact angle; this can be seen in both Carbonate #1 and Carbonate #3. However, the imbibed fluid distribution in the smaller pores was found to be different. Carbonate #3 exhibited more imbibition in pores < 5 nm in size (i.e., 41%), while the imbibition distribution for Carbonate #1 indicated that imbibition in the same pore range was less than 30%. This is clear evidence that more water-wetness did indeed cause more imbibition to occur in smaller pores, due to the increase in oil capillary pressure over that of water.

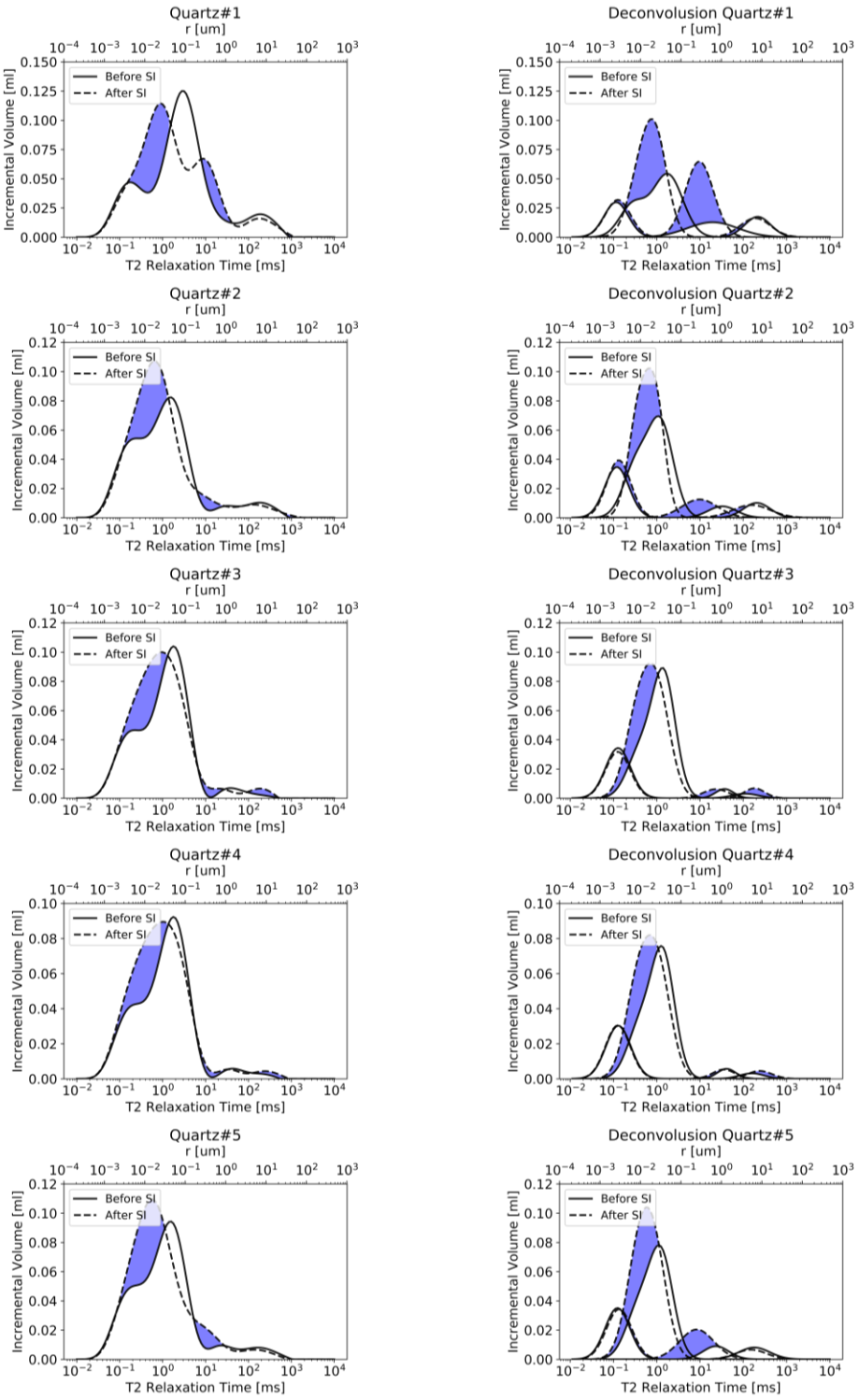

Figure 5-20 T_2 distributions before and after SASI for the quartz-rich samples; (left) is the difference before and after SASI, and (right) is the deconvoluted peaks for each sample. The water imbibed into the core is shaded in blue.

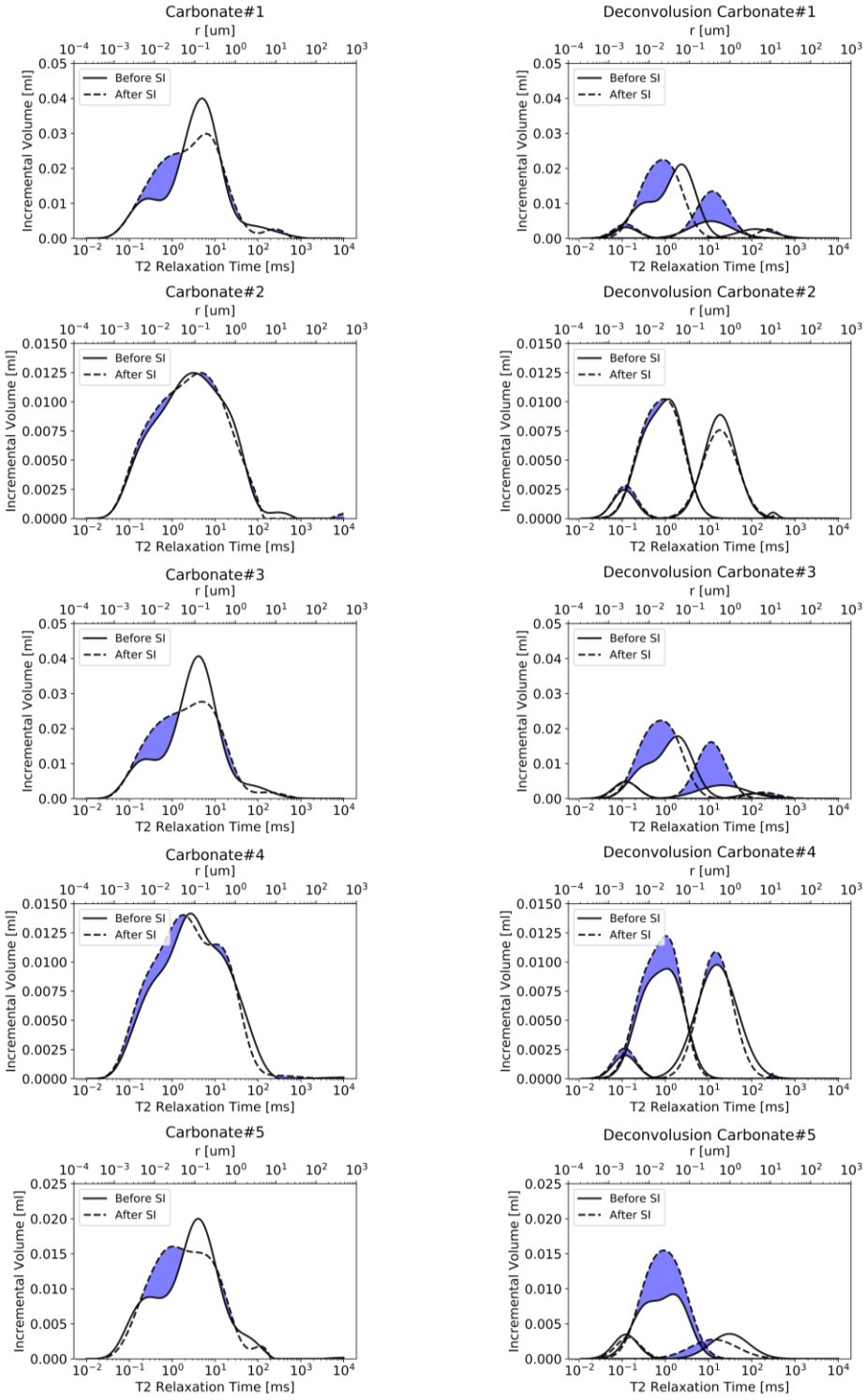

Figure 5-21 T_2 distributions before and after SASI for the carbonate-rich samples; (left) shows the difference before and after SASI, and (right) shows the deconvoluted peaks for each sample. The water imbibed into the core is shaded in blue.

In general, the majority of the imbibition process took place in small pores. In the quartz-rich samples, the range of equivalent spherical radii for imbibition was between 1 to 300 nm. However, more than 70% of the imbibed fluid in the clastic environment occurred in pores smaller than 15 nm, with the exception of Quartz #1, where the majority of the imbibition was located in pores between 2 nm and 300 nm in size. As explained above, Quartz #1 is a special case among the quartz-rich samples; the PSD was slightly different from the other cores, and the average pore size was slightly larger than those of the other core samples. Moreover, the frequency of occurrence of those pores was higher compared to all of the tested core samples, and this was suspected as the reason behind the different observed imbibition mechanisms. The post-SASI PSD plot shown in **Figure 5-18** indicates that the imbibition process in Quartz #1 was not finished by the time the cores were NMR scanned. This was where two fluids coexisted in the larger pores, which can be interpreted as incomplete imbibition. In the carbonate-rich samples, however, the range of equivalent spherical radii for imbibition was between 10 to 260 nm, depending on the sample.

Since the produced to imbibed fluid ratio is never 1:1, the volume of the imbibed water will almost always be larger than the volume of oil produced; hence, a correction factor was needed. This research proposes a correction ratio that is unique for each sample and can be obtained directly from the total volume before and after SASI. The oil recovered can then be calculated by **Eq. (5-8)**, as follows:

$$NMR\ V_o \simeq V_{iw} \times \left(\frac{V_{tb}}{V_{ta}}\right) \tag{5-8}$$

where V_{iw} is the imbibed volume in ml, and can be calculated by the area difference for each peak of interest; V_{tb} is the total NMR volume before the SASI experiment; and V_{ta} is the total NMR volume after the SASI experiment. A clear correlation is demonstrated in **Figure 5-22**, where the actual collected oil increased with the increase in approximated NMR oil. This can be referred to as a positive correlation. The only substantive difference between the two was found in Quartz #2. The approximated NMR for the produced oil was found to be 0.6 ml, while the collected was measured at 0.4 ml. This difference can be attributed to the fact that there was a visible amount of oil attached to the surface of the core sample. The oil was not collected because of the significant oil-wetness of the surface; hence, water was used in Quartz #2. The volume of the attached oil was counted as part of the NMR volume, as it was not contained in the porous medium. It was also not part of the measured oil in the modified Amott cell, since it was not collected.

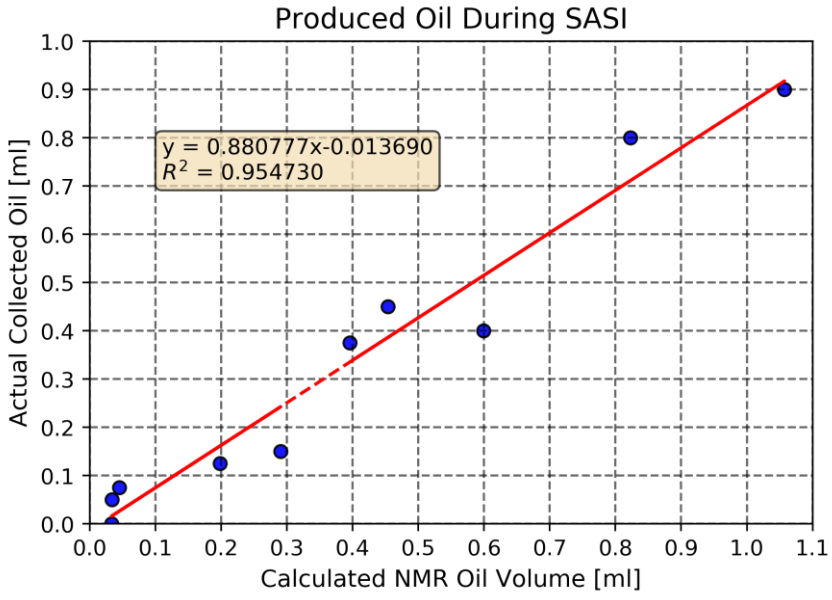

Figure 5-22 Collected oil produced using modified Amott cells vs. oil approximately produced by NMR, using Eq. (5-8).

T_1/T_2 shows a clear contrast between the imbibed fluid and remaining oil. As previously mentioned, the T_1/T_2 oil ratio was around 2, which can clearly be seen in **Figure 5-23**.

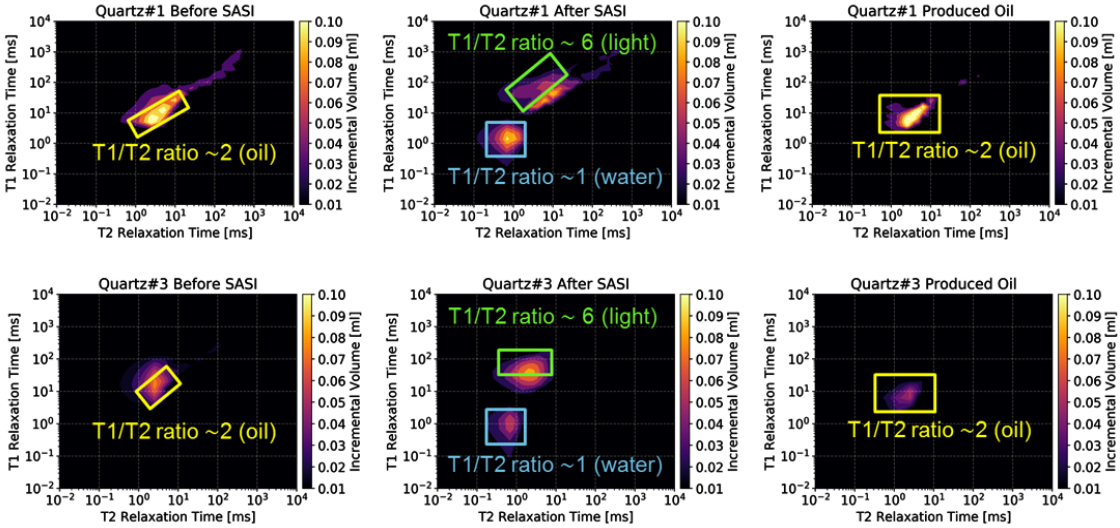

Figure 5-23 2D T_1-T_2 maps for Quartz #1 and Quartz #3. The maps in first column from the left represent fully oil saturated cores. The maps in the middle represent cores post-SASI. Lastly, the maps in the last column from the left represent the oil produced after SASI.

Imbibed fluid was also identified based on the after-SASI maps by the introduction of another peak with a T_1/T_2 ratio of around 1. The remaining fluid appeared to contain a small percentage of the heavier oil components and a fair percentage of the lighter hydrocarbon components, distinguished by a T_1/T_2 ratio of around 6 to 10. The distinction between the oils (i.e., original and produced) T_1/T_2 ratios indicated that the remaining oil was lighter compared to the produced fluid. A similar phenomenon was observed in the EF after CO_2 huff-and-puff followed by SASI, where the CO_2 huff-and-puff produced lighter fluids, as opposed to SASI which recovered slightly heavier fluids. This observation led to the conclusion that SASI recovered oil with heavier components (i.e., composition change). The 2D maps for the rest of the samples are shown in **Figure 5-24** and **Figure 5-25.**

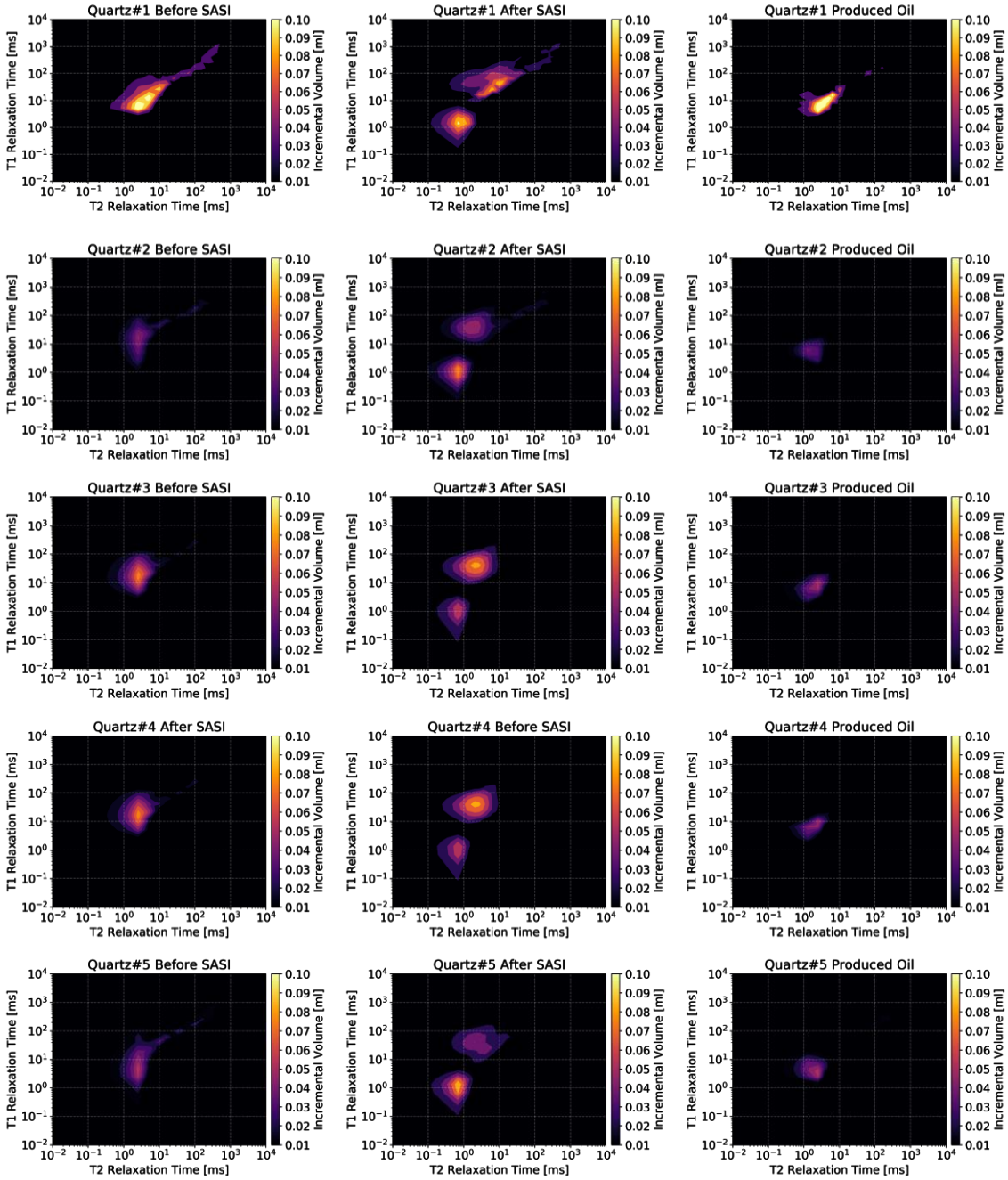

Figure 5-24 2D T_1-T_2 maps of quartz-rich samples. The maps in the first column from the left represent fully oil saturated cores. The maps in the middle represent cores post-SASI. Lastly, the maps in the last column from the left represent the oil produced after SASI.

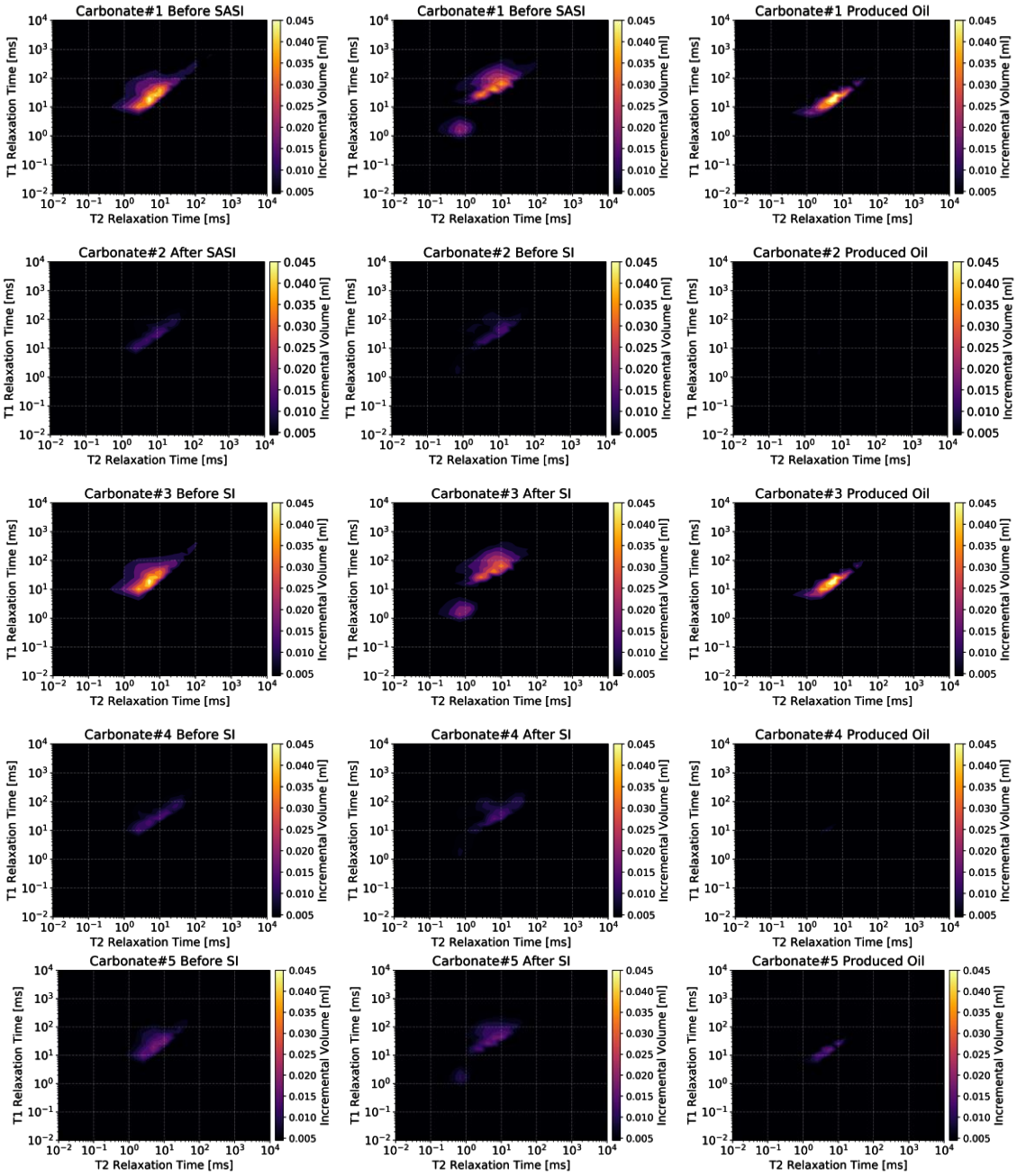

Figure 5-25 T_1-T_2 maps of carbonate-rich samples. The maps in the first column from the left represent fully oil saturated cores. The maps in the middle represent cores post-SASI. Lastly, the maps in the last column from the left represent oil produced after SASI.

CHAPTER 6

CONCLUSIONS

This work was conducted in order to come up with a robust and complete workflow for surfactant-assisted spontaneous imbibition assessment and evaluate the mechanism of the imbibition process with respect to the the petrophysical attributes of the samples. This chapter is divided into three main subsections based on the outcomes of this work: (1) fundamental analysis and experimental methods, (2) surfactant-assisted spontaneous imbibition and oil displacement and (3) textural characteristics and the imbibition mechanism influence.

6.1 Fundamental Analysis and Experimental Methods

The addition of surfactants caused an IFT reduction. Yet, the desired magnitude of IFT reduction should be less than those experienced in high permeability reservoirs flooding applications. The addition of surfactants alters the wettability state of the rock surface. The contact angle measurement performed in this work indicated that a clear shift in the wettability from oil-wet to water-wet, which was predominant in the clastic rocks more than that of the carbonate. Also, surfactant systems helped making the aqueous phase more stable by forming a double layer around the rock particle. In this case, ζ potential provided valued insights into rock particles interactions and enhanced the understanding of stability. However, most of the information obtained from an electrophoresis experiment was far from being quantitative. Challenges arised from the fact that heterogeneous mixtures of solid particles are suspended in a complex aqueous medium with various molecules and hydrocarbon particles. Nevertheless, even with being

qualitative at best, the sign of the charge, be it positive or negative, indicated the surfactant potential and charge because of the different interactions between the particles and the medium. Each chemical exhibits a different diffusion potential trend depending on the concentration, pH, dispersed particles, sample count rate and aging time. The ζ potential was found to be relatively stable after 4 to 8 hours in the case of the evaluated surfactant solutions. Also, the ζ potential measurements of the of rock-surfactant interfaces were found to be similar for both carbonate-rich and quartz-rich rocks with the Cationic surfactant displaying the highest standard deviation from the mean as opposed to the Nonionic surfactants. Adding a solvent to one of the nonionic surfactants caused the ζ potential to fluctuate triggering the formation of an unstable double layer that changes constantly with time. When oil was integrated into the system, even qualitative information became hard to interpret. Despite that the layer inside the oil droplets of the solution is often stable in the oil-rock interface, the surface of the oil drop was deemed complex to study due to being covered with a complex chemical with different compositions that were unknown during the course of this work.

6.2 Surfactant-Assisted Spontaneous Imbibition And Oil Displacement

Surfactant addition enhanced oil production from capillary-driven spontaneous imbibition, which can be translated to higher cumulative oil production and rate. Wettability alteration played a dominant role in the oil production from SASI as surfactant that altered wettability the most also produced the most oil, relatively. In this work, Nonionic 1 and Nonionic 2 resulted in a similar oil recoveries at 27.3% and 21.3% with 9.2% and 3.2% additional oil recovery compared to the water base case, respectively. The

Cationic surfactant performed similarly to the base case in the quartz-rich samples where the measured recovery factor was 19.2% with 1.1% additional oil recovery compared to the water base case. Nonionic 3 yielded the highest oil recovery in the quartz-rich samples at 35.9% with 17.8%, 16.7%, 14.6% and 8.6% additional oil recovery compared to water, cationic, nonionic 2 and nonionic 1, respectively. Oil recovery from carbonate-rich core samples ranged from 14.8% to 49%**.** All Nonionic surfactants performed similarly with 14.8%, 15.2% and 17.2% for Nonionic 1, Nonionic 3 and Nonionic 2, respectively. The Cationic surfactant outperformed all the tested surfactant solution systems in the carbonate-rich environment where the measured recovery factor was around 49%. When comparing the imbibition result of the surfactants in the carbonate-rich environment, the best recovery improvement was achieved from the Cationic Surfactant.

The general trend observed on all tested core samples from the XY CT images was that a clear imbibition of the aqueous-phase into the rock sample along with expulsion of oil in the same process, which can be termed as “replacement”. In the quartz-rich samples, it was observed on most samples that the imbibition occurred in the beginning slices or last slices with minimal changes in the slices taken from the middle of the plugs. Also, in this case, the majority of the imbibition occurred in smaller pores as the frequency of occurrence of larger pores was scarce. As for the carbonate samples, images showed that the core samples were tighter in general with greater average CT numbers compared to those of the quartz-rich samples. The observed fluid movement was similar to that of the clastic samples; yet, less noticeable due to the limited amount of saturated oil in the cores.

6.3 Texturare Characteristics and the Imbibition Mechanism Influence

NMR results revealed that the PSD plays a significant role in SASI EOR where the majority of the imbibed fluid was observed in smaller pores (Mesopores), larger than those of Clay Bound Water (CBW) and smaller than those of high permeability streaks or bedding planes. The cores with similar PSD exhibited a comparable imbibition process in larger pores regardless of the wettability. However, the imbibed fluid distribution in smaller pores was found to be a bit different and slightly influenced by wettability. For instance, Carbonate#3 exhibited more imbibition in pores <5 nm at 41% while the imbibition distribution for Carbonate#1 indicated that the imbibition in the same pore range was less than 30%. This was deemed as a clear evidence that more water-wetness does cause more imbibition to occur in smaller pores due to the increase of the oil capillary pressure compared to that of water.

T_1/T_2 2-D maps showed a contrast between the imbibed fluid and the remaining oil. Imbibed fluid was identified after SASI through the introduction of another proton distribution peak with a T_1/T_2 ratio of around 1. The remaining fluid appeared to be mixed between oil and lighter fluid that is slightly lighter with a T_1/T_2 ratio of around T_1/T_2~6-10. The produced oil, however, had a T_1/T_2 ratio of around 2 indicating that the remaining fluid was lighter compared to the produced fluid which was observed post-SASI. The same phenomenon was observed more clearly in the Eagle Ford after CO_2 huff & puff followed by SASI where the CO_2 huff & puff produced lighter fluids as opposed to SASI that recovered slightly heavier fluids. It is believed that such phenomenon occurred because

the oil samples collected from SASI were “weathered”, (i.e., they lacked low-end hydrocarbon fractions, which caused the observed darker colors).

REFERENCES

Advani, S.H., H Khattab, and J.K. Lee. 1985. “Hydraulic Fracture Geometry Modeling, Prediction, and Comparisons.” In *SPE/DOE Low Permeability Gas Reservoirs Symposium*, 10. Denver, Colorado: Society of Petroleum Engineers. https://doi.org/10.2118/13863-MS.

Alvarez, J. O., and David S. Schechter. 2016. “Wettability, Oil and Rock Characterization of the Most Important Unconventional Liquid Reservoirs in the United States and the Impact on Oil Recovery.” *Proceedings of the 4th Unconventional Resources Technology Conference*, 2997–3017. https://doi.org/10.15530/urtec-2016-2461651.

Alvarez, J. O., F. D. Tovar, and D. S. Schechter. 2017. “Improving Oil Recovery in Unconventional Liquid Reservoirs by Soaking-Flowback Production Schedule with Surfactant Additives.” *SPE Liquids-Rich Basins Conference - North America*. https://doi.org/10.2118/187483-MS.

Alvarez, J O, I W R Saputra, and D S Schechter. 2017. “The Impact of Surfactant Imbibition and Adsorption for Improving Oil Recovery in the Wolfcamp and Eagle Ford Reservoirs.” *SPE Annual Technical Conference and Exhibition*. San Antonio, Texas, USA: Society of Petroleum Engineers. https://doi.org/10.2118/187176-MS.

Alvarez, J O, and D S Schechter. 2015. “Wettability Alteration and Spontaneous Imbibition in Unconventional Liquid Reservoirs by Surfactant Additives.” *SPE Latin American and Caribbean Petroleum Engineering Conference*. Quito, Ecuador: Society of Petroleum Engineers. https://doi.org/10.2118/177057-MS.

———. 2016. “Altering Wettability in Bakken Shale by Surfactant Additives and Potential of Improving Oil Recovery During Injection of Completion Fluids.” *SPE Improved Oil Recovery Conference*. Tulsa, Oklahoma, USA: Society of Petroleum Engineers. https://doi.org/10.2118/179688-MS.

Alvarez, Johannes O, Anirban Neog, Afif Jais, and David S Schechter. 2014. “Impact of Surfactants for Wettability Alteration in Stimulation Fluids and the Potential for Surfactant EOR in Unconventional Liquid Reservoirs.” In *SPE Unconventional Resources Conference*, 468–85. Society of Petroleum Engineers. https://doi.org/10.2118/169001-MS.

Alvarez, Johannes O, I Wayan Rakananda Saputra, and David S Schechter. 2017. “Potential of Improving Oil Recovery with Surfactant Additives to Completion Fluids for the Bakken.” *Energy & Fuels* 31 (6): 5982–94. https://doi.org/10.1021/acs.energyfuels.7b00573.

Arthur F Taggart. 1951. *Elements of Ore Dressing*. Wiley (1951).

Austad, T, B Matre, J Milter, A Sævareid, and L Øyno. 1998. “Chemical Flooding of Oil Reservoirs 8. Spontaneous Oil Expulsion from Oil- and Water-Wet Low Permeable Chalk Material by Imbibition of Aqueous Surfactant Solutions.” *Colloids and Surfaces A: Physicochemical and Engineering Aspects* 137 (1): 117–29. https://doi.org/https://doi.org/10.1016/S0927-7757(97)00378-6.

Babadagli, T, A Al-Bemani, and F Boukadi. 1999. “Analysis of Capillary Imbibition Recovery Considering the Simultaneous Effects of Gravity, Low IFT, and Boundary Conditions.” In *SPE Asia Pacific Improved Oil Recovery Conference*, 9. Kuala Lumpur, Malaysia: Society of Petroleum Engineers. https://doi.org/10.2118/57321-MS.

Baxter, S, and A B D Cassie. 1945. “8—THE WATER REPELLENCY OF FABRICS AND A NEW WATER REPELLENCY TEST.” *Journal of the Textile Institute Transactions* 36 (4): T67–90. https://doi.org/10.1080/19447024508659707.

Benavides, Francisco, Ricardo Leiderman, Andre Souza, Giovanna Carneiro, and Rodrigo Bagueira. 2017. “Estimating the Surface Relaxivity as a Function of Pore Size from NMR T2 Distributions and Micro-Tomographic Images.” *Computers & Geosciences* 106 (June): 200–208. https://doi.org/10.1016/j.cageo.2017.06.016.

Bloembergen, N, E M Purcell, and R V Pound. 1947. “Nuclear Magnetic Relaxation.” *Nature* 160 (October): 475.

Brownstein, K. R., and C. E. Tarr. 1979. “Importance of Classical Diffusion in NMR Studies of Water in Biological Cells.” *Physical Review A* 19 (6): 2446–53. https://doi.org/10.1103/PhysRevA.19.2446.

Butler, J P, J A Reeds, and S V Dawson. 1981. “Estimating Solutions of First Kind Integral Equations with Nonnegative Constraints and Optimal Smoothing.” *SIAM Journal on Numerical Analysis* 18 (3): 381–97. http://www.jstor.org/stable/2156861.

Coates, George R, M Miller, M Gillen, and C Henderson. 1991. “The MRIL In Conoco 33-1 An Investigation Of A New Magnetic Resonance Imaging Log.” *SPWLA 32nd Annual Logging Symposium*. Midland, Texas: Society of Petrophysicists and Well-Log Analysts. https://doi.org/.

Cuiec, L E, B Bourbiaux, and F Kalaydjian. 1994. “Oil Recovery by Imbibition in Low-Permeability Chalk.” *SPE Formation Evaluation* 9 (03): 200–208. https://doi.org/10.2118/20259-PA.

Garg, A., A.R. Kovscek, M Nikravesh, L.M. Castanier, and T.W. Patzek. 1996. “CT Scan and Neural Network Technology for Construction of Detailed Distribution of Residual Oil Saturation During Waterflooding.” In *SPE Western Regional Meeting*. Society of Petroleum Engineers. https://doi.org/10.2118/35737-MS.

Hirasaki, G J. 1991. “Wettability: Fundamentals and Surface Forces.” *SPE Formation Evaluation* 6 (02): 217–26. https://doi.org/10.2118/17367-PA.

Hove, A.O., J.K. Ringen, and P.A. Read. 1987. “Visualization of Laboratory Corefloods With the Aid of Computerized Tomography of X-Rays.” *SPE Reservoir Engineering* 2 (02): 148–54. https://doi.org/10.2118/13654-PA.

Hunter, Robert J, ed. 1981. “COLLOID SCIENCE.” In *Zeta Potential in Colloid Science*, ii. Academic Press. https://doi.org/https://doi.org/10.1016/B978-0-12-361961-7.50001-8.

J. Hill, H, O J. Shirley, and G E. Klein. 1979. *Bound Water in Shaly Sands: Its Relation to Q/Sub v/ and Other Formation Properties*. Vol. 20.

Kesserwan, Hasan, Guodong Jin, Gaurav Agrawal, and Abdullah Sultan. 2016. "Wettability Characterization and Comparison of Carbonate Source Rocks Using NMR." *SPWLA 57th Annual Logging Symposium*. Reykjavik, Iceland: Society of Petrophysicists and Well-Log Analysts. https://doi.org/.

Kwok, D Y, R Lin, M Mui, and A W Neumann. 1996. "Low-Rate Dynamic and Static Contact Angles and the Determination of Solid Surface Tensions." *Colloids and Surfaces A: Physicochemical and Engineering Aspects* 116 (1): 63–77. https://doi.org/https://doi.org/10.1016/0927-7757(96)03590-X.

Liang, Tianbo, Rafael A Longoria, Jun Lu, Quoc P Nguyen, and David A DiCarlo. 2017. "Enhancing Hydrocarbon Permeability After Hydraulic Fracturing: Laboratory Evaluations of Shut-Ins and Surfactant Additives." *SPE Journal* 22 (04): 1011–23. https://doi.org/10.2118/175101-PA.

Linda Doman, Ari Kahan. 2018. "United States Remains the World's Top Producer of Petroleum and Natural Gas Hydrocarbons - Today in Energy - U.S. Energy Information Administration (EIA)." U.S Energy Information Administration. 2018. https://www.eia.gov/todayinenergy/detail.php?id=36292.

Lindsay, G, G Miller, T Xu, D Shan, and J Baihly. 2018. "Production Performance of Infill Horizontal Wells vs. Pre-Existing Wells in the Major US Unconventional Basins." In *SPE Hydraulic Fracturing Technology Conference and Exhibition*, 28. The Woodlands, Texas, USA: Society of Petroleum Engineers. https://doi.org/10.2118/189875-MS.

Losso, Jack N, Armen Khachatryan, Masahiro Ogawa, J Sam Godber, and Fred Shih. 2005. “Random Centroid Optimization of Phosphatidylglycerol Stabilized Lutein-Enriched Oil-in-Water Emulsions at Acidic PH.” *Food Chemistry* 92 (4): 737–44. https://doi.org/https://doi.org/10.1016/j.foodchem.2004.12.029.

Lu, Yingda, Nariman Fathi Najafabadi, and Abbas Firoozabadi. 2017. “Effect of Temperature on Wettability of Oil/Brine/Rock Systems.” *Energy & Fuels* 31 (5): 4989–95. https://doi.org/10.1021/acs.energyfuels.7b00370.

Lyu, Chaohui, Qing Wang, Zhengfu Ning, Mingqiang Chen, Mingqi Li, Zhili Chen, and Yuxuan Xia. 2018. “Investigation on the Application of NMR to Spontaneous Imbibition Recovery of Tight Sandstones: An Experimental Study.” *Energies* 11 (9): 2359. https://doi.org/10.3390/en11092359.

Marinova, K. G., R. G. Alargova, N. D. Denkov, O. D. Velev, D. N. Petsev, I. B. Ivanov, and R. P. Borwankar. 1996. “Charging of Oil−Water Interfaces Due to Spontaneous Adsorption of Hydroxyl Ions.” *Langmuir* 12 (8): 2045–51. https://doi.org/10.1021/la950928i.

McNeil-Watson, Fraser, Walther Tscharnuter, and John Miller. 1998. “A New Instrument for the Measurement of Very Small Electrophoretic Mobilities Using Phase Analysis Light Scattering (PALS).” *Colloids and Surfaces A: Physicochemical and Engineering Aspects* 140 (1): 53–57. https://doi.org/https://doi.org/10.1016/S0927-7757(97)00267-7.

Menouar, Habib, and Roy M Knapp. 1980. “Numerical Simulation Of The Imbibition Process In Fractured Reservoirs.” *SPE Annual Technical Conference and Exhibition*. Dallas, Texas: Society of Petroleum Engineers. https://doi.org/10.2118/9370-MS.

Morrow, Norman R., and Geoffrey Mason. 2001. “Recovery of Oil by Spontaneous Imbibition.” *Current Opinion in Colloid & Interface Science* 6 (4): 321–37. https://doi.org/10.1016/S1359-0294(01)00100-5.

Nelson, Philip H. 2009. “Pore-Throat Sizes in Sandstones, Tight Sandstones, and Shales.” *AAPG Bulletin* 93 (3): 329–40. https://doi.org/10.1306/10240808059.

Park, Kang Han, and David S Schechter. 2018. “Investigation of the Interaction of Surfactant at Variable Salinity with Permian Basin Rock Samples: Completion Enhancement and Application for Enhanced Oil Recovery.” *SPE Liquids-Rich Basins Conference - North America*. Midland, Texas, USA: Society of Petroleum Engineers. https://doi.org/10.2118/191801-MS.

Parsons, R.W., and P.R. Chaney. 1966. “Imbibition Model Studies on Water-Wet Carbonate Rocks.” *Society of Petroleum Engineers Journal* 6 (01): 26–34. https://doi.org/10.2118/1091-PA.

Petrov, Oleg V., and Bruce J. Balcom. 2011. “Two-Dimensional T2 Distribution Mapping in Porous Solids with Phase Encode MRI.” *Journal of Magnetic Resonance* 212 (1): 102–8. https://doi.org/10.1016/j.jmr.2011.06.018.

Rassenfoss, Stephen. 2017. “Shale EOR Works, But Will It Make a Difference?” *Journal of Petroleum Technology* 69 (10): 34–40. https://doi.org/10.2118/1017-0034-JPT.

Ren, Xiaoxia, Aifen Li, Asadullah Memon, Shuaishi Fu, Guijuan Wang, and Bingqing He. 2019. “Experimental Simulation on Imbibition of the Residual Fracturing Fluid in Tight Sandstone Reservoirs.” *Journal of Energy Resources Technology* 141 (8): 82906–9. http://dx.doi.org/10.1115/1.4042734.

Riddick, T M. 1968. *Control of Colloid Stability Through Zeta Potential: With a Closing Chapter on Its Relationship to Cardiovascular Disease*. Publié pour Zeta-Meter, Incorporated, by Livingston Publishing Company. https://books.google.com/books?id=4ZRDnwEACAAJ.

Rosen, Milton J. 2004. *Surfactants and Interfacial Phenomena*. *Colloids and Surfaces*. Vol. 40. Hoboken, NJ, USA: John Wiley & Sons, Inc. https://doi.org/10.1002/0471670561.

Saidian, Milad, and Manika Prasad. 2015. “Effect of Mineralogy on Nuclear Magnetic Resonance Surface Relaxivity: A Case Study of Middle Bakken and Three Forks Formations.” *Fuel* 161: 197–206. https://doi.org/10.1016/j.fuel.2015.08.014.

Salehi, Mehdi, Stephen J Johnson, and Jenn-Tai Liang. 2008. “Mechanistic Study of Wettability Alteration Using Surfactants with Applications in Naturally Fractured Reservoirs.” *Langmuir* 24 (24): 14099–107. https://doi.org/10.1021/la802464u.

Saputra, I Wayan Rakananda, and David S Schechter. 2018. “Comprehensive Workflow for Lab to Field-Scale Numerical Simulation to Improve Oil Recovery in the Eagle Ford Shale by Selective Testing and Modeling of Surfactants for Wettability Alteration.” In *Proceedings of the 6th Unconventional Resources Technology Conference*, 22. Tulsa, OK, USA: American Association of Petroleum Geologists. https://doi.org/10.15530/urtec-2018-2884598.

Schafersman, Steven D. 1997. “An Introduction to Science, Scientific Thinking and the Scientific Method.” http://www.geo.sunysb.edu/esp/files/scientific-method.html.

Schechter, D.S, D Zhou, and F.M Orr. 1994. “Low IFT Drainage and Imbibition.” *Journal of Petroleum Science and Engineering* 11 (4): 283–300. https://doi.org/10.1016/0920-4105(94)90047-7.

Sidle, Rodney, and W Lee. 2010. “The Demonstration of a ‘Reliable Technology’ for Estimating Oil and Gas Reserves.” https://doi.org/10.2523/129689-ms.

Sing, K. S. W. 1982. “Reporting Physisorption Data for Gas/Solid Systems with Special Reference to the Determination of Surface Area and Porosity (Provisional).” *Pure and Applied Chemistry* 54 (11): 2201–18. https://doi.org/10.1351/pac198254112201.

Standnes, Dag, and Tor Austad. 2003. *Wettability Alteration in Carbonates*. *Colloids and Surfaces A: Physicochemical and Engineering Aspects*. Vol. 216. https://doi.org/10.1016/S0927-7757(02)00580-0.

Steward, Dan B. 2013. “George P. Mitchell and the Barnett Shale.” *Journal of Petroleum Technology* 65 (11): 58–68. https://doi.org/10.2118/1113-0058-JPT.

Stuckner, Joshua, Katherine Frei, Ian McCue, Michael J. Demkowicz, and Mitsuhiro Murayama. 2017. “AQUAMI: An Open Source Python Package and GUI for the Automatic Quantitative Analysis of Morphologically Complex Multiphase Materials.” *Computational Materials Science* 139 (November): 320–29. https://doi.org/10.1016/j.commatsci.2017.08.012.

Sulucarnain, Ismail Dean, Carl H. Sondergeld, and Chandra Shekhar Rai. 2012. “An NMR Study of Shale Wettability and Effective Surface Relaxivity.” In *SPE Canadian Unconventional Resources Conference*. Vol. 1. Society of Petroleum Engineers. https://doi.org/10.2118/162236-MS.

Utpalendu Kuila. 2013. *Measurement and Interpretation of Porosity and Pore-Size Distribution in Mudrocks: The Hole Story of Shales*. https://books.google.com/books?id=Laj2ngEACAAJ.

Wenzel, Robert N. 1936. “RESISTANCE OF SOLID SURFACES TO WETTING BY WATER.” *Industrial & Engineering Chemistry* 28 (8): 988–94. https://doi.org/10.1021/ie50320a024.

Wolfs, F.L.H. 1996. “Introduction to the Scientific Method.” University of Rochester, Rochester, New York, USA. 1996. http://teacher.pas.rochester.edu/PHY_LABS/AppendixE/AppendixE.html.

Xie, Xina, William W Weiss, Zhengxin J Tong, and Norman R Morrow. 2005. "Improved Oil Recovery from Carbonate Reservoirs by Chemical Stimulation." *SPE Journal* 10 (03): 276–85. https://doi.org/10.2118/89424-PA.

Yuan, Yuehua, and T Randall Lee. 2013. *Surface Science Techniques*. Edited by Gianangelo Bracco and Bodil Holst. Vol. 51. Springer Series in Surface Sciences. Berlin, Heidelberg: Springer Berlin Heidelberg. https://doi.org/10.1007/978-3-642-34243-1.

Zhang, Jieyuan, Quoc P Nguyen, Adam Flaaten, and Gary A Pope. 2009. "Mechanisms of Enhanced Natural Imbibition With Novel Chemicals." *SPE Reservoir Evaluation & Engineering* 12 (06): 912–20. https://doi.org/10.2118/113453-PA.

Zhang, W, M Wahlgren, and B Sivik. 1989. "Membrane Characterization by the Contact Angle Technique." *Desalination* 72 (3): 263–73. https://doi.org/10.1016/0011-9164(89)80011-6.